EVALUATION OF THE CONTINUOUS DETECTOR CONCEPT FOR PET SYSTEMS DEDICATED TO SMALL ANIMALS BY USING THE MONTE CARLO SIMULATION METHOD

by

Sakine Şebnem ERTÜRK

B.S. in Physics Engineering

Gaziantep University, 2002

Submitted to Institute of Biomedical Engineering

in partial fullfillment of the requirements

for the degree of

Master of Science

in

Biomedical Engineering

Boğaziçi University

January 2007

ACKNOWLEDGMENT

First and foremost, I would like to thank my supervisor, Assoc.Prof.Dr. Albert GÜVENİŞ, for his hard work,valuable guidance, information, endless patience and support.

Special thanks to my committee members for giving me their valuable time as well as their helpful suggestions.

Also, I would like to thank all the members of Bogazici University Institute of Biomedical Engineering.

Many thanks to Jinhun Joung, Ph.D. Patent Manager Siemens Medical Solutions USA, Inc. Molecular Imaging , Mehmet Aykac, Ph.D.Senior Scientist Siemens Molecular Imaging Detector R&D, Christopher J. Thompson DSc. FCCPM Montreal Neurological Institute/ McGill University , Tom Ruth , Director, UBC/TRIUMF PET Program, Prof. Valeri Saveliev, Obninsk State University, Obninsk, Russia , Alberto Del Guerra Professor of Medical Physics University of Pisa Department of Physics,E.Fermi, Tom K. Lewellen, Professor of Radiology, Division of Nuclear Medicine Department of Radiology, University of Washington , Gunes Yavuz Regional Account Manager NM & Oncology Business Line Manager Philips Medical Systems Turkey ,İkbal Çam, Kenan GÜRSOY and Gürcan Atakök for their valuable information, guidance and support.

I would like to thank my family and friends for believing in me and support.

Finally, very special thanks to Dr. Orhan TERNAR. I feel immense gratitude towards him for his hard work, great patience during my study. Without his valuable suggestions, knowledge and ideas, this work would not have been possible.

ABSTRACT
EVALUATION OF THE CONTINUOUS DETECTOR CONCEPT FOR PET SYSTEMS DEDICATED TO SMALL ANIMALS BY USING THE MONTE CARLO SIMULATION METHOD

A detector design especially for small animal PET systems requires taking into account three main factors: these are high energy and spatial resolution and price. When examining the state-of-the-art PET detectors, it can be seen that many researchers have preferred to use continuous (monolithic), block or discrete crystals for small animal PET systems. Although, the discrete crystal detector designs have provided high spatial resolution, they also have caused many complications such as, reduced light collection (low packing fraction), labour-intensive use and increased costs. In this study, to overcome these limitations, the feasibility of using a continuous crystal instead of block or discrete designs has been explored for high resolution small animal PET applications. For this aim, a PET detector for small animals based on continuous block Lutetium oxyorthosilicate crystal (LSO) (16mm x 16mm) coupled to a PS-PMT (Hamamatsu H8711-03) has been designed. When working with continuous crystals, surface treatment and crystal thickness are important factors that strongly determine the main characteristics of the detector module. Therefore, for the development of this explored small animal PET detector, the effects of these factors on the detector module performances have been investigated, in order to optimize crystal configuration. In this study 4 different surface treatments (Polish + Black, Ground + Black, Ground + Methacrylate, Ground + Air), 3 different crystal thickness (3mm-6mm-9mm) and 41 different source coordinates were used. The obtained results for the energy resolution, spatial resolution and image compression have been presented when using different surface treatments and thicknesses in continuous LSO crystals. The simulation results have been carried out by using DETECT2000 package.

The end word, high spatial resolution is the most important parameter for a PET detector. In our study, Ground + Air (GA) surface treatment gives the highest special resolution but, the image compression is poor. However, this poorness can be avoided by using certain statistics based positioning (SBP) algorithms.

Keywords: Continuous crystal, surface treatment, small animal PET, LSO.

ÖZET

BLOK DETEKTÖR KAVRAMININ, KÜÇÜK HAYVAN PET SİSTEMLERİ İÇİN, MONTE CARLO BENZETİM YÖNTEMİNİ KULLANARAK DEĞERLENDİRİLMESİ

Küçük hayvanlar için pozitron emisyon tomografisine ait detektör tasarımı, üç tane ana faktörü göz önünde tutmayı gerektirir. Bunlar yüksek enerji çözünürlüğü, uzamsal çözünürlük ve maliyettir. En son teknoloji pozitron emisyon tomografisi detektörleri incelendiğinde, birçok araştırmacının küçük hayvanlar için olan PET sistemleri için, yekpare, blok ya da parçalı kristallerden oluşan detektörleri tercih ettikleri görülebilir. Parçalı kristallerden oluşan detektör tasarımı, yüksek uzamsal çözünürlük sağlarken, aynı zamanda pek çok yeni sorunada yol açar; örneğin, ışın toplanmasında düşüş (düşük bağlanma kesri), yoğun emek ve yüksek maliyet. Bu çalışmada, bu kısıtlamaların üstesinden gelebilmek için blok ya da parçalı kristallerden oluşan detektörler yerine, yekpare bir kristalin, yüksek çözünürlüklü küçük hayvan PET sistemleri için uygulanabilirliği araştırıldı. Bu amaç için, konum duyarlı bir ışıl elektriksel çoğaltıcıya (Hamamatsu H8711–03) bağlı bir LSO (16mm x 16mm) kristali tasarlandı. Yekpare bir kristal ile çalışırken, yüzey kaplaması ve kristal kalınlığı, detektörün ana özelliklerini belirleyen önemli faktörlerdendir. Bu yüzden, tasarlanan detektörün optimizasyonu için bu faktörlerin etkisi araştırıldı. Çalışmada, 4 farklı yüzey kaplaması (parlak yüzey + siyah boya, pürüzlü yüzey + siyah boya, pürüzlü yüzey + metakrilit + siyah boya, pürüzlü yüzey + hava), 3 farklı kalınlık (3mm-6mm-9mm) ve 41 değişik kaynak koordinatı kullanıldı. LSO kristalinin farklı yüzey kaplamaları ve kalınlıklarıyla ilgili elde edilen tüm enerji çözünürlüğü, uzamsal çözünürlük ve imge sıkıştırma sonuçları sunuldu. Benzetimler, DETECT2000 benzetim paketi kullanılarak gerçekleştirildi.

Yüksek uzamsal çözünürlük, bir PET detektörü için en önemli parametredir. Yapılan çalışmada, "pürüzlü yüzey + hava yüzey kaplaması" en yüksek uzamsal çözünürlük, ancak zayıf bir imge sıkıştırması sonucu vermiştir. Ancak, bu beklenen düzeyde olmayan sonuç, bazı özel istatistiksel konumlandırma algoritmalarıyla iyileştirilebilir.

Anahtar sözcükler: Yekpare kristal, yüzey kaplama, küçük hayvan pozitron emisyon tomografisi, LSO.

TABLE OF CONTENTS

LIST OF FIGURES

LIST OF TABLES

LIST OF SYMBOLS

α	Alpha particle
Bq	Becquerel
β	Beta particle
c	Velocity of light
C_{bs}	The backscatter spike constant
C_{sl}	The specular lobe constant
C_{ss}	The specular spike constant
C_{dl}	The diffuse lobe constant
cm	Centimeter
$\vec{d}_i$	Direction vector of incident photon
$\vec{d}_r$	Direction vector of reflected photon
$\vec{d}_t$	Direction vector of refracted photon
E	Energy
e-	Electron
e^+	Positron
FDG	2-[F-18]-fluoro-2-deoxy-D-glucose [-F-18-FDG]
I_0	The incident light intensity
kg	Kilogram
λ	Wavelength
m	Mass
n_i	Refractive indices of the incidence media
n_t	Refractive indices of the transmittance media
n_1	Index of refraction of incidence medium
n_2	Index of refraction of the transmission medium
R	Reflection
SA	The standard deviation of the distribution of the angle of the local normal vectors with the global normal.
Si	Silicon
T	Transmittance

τ	Time
θ_i	Angles of incidence
θ_s	Polar angle of the scattered light
θ_t	Angles of transmittance
X_i	The x-coordinate of the interaction
$X\gamma$	The x-entrance coordinate
Y_i	The y-coordinate of the interaction
$Y\gamma$	The y-entrance coordinate
Z_i	The z-coordinate of the interaction

LIST OF ABBREVIATIONS

APD	Avalanche photodiode
BaF_2	Barium fluoride
BGO	Bismuth germanium oxyde
B.F.	Back face
Ce	Cerium
CFOV	Central field of view
Cm	Centimeter
CsF	Cesium Fluoride
CT	Computerized tomography
CsI:Tl	Thallium-doped cesium iodide
eV	Electron-volt
F.F	Front face
FWHM	Full width at half maximum
FWTM	Full width at tenth maximum
FOV	Field of view
GA	Ground + Air
GB	Ground + Black
GM	Ground + Methacrylate
GRIT	Gamma-ray interaction tracking
GSO	Gadolinium oxyorthosilicate
KeV	Kilo electron-volt
Kg	Kilogram
LGSO	Lutetium gadolinium oxyorthosilicate
L_i	Calibrated light yield
LPS	Lutetium pyrosilicate
LSF	Line spread function
LSO	Lutetium oxyorthosilicate
LuAP	Lutetium aluminum perovskite
LuAP:Ce	Cerium doped lutetium aluminum perovskite
LuAG	Lutetium Aluminum Garnet
Max.	Maximum

Metha.	Methacrylate
MeV	Mega electron-volt
Min.	Minimum
Mm	Millimeter
MRI	Magnetic Resonance Imaging
MRS	Metal-resistor-semiconductor
MWPC	Multi wire proportional chamber
NaI :Tl	Thallium-doped sodium iodide
NEMA	National Electrical Manufacturers Association
Nm	Nanometer
OPHS	Optical pulse-height spectrum
PB	Polished + Black
pdfs	Probability density functions
PET	Positron emission tomography
PMT	Photomultiplier tube
PS-APD	Position sensitive avalanche photodiode
PSD	Position sensitive detector
PSF	Point spread funcion
PS-PMT	Position sensitive photomultiplier tube
RatCAP	Rat conscious Animal PET
RC	Reflection coefficient
S.F.	Side face
SiPM	Silicon photomultiplier
Si-SSPM	Silicon semiconductor structure photomultiplier
SPECT	Single photon emission computed tomography
UK	United Kingdom
UV	Ultraviolet
YAP	Yttrium aluminate perovskite
YAP: Ce	Yttrium aluminate perovskite, cerium activated

1. INTRODUCTION

In order to see objects invisible to the naked eyes, especially the interior of biological matter, mankind for a very long time made enormous efforts, the first fruit of which was the microscope and the second the X-ray machine. (1895)

In 1898, in France radium was separated by Pierre Curie and Marie Curie. H.A.Becquerel discovered that crystals of uranium salt emit radiation capable of penetrating opaque materials, affecting photographic film. (1899)

Since Becquerel's discovery, many researchers have tried to find new ways to take an image of invisible objects within biological matters benefiting from radioactive material radiations.

With the realization of positron detection in 1950, these studies gained new and different impetus. As a result of this, production of a positron emission tomography (PET) has begun.

On the other hand, from detection materials to sensors, detector designs to recording of the results, many investigations have been made, up to present day. In addition to these, the hastiness of the PET producers caused many complications.

After examining all the studies by realist investigators, it is not possible to produce a satisfactory PET system clarifying before many unknown points related to positron emitting detection systems for diagnosis.

The aim of this study is to develop a low cost and more satisfactory dedicated PET detector module for small animal brain imaging using a conventional continuous Lutetium Oxyorthosilicate (LSO) crystal coupled to a position sensitive photomultiplier tube (PS-PMT). On the other hand, it is expected that the main characteristics of continuous crystal detector (especially energy and spatial resolution) to be strongly related to the crystal thickness and surface treatment. Then, the power of these relations on the contemplated detector design is investigated by using DETECT2000 simulation package.

During this study, we have felt a need for considering image compression too.

1.1 Outline of the Thesis

Chapter 1 introduces the thesis. In Chapter 2, brief information on gamma ray detection systems is given. Theory of production, detection and collimation of annihilation radiation, physical properties of scintillator materials used for PET and sensors for gamma ray detection systems are discussed in Chapter 3. In Chapter 4, an overview of current dedicated animal PET systems and their technological properties are presented. Material and method are introduced in Chapter 5. The simulation results are given in Chapter 6. Chapter 7 is a summary of our concluding remarks and also our decision on future work.

Appendix A presents classical knowledge about Positron Emission Tomography. Definition and types of scintillators used in PET with their characteristics are explained in Appendix B. The used PC configuration is given in Appendix C. Appendix D gives information about DETECT2000 simulation package. Introduction to Monte Carlo Method is in Appendix E. An example input and output files are given in Appendix F. In Appendix G, energy and spatial resolution and image compression are explained. The special code written by using Perl for quantum efficiency of the PS-PMT is given in Appendix H.

2. HISTORICAL EVALUATION

2.1 Historical Evaluation: Paramedical

The early part of the imaging techniques history was well reported by O. TERNAR. [1] First imaging techniques dates back to Leonardo da Vinci (1452-1519), the well-known artist who first used the pinhole camera called “camera obscura” [2]. Then, Giambatista Della Porta (1593-1615) modified the camera obscura to the similar form known today as the pinhole camera and it is referred in many books as Porta’s camera [3]. This subject also goes back to A.W. Godspeed who produced in 1890 shadow photographs of ordinarily opaque objects using cathode rays from discharge tubes [4].

In 1895, W. C. Roentgen covered a sheet of paper with barium platinocyanide and showed that it glittered brilliantly near X-ray discharge tube [4].

In 1896, the pinhole camera principle was first used by Roentgen in order to visualize a source of ionizing radiation. Roentgen got the projected image of the anode of one of his X-ray tubes by the help of a hole in a sheet of metal on a photographic plate [5]. Within the same year, H. A. Becquerel discovered the radioactivity in France [6].

In 1898, also in France, radium was separated by Pierre Curie and Marie Curie [7,8]. H. A. Becquerel discovered in 1899 that crystals of uranium salt emit radiation capable of penetrating opaque materials, affecting photographic film and discharging an electroscope [4]. P. Villard showed in 1900 that radioactive materials emit a third kind of radiation. This was the gamma ray that has great penetrating power, affects photographic film, but is not deflected by a magnet [4].

Danlos and Block in 1901 used radium to cure a human being [9]. F. Dessauer in 1906 measured the dose of radiation at various places. He took a bucket of water, put a radiation source in it and indicated the lines of equal dose and formed an isodose chart [10]. Beaudoin and Ceytre published in 1908 “La Radiumtherapie” in Paris [11].

E. London informed in 1909 that the distribution of radioactive elements in biological material may be studied by using their effects on photographic film [4].

E. Rutherford and A. N. da C. Andrade in 1914 showed that gamma rays could be deflected by X-ray deflecting crystals [4]. At the same time, F. Dessauer insisted that X-rays were similar to gamma rays [12].

Development of nuclear science gained speed by the amazing discovery of E. Rutherford. In 1919, According to his discovery, the structure of matter could be altered by bombarding elements with alpha particles from radium (1919). He also found that when nitrogen was bombarded with alpha particles coming from radium, it transformed into nuclei of oxygen [4].

Rutherford succeeded the first deliberate artificial transformation of an atomic nucleus. In the 1920's physical scientists, benefiting from the Rutherford's discovery, kept on their nuclear studies. They soon noticed that radium had serious limitations as a source of sub-atomic projectiles. First of all, only the alpha particles from radium were effective in nuclear transformation. Also, the number of alpha particles was not sufficient for desirable experimentation. Moreover, the energy and penetration of its alpha particles were severely limited [4].

In 1923, A. H. Compton showed that when X-rays fall on carbon or other materials of low atomic weight, the scattered radiation includes some rays of longer wavelength than the incident X rays [4].

A. Lacarsague and J. Lattes informed in 1924 that radioactive polonium can be injected into various organs to study its effects [4]. The Geiger-Mül1er counter was invented by f and Mül1er in 1928 in Germany [13].

P.A. M. Dirac in 1930 predicted the existence of a particle similar to the electron but, carrying a positive charge [4].

E.O. Lawrence in 1930 showed in the U.S.A. that a strong alternating magnetic field could transfer added energy to particles moving in a spiral path (cyclotron) [4, 9, 13]. Within the same year, in England, artificially accelerated particles were used for first nuclear transmutation by Cockcroft and Walton [9, 13]. Also in the same year, C. Y. Chao suggested that the gamma rays can be converted into positron-electron pairs, when matter absorbs high-energy gamma rays at a greater rate then expected [4].

In 1932, experimental physicist, C.D. Anderson proved the correctness of Dirac's prediction by observing experimentally that cosmic rays include particles with the mass of electrons (e^-) but move in a strong magnetic field along a path indicating their having a positive charge. He called these particles "positrons" (e^+) or positive electrons. [4, 54]

J. Thibaud and F. Joliot showed that in 1933 when a positron and electron could combine, they only produce the annihilation energy [3]. In 1934, artificial radioactivity was discovered by F. Joliot and Irene Curie in France [13, 14]. Within the same period, Hevesy and Hofer realized the first clinical study related with stable isotopes. They used deuterium to examine the total water content and half-life of water molecules in their own bodies. This is the first application of the isotope dilution principle and has found widespread application area in clinical studies [7].

P.A. Cerenkov in 1934 showed that water and other transparent substances emit a weak bluish-white shine when exposed to gamma radiation [4]. In 1935, coincidence counting techniques were used to study radioactive decay by Bothe and Von Baeyer in Germany [13].

In the fall of 1935 an artificially produced radioisotope was first applied to a biological problem. O. Chiewitz and G. Hevesy used radioactive phosphorus as a tracer to investigate the distribution and excretion of that element in rats and to study the absorption of this element by plants [4, 9].

O. Dessauer in 1936 showed that a thin paste of zinc sulphide and zinc oxide in castor oil, when spread on a metal plate covered with a sheet of mica and immersed in salt water, would produce electroluminescence [4].

In 1939 nuclear fission was discovered by Hahn and Strassmann in Germany and in the same year a large section of the Kaiser Wilhelm Institute in Berlin had been turned into the research center on uranium [4, 13].

On December 2, 1942 E. Fermi and his co-workers at the University of Chicago achieved the first self-sustained nuclear chain reaction [4, 9, 13].

In 1945, P. J. Van Heerden discovered that certain crystals, normally poor electrical conductors, gain conductivity according to the intensity of ionizing radiations to which

they are exposed; he showed that individual ionizing particles may be counted by amplifying the pulses of current produced when certain crystals are exposed to these particles and these crystals are called as crystal counters [4, 15].

M. Blau and B. Dreyfus in May 1945 used a photocolorimetric method for measuring the alpha particles. Basically, this method included the measurement of the fluorescent light produced by alpha particles on zinc sulphide activated with copper screen with PMT and comparing the light produced with a standard light source.

The importance of this work was to show that the photomultiplier tube might be used in the measurement of activity of the radioactive materials [16] (Figure 2.1)

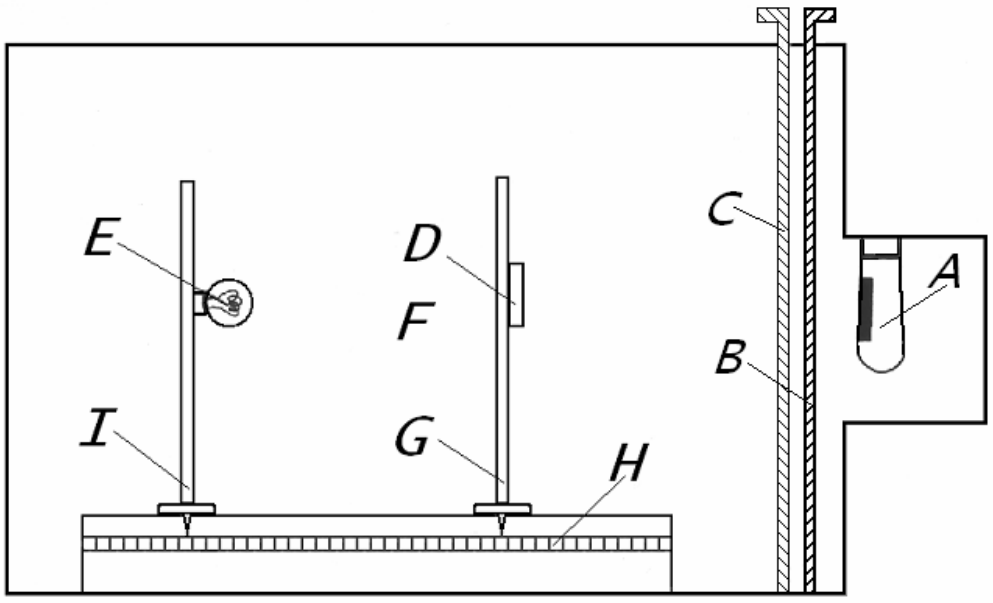

Figure 2.1 The first use of the phototube in radioactive measurement [16].

In 1947 Kallman and Broser in Germany, and Coltman and Marshall in the U.S.A. proved that when alpha (α) or beta (β) particles fall upon a crystal of naphthalene, anthracene or calcium tungstate, light pulses are emitted, without potential applied to the

crystal [13-15, 17-18]. After than, Kallmann used the major advance of this technique and he found that scintillations produced in large transparent blocks of naphthalene by beta rays and gamma rays could be detected with a photomultiplier.

In the same year, M. Deutsch showed that such screens several centimetres thick gave a detection efficiency of 20% for l.2-MeV gamma rays and even higher for lower-energy radiations [19].

In 1948 P. R. Bell discovered that anthracene was a more suitable phosphor and it gave scintillation pulses about five times the amplitude of those from naphthalene.

He also found that fast neutrons could be detected by the scintillations caused by recoil protons within the phosphor [20]. In the same year R. Hofstadter discovered that sodium iodide crystals activated with thallium gave even larger pulses than anthracene and, because of the high photoelectric absorption of the iodine constituent, could be used for gamma-ray spectroscopy of very weak sources [21].

D.B. Copeland and E. W. Benjamin in 1949 used a pinhole camera for gamma-ray emitters [22].

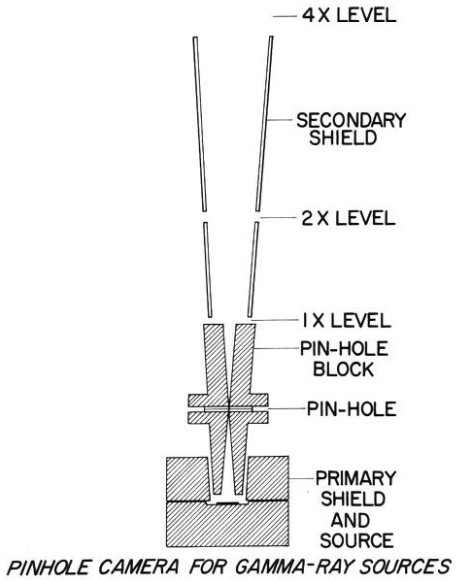

Figure2.2 The Pinhole Camera of Copeland and Benjamin for gamma-ray sources [22].

G.T. Reynolds, F. B. Harrison and G. Salvani in 1950 reported that scintillation pulses from certain organic solutions were comparable in magnitude with those from anthracene.

Thus, large volumes of transparent liquid phosphors could be used as gamma-ray counters of very high efficiency [23].

Johannson in 1950 and Bair and Maienshcein in 1951 developed the scintillation pair spectrometer in which the two 0.51 MeV quanta emitted in opposite directions in positron annihilation were used to separate the pair production from the other gamma ray absorption processes.

In Johannson's spectrometer, the primary gamma radiation is incident on the crystal "A" of a scintillation counter. The crystal "A" is surrounded on opposite sides by two large crystals "B" and "C", designed to capture the annihilation radiation. Coincidences between the output pulses from the photomultipliers viewing "B" and. "C" are used to a gate for the signal pulses from the central counter, which responds to an energy.

$$Epp = (E_I - 1.02)\ MeV \qquad (1.1)$$

The central crystal "A" must be sufficiently large to give reasonable gamma-ray detection efficiency with a thickness greater than the range of the electron-positron pair. On the other hand, it must not be so large that an appreciable number of the annihilation quanta are absorbed.

The side crystals "B" and "C" should be as large as possible so as to capture most of the annihilation quanta.

Johannson also showed that a large volume organic solution phosphor might be more suitable (24).

In the following section, the application of these discoveries into the medical field is reviewed briefly.

2.2 Historical Evolution: Medical

In 1950, human being saw the first various fast-measuring devices in the medical field for the measurement the radioactive materials. W. V. Mayneard and E. H. Belcher in 1950 explained how a scintillation counter might be used to examine various simple sources, and confirmed the theory that such a multi-functional system could measure the approximate thickness of the radioactive materials [15].

2.2.1 Collimators

Another interesting feature of their publication is that it explained the importance of collimators, and then different types of collimators were designed for clinical use. These collimators can be classified as below [25, 26].

I. Single – hole collimator
   A. Cylindrical
   B. Conical inverted
   C. Conical obverted

II. Slit collimator

III. Multichannel collimator
   A. Focused
      1. Honeycomb cone
         a. Several to 280 holes
         b. Hexagonal or round shaped hole
      2. Spiral plug
      3. Split plug
   B. Non-focused

2.2.2 Area Scanners

In 1951, Benedict Cassen invented a new mechanical device to route the detector over the neck to gather as much information in as a possible short time and to transfer it to a piece of paper in the form of dots. Cassen called this “Scanning Technique” [27].

Cassen’s technique was so useful diagnostically that it was immediately developed by many commercial companies; many different machines were made that were particularly adapted to learn the size, shape, and location of the thyroid gland. This technique is called as “Area Scanning”. When the capacity of Cassens machine was realized, it was thought that the sweep speed of the probe and the traverse line spacing gave inaccurate results in areas of very high or very low radioactivity, and also in many situations it was desired to have different sweep speeds and different spacings of the traverse line for the probe. Therefore, in many machines the movement of the probe could be regulated by the help of the Cassen’s machine in those years [10, 27-28].

In April 1957 in Canada, Reid and Johns [29], in brain scanning, developed a rotational probe system that followed the special shape of the organ.

David B. Kuhl [30] in 1958 used the same idea with a little different form in liver scanning and called these forms of scanning “rotational scanning” and the flat form of scanning “planar scanning”.

2.2.3 Depth Scanners

During the development of area scanners, it was learned that, especially for localization of tumors, area scanners are not sufficient and collimators do not have a good enough focusing form. Therefore, researchers may use more than one scanner at the same time on different angled planes. This category of techniques is being called depth scanning or three-dimensional scanning [10, 31, 32, 33, 34].

2.2.4 Temporal Scanning

When someone is able to visualize the deposition or movement of radioisotopes in the body over a period of time, this is another type of scanning called “temporal scanning.” This is not a four-dimensional scanning; it is only at the fourth dimension.

2.2.5 Linear Scanners

During the development of Cassen’s technique for area scanning, E. E. Pochin in 1954 in England [35, 36] made a rapid and quantitative measurement of the radioisotope distribution throughout the body.

He used a collimated Geiger-Müller tube with a sensitive length of about 8.5 cm and passed this system slowly down a track over a subject lying on a bed. At each position over the subject, it recorded the radioisotope content of the whole width of the body, but only a short section of its length. He called it profile counting.

In June of 1956 Concannon and Bolhuis [37] in Chicago modified Pochin’s method by using a single scintillation detector with a well-collimated lead head with a transverse wedge-shaped slit. Their work resulted in a more sensitive counter; they called it total-body scanning.

2.2.6 Total-Body Scanners:

In California H. O. Anger [38], with the help and encouragement of Dr.C. A. Tobias, built in 1953 a special scanner device for rapidly scanning the entire body. Anger used in this scanning device ten scintillation counters to obtain a good record in a relatively short time. This provides a picture of the source of gamma-emitting activity in a small area. Human subjects can be scanned from head to foot in about 45 minutes and laboratory animals in a proportionately shorter time.

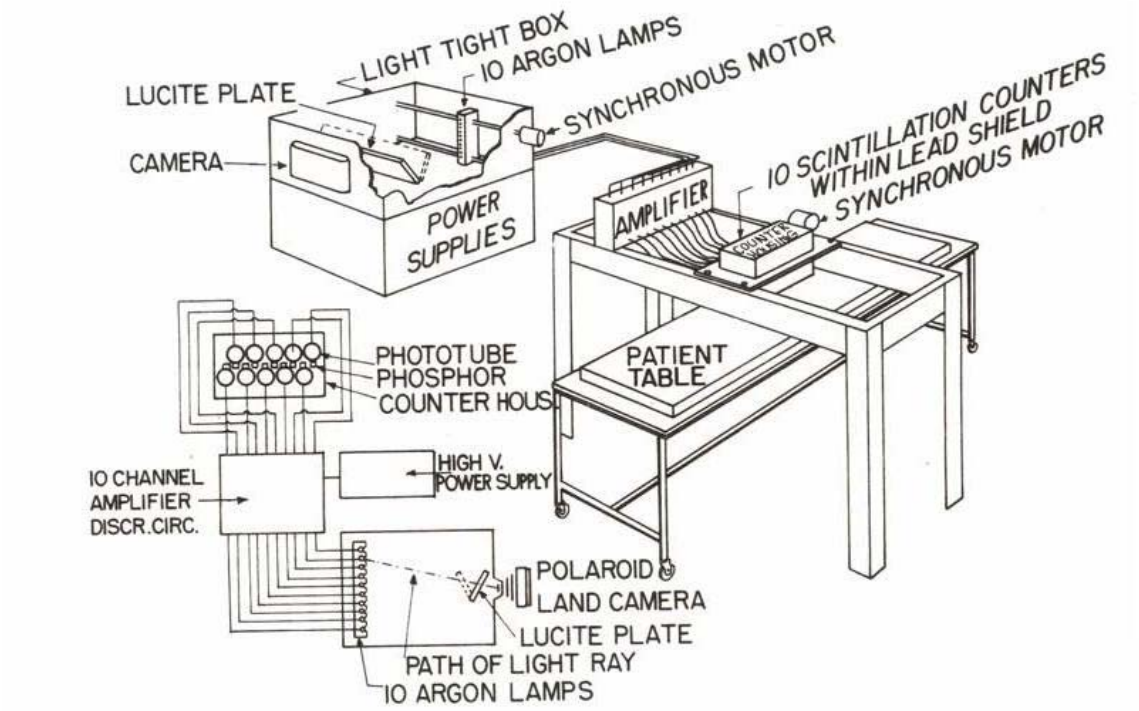

Figure 2.3 Total-body scanner of Anger [38].

The active areas in the subject are shown as white areas on the resulting gamma-ray picture. Anger's instrument has wide application both in tracer research with gamma-emitting isotopes and in clinical diagnosis of thyroid lesions and other conditions.

2.2.7 Positron-Emitting Isotope Scanners:

The development of the scintillation counting technique saved researchers from the difficult applications of Geiger-Müller tube and beta-emitting isotopes for in vivo external counting. Also, external counting is often limited to a few gamma-emitting isotopes and additionally some gamma-emitting isotopes, like-more distributed in organism than investigator's desire and produce some difficulties in the localization of a hot area. In the same kind of situation, profiting by the development of scintillation counting and by using positron-emitting isotopes, somebody has practically eliminated these difficulties [39-40].

In 1951 Wrenn, Good, and Handler published a preliminary report discussing the possible use of positron-emitting isotopes [41]. In the same year the results of Sweet's and

Brownell's initial studies on positron-emitting isotopes were described as part of a more general report by Sweet [42]. The first positron-emitting isotopes scanner in the medical field was prepared in 1953 by Brownell and Sweet, also used by these investigators. Their scanner has only two detectors and a special circuit [43]. The positron-emitting isotopes scanner is similar in form with Johannson's scintillation pair spectrometers introduced in 1950 and was used in the medical field after 1955 [44].

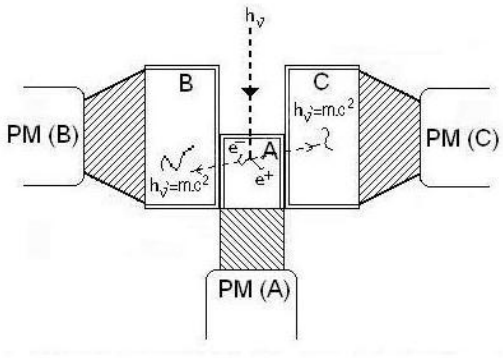

Figure 2.4 Scintillation Pair Spectrometer of Johannson [24].

Later on Brownell et al. developed a new positron-emitting isotopes scanner - like their first positron-emitting isotopes scanner by using two detectors and a special coincidence circuit, which has a two micro-second resolution time [45].

Finally, in 1962, Rankowitz, Robertson, Higinbotham, and Rosenblum, by using in a stationary circular array of 32 scintillation detectors, built a new positron scanner for locating brain tumors [46].

2.2.8 Camera Systems:

When someone designs a recording system, the basic problem to be overcome beside from the purely technical considerations, is to achieve act of seeing. To reach a good solution, many researchers often prefer to use photography technique. Realizing the advantages of such a system, in 1952 Anger [47] built the Anger I camera for in vivo studies by improving the "pinhole camera for gamma-ray sources" of Copeland and Benjamin.

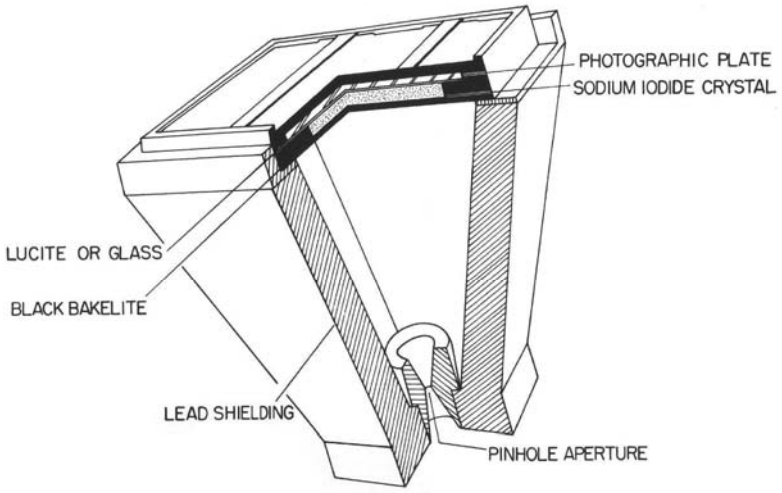

Figure 2.5 First Gamma-ray pinhole camera of Anger [47].

In 1955 in France, Kellershohn and Pellerin designed a scintillation grid for photographic localization of gamma emitters [48, 49].

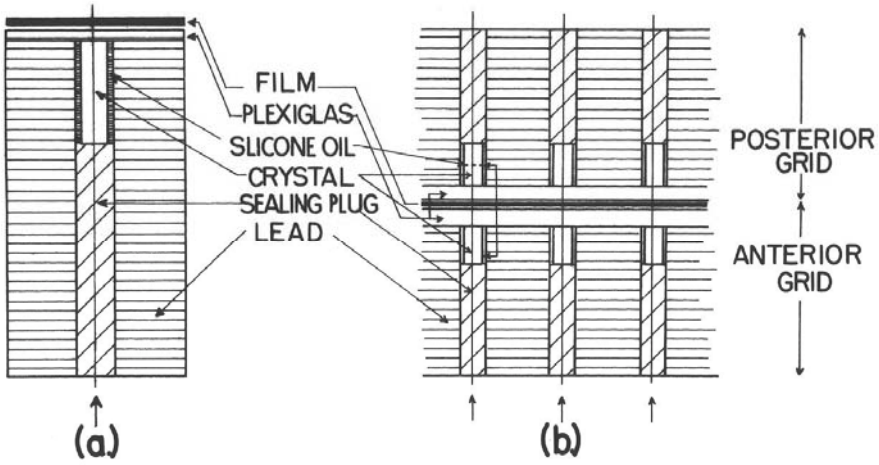

Figure 2.6 Scintillation grids of Kellershohn and Pellerin [48].

Also, the same people in the same year used an image-intensifier tube with a multihole straight collimator (= grille collimatrice) and achieved a device for the same purpose [50].

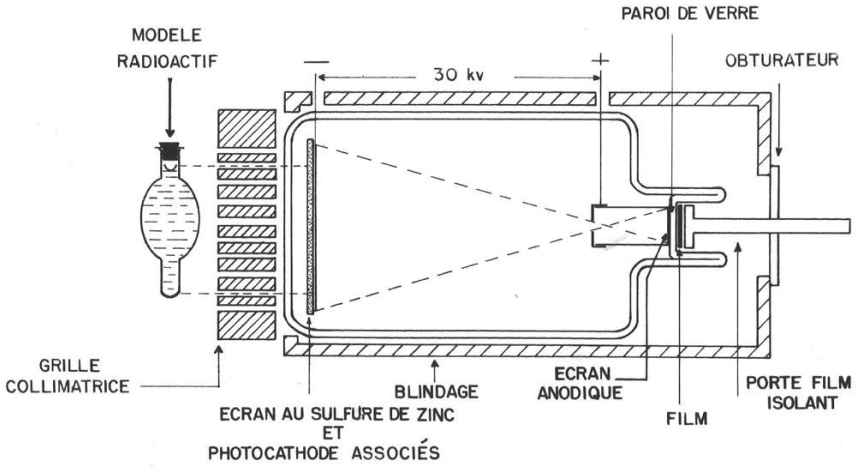

Figure 2.7 Gamma – ray camera with image amplifier of Kellershohn and Pellerin [50].

In 1957, H. O. Anger developed a new and more sensitive gamma-ray camera [4, 51]. It consisted of a lead shield with a single-hole aperture a scintillating crystal within the shield, viewed by a bank of seven photomultiplier tubes, a special signal matrix circuit, a pulse-height selector and a cathode-ray oscilloscope. He called it a "scintillation camera".

In 1959, Anger, by modifying the "scintillation camera" designed and built two different cameras for location of positron-emitting isotopes.

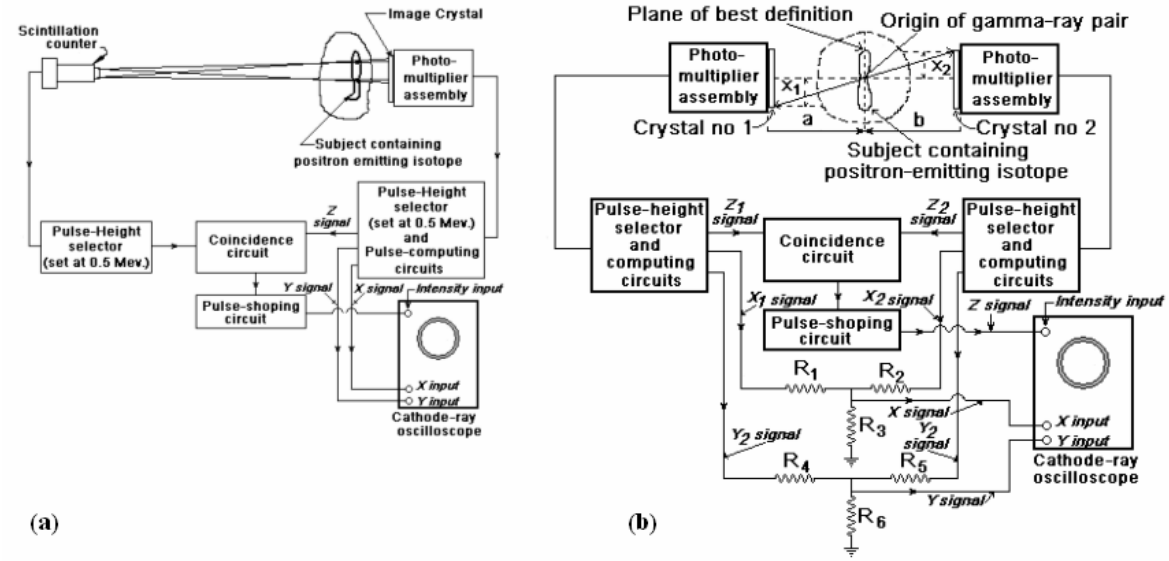

Figure 2.8: (a) Block diagram of single-crystal positron camera of Anger. (b) Block diagram of twin-crystal positron camera of Anger [5].

In 1960, M.A. Bender and M. Blau [52] in Roswell Park Memorial Institute of Buffalo, by using the data transfer system of Anger's positron camera, began to prepare a new camera and they called it an autofluoroscope.

In May 1963, O.Ternar prepared a new gamma-ray camera using two scintillation crystals one of which is connected to a PM tube, the other one is connected to a five-stage image intensifier and two video systems as shown in Figure 2.9.

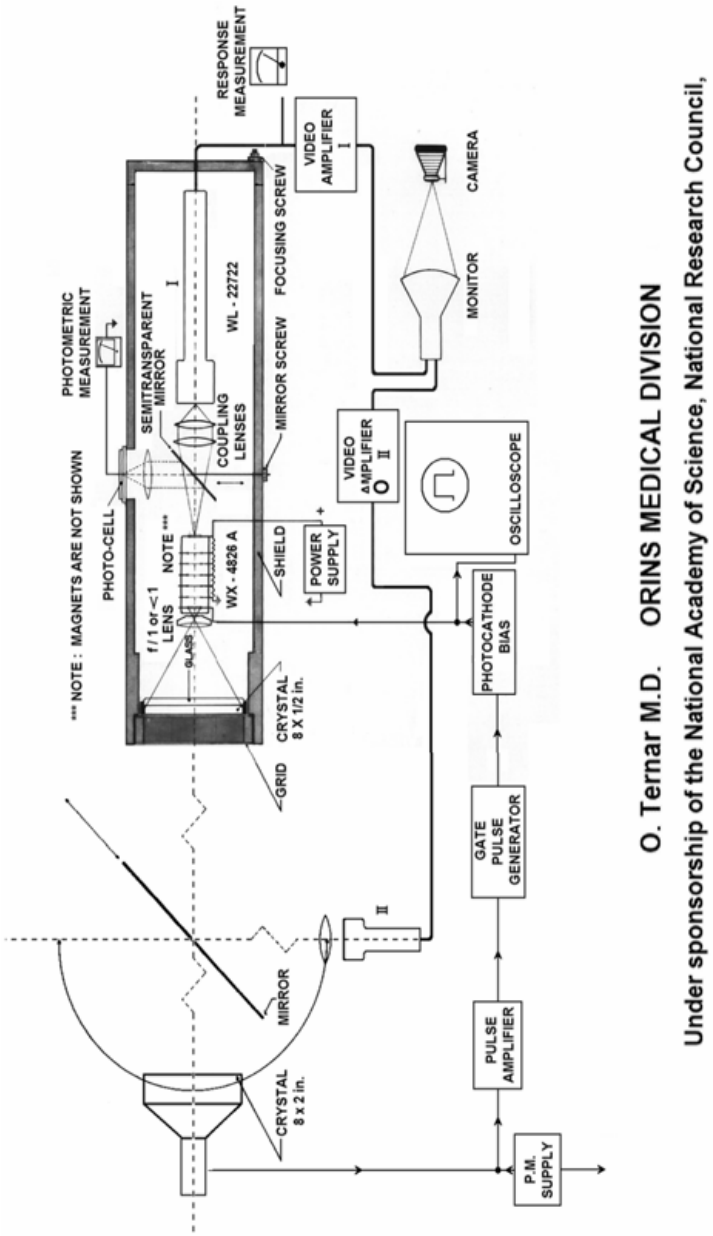

Figure2.9 O.Ternar Gamma-rays camera [1].

2.2.9 The Renaissance of PET Imaging Systems

In the early 1960s to the mid 1970s, several versions of the single pair coincidence systems were built including a commercial version various groups of investigators. Also, hybrid scanner was developed. At the same time, another group of investigators made enormous efforts to produce short-lived positron emitting isotopes benefiting from cyclotron, because according to this group, positron emitting isotopes have more chance to obtain high sensitivity and better resolution than the others [53, 55, 56].

The Washington University groups of Phelps, Hoffman, Mullani and Ter-Pogossian used 24 NaI (Tl) detectors of a hexagonal array. Examined objects were placed on a computer-controlled turntable at the center of and perpendicular to the plane of the hexangle. This device was called as PET II.

In 1975, same group using 48 NaI (Tl) detectors built a new device called PET III.

During the late 1970s and 1980s advancements of PET cameras were realized using ring detector geometries, different detector materials such as Bismuth-germanium oxyde (BGO) and Cesium fluoride (CsF).

After 1980s, many investigators and firms built different types of PET. This period can be accepted as the Renaissance of the PET studies.

Also in this period, they remembered the difference between photograph and image, again. In other words, they understood the insufficiencies of image reconstruction methods [57, 58, 59].

In 1980s, some realistic researchers checked all the results against the PET producers and asked themselves that why they had spent a lot of money and time for these works, because, despite of all efforts, there have been no any believable and satisfactory PET systems yet. Then, they started to search cheaper and more satisfactory methods and decided to use Monte Carlo Simulation Method.

Thus, a program (DETECT) for modelling optical properties of scintillators was appeared in1988 [57].

DETECT have been used by many investigators for a long time. However, modelling optical properties of scintillators were insufficient to solve all PET problems.

In 2000s, Monte Carlo codes have been developed for positron emission tomography (PET) [58].

Benefiting from upper layer of the Geant4 (nuclear physics code), GATE Monte Carlo simulation package was designed and adapted for nuclear medicine more specifically to fulfil its role as a simulation platform for PET and Single Photon Emission Computed Tomography (SPECT) [58, 59, 60].

3. THEORY

3.1 Production of Annihilation Radiations

A positron is a particle identical, in all respects, to an electron, except that it has a positive electric charge rather than a negative one. Thus, a positron is an antimatter electron. When a positron and an electron meet, the mass of each particle is completely transformed into energy according to Einstein's well-known equation, $E= mc^2$. If someone does the mass conversions, he sees that each electron mass is equivalent to 0.511 MeV of energy. Thus, two photons, each with energy of 0.511 MeV, are produced by each positron–electron interaction, with the photons leaving the site of the interaction almost exactly 180° apart (the slight deflection from 180° is from conservation of the residual kinetic energy each particle possessed at the time of the positron–electron interaction). (Fig.3.1) The unique form of reaction that produces the two photons called an "annihilation event'' and the two photons are called ''annihilation photons'' [61].

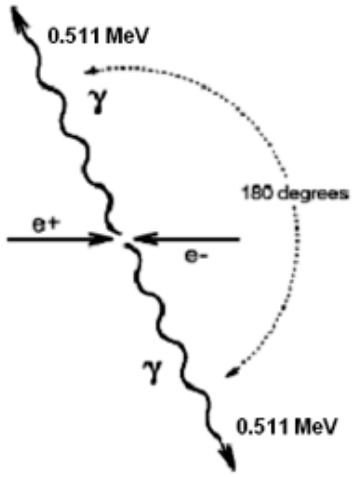

Figure 3.1 Pair production (Annihilation event) [61].

The detection of these annihilation photons (gamma rays) is the foundation for positron emission tomography (PET) imaging. (see Appendix A for details of positron emission tomography).

3.2 Detection of Annihilation Radiation

There is no any detection principle difference between each rays of pair production and the other gamma rays (Figure 3.2).

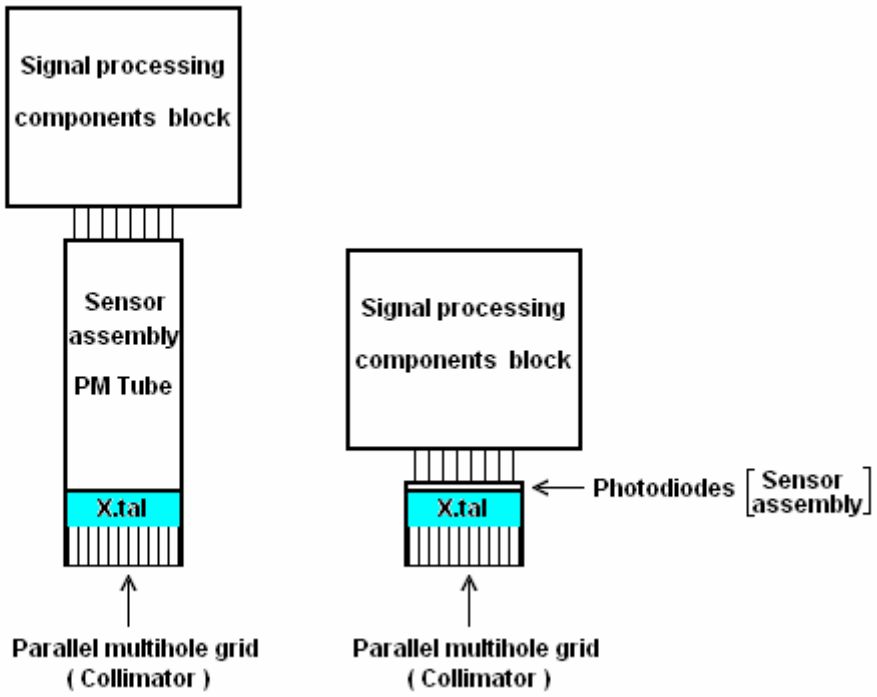

Figure 3.2 The simple schematic of two different type gamma ray detector configurations.

As seen in Figure 3.2, one gamma ray scintillation counter has four cardinal parts;

a) Collimator,

b) Scintillation crystal,

c) Sensor,

d) Counting assembly.(Signal processing components block)

3.2.1 Collimation of Annihilation Rays

Energy of annihilation ray is 511 keV, but this energy is fairly high. Therefore, preparation a good collimator for this energy level needs an extreme technique and care. On the other hand, the construction and shape of these collimators can be varied depend on the usage purpose. Certain types of collimators mentioned above are seen in Figure 3.3 (a,b,c) [62].

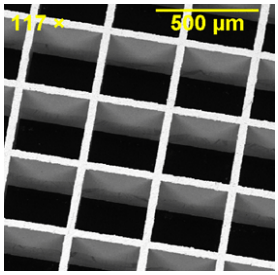

3.3 (a)

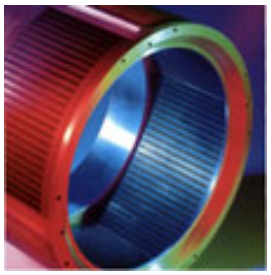

3.3 (b)

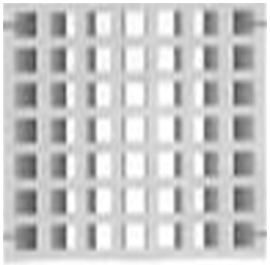

3.3 (c)

Figure 3.3 Various collimators **(a)** A special gold collimator, **(b)** Cylindrical multihole collimator, **(c)** Partial enlargement of cylindrical collimator [62].

3.2.2 Scintillation Crystal

A scintillator is a high density, transparent material which emits visible or ultraviolet light when x- or γ-ray interaction happens to interior part. Each gamma ray detection system must have an energy transformer material for radiation detection. Most commonly used gamma ray energy transformers are solid, monocrystal chemical compounds. However, to obtain a good image, these crystals should be very thin.

On the other hand, thin crystals have a very low detection power. This obligation creates another difficulty to acquire a good image. The researchers can partially eliminate this unpleasant condition by increasing density of the used crystal.

According to published papers, the most common crystals used for PET systems are informed with almost full details summarized in Table 3.1 [63].

Table 3.1 Physical properties of scintillation materials used for PET [63]. (The details are given in Appendix B)

Physical properties of scintillator materials used for PET

Scintillator material	Composition	Density (g/cm)	Z_{eff}	Attenuation length for 511-keV gammas(mm)	Probability of PE(%)	Light output (ph/MeV)	Decay time (ns)	Scin. emission wave-length (nm)	Hygroscopic	Refractive index
BGO	$Bi_4Ge_3O_{12}$	7.1	75	10.4	40	9,000	300	480	No	2.15
LSO	Lu_2SiO_5:Ce	7.4	66	11.4	32	30,000	40	420	No	1.82
NaI:Tl	NaI:Tl	3.67	51	29.1	17	41,000	230	410	Yes	1.85
CsI: Tl	CsI:Tl	4.51	52	22.9	21	66,000	900	550	Slightly	1.80
GSO	Gd_2SiO_5:Ce	6.7	59	14.1	25	8,000	60	440	No	1.85
LGSO	$Lu_{1.8}O_2SiO_3$:Ce					23,000	40	420	No	
LuAP	$LuAlO_3$:Ce	8.3	64.9	10.5	30	12,000	18	365	No	1.94
YAP	$YAlO_3$:Ce	5.5	33.5	21.3	4.2	17,000	30	350	No	1.95
LPS	$Lu_2Si_2O_7$:Ce	6.2	63.8	14.1	29	30,000	30	380	No	
LuAG	$Lu_3Al_5O_{12}$:Ce	6.7	62.9	13.4	27	5,606		510	No	
BaF_2	BaF_2	4.89	54	20.6		65,000	<1	220	No	1,54

PE, Photoelectric effect

3.3 Sensors for Gamma Ray Detection Systems

511 keV Gamma Ray detection system sensors can be collected in four groups:

I Photomultiplier tubes (PMT),

II Special photodiodes,

III Multiwire proportional chambers (MWPC),

IV SiPM (Silicon photomultiplier).

I. Photomultiplier tubes: They are divided into two main groups:

I-a) Photomultiplier tube: It was invented on August 4, 1930 by Soviet-Russian physicist and engineer L.A.Kubetsky. [64] In 1933-34 L.A.Kubetsky has developed a number of photomultiplier tubes with Ag-O-Cs photocathodes and circular secondary electron emitters made also from Ag-O-Cs. The photomultiplier tubes consisted of photocathode and multi-stage electron multiplier system including constant magnets for electron focusing because electrostatic electron optics was not developed well at that time.

The amount of light which is produced from a single scintillation is very small, so, classic sensor types can not be used in PET systems. To overcome this problem, instead of classic detector types, PMTs are widely used in commercial PET scanners. PM tubes composed of multiple metal dynodes put at increasing voltages. When a photon collides with a photocathode, it turns into energetic electrons. These electrons are then accelerated toward the next dynode. As a result, millions of electrons are detected for each photon that hits the photocathode of the PM tube. A typical scintillation event is in the order of the micro-ampere [66].

It is surprising that up to now the majority of physics community in the west has deepest conviction that the first PMT was developed by V.K. Zworykin et al. at RCA in 1936 [64].

There is practically no mentioning of L.A.Kubetsky name in English scientific literature [64]. After 1938, the most widespread usage of PM tubes has begun.

I-b) PS-PMTs (Position sensitive photomultiplier tubes): Position sensitive PM tubes one class of PMTs. They are able to both detect whether or not photons hits the detection surface and also encodes the position of the incoming photons. The electron detection is done by multiple anode wires which go along the length and width axis of the PMT and the obtained final signal distribution shows the origin of the light photon. By using PS-PMTs, it is likely to have one or more scintillation material coupled to one sensor. This approach is cheaper and also permits the new scintillation detector designs.

PSDs (Position Sensitive Detectors) were put on the market in 1979 [65]. Construction and working principle of PS-PMTs are given by Glenn F. Knoll with full details [66].

II. Special photodiodes: Photodetectors were well-known and used by the firstly formed alive single cell organisms billion and billion years ago. First commercial photocell was produced by Westinghouse in 1925. The history of special photodiode for a gamma ray detection system goes back to 1988 in CERN. Today many different types of photodiodes have been produced. Some of them are suitable for gamma ray detection systems, but they have not been preferable widely yet due to their high noise problems [67].

III. Multiwire proportional chamber (MWPC): The principle of MWPC is similar to Geiger Müller Counter (see Figure3.4) [68].

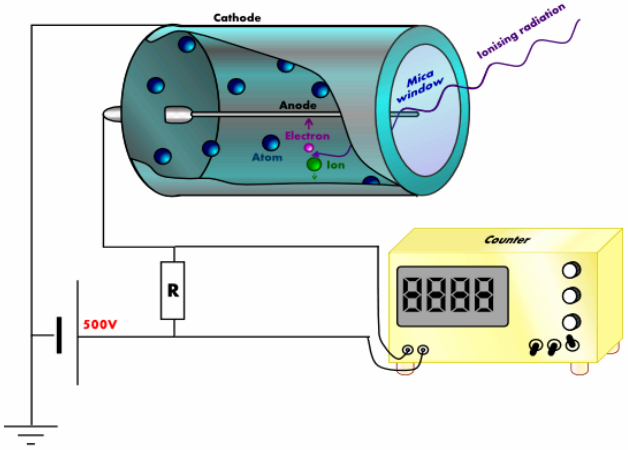

Figure 3.4 The schematic presentation of a Geiger Müller tube [68].

Geiger Müller tube has only one anode wire whereas MWPC whose schematic representation is shown in Fig 3.5 has more than one. MWPC has been borrowed from high energy physics technology and it can be seen in HIDAC PET systems. Detection power of this system depends on the number of the anode wires within a unit area. This technique was discovered by Georges Charpak [69]. His pioneering work was published in 1968 in CERN and he was awarded the Nobel Prize in 1992.

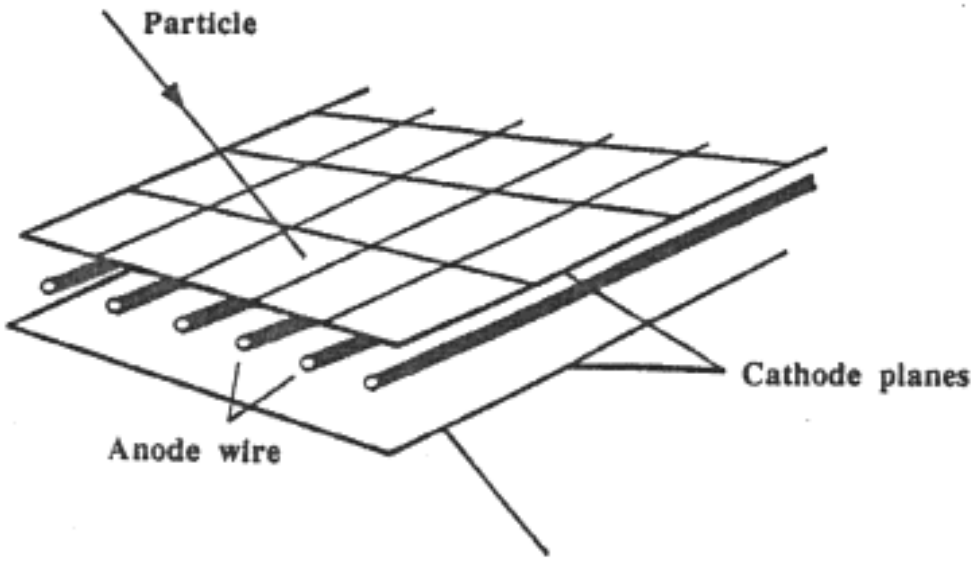

Figure 3.5 Schematic presentation of a MWPC (sample detector module) [69].

Charpak's' detector was used in HIDAC PET system.

In HIDAC PET system, each detector module consists of three layers; a converter, a MWPC and then further converter as shown in Figure3.6a [70].

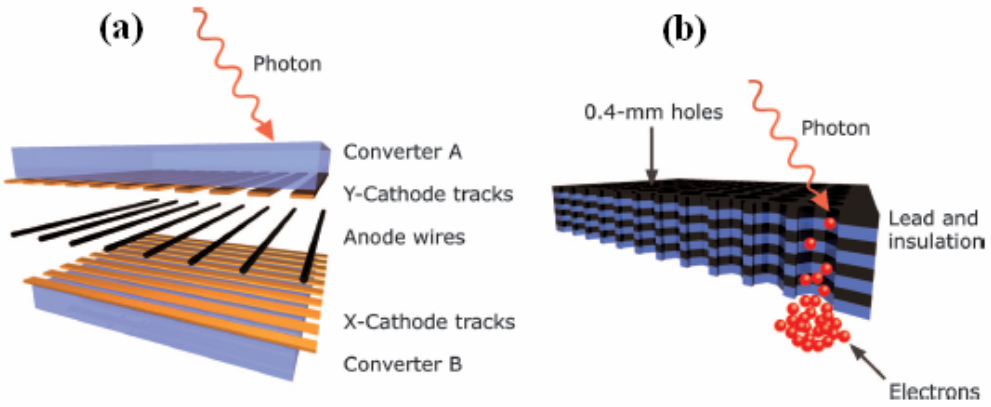

Figure 3.6 (a,b): (a) Construction of a detector module in 3 layers, (b) Construction of the converter [70].

Each converter contains interleaved lead and insulation sheets, mechanically drilled with a dense matrix of small holes. A photon interact with the lead, resulting in an electron that avalanches in a strong electrical field and accelerate toward the MWPC as depicted in Figure3.6b.

The main disadvantage of MWPC that it has no electronic energy discrimination of the incoming photons [70].

IV. SiPM (Silicon photomultiplier):

In the middle of 1985, in the research laboratory of Moscow Radio Devices Enterprise Prof. Yu. Yusipov began to work on stationary multiplication of photocurrent in metal conducting dielectric-semiconductor structures. In 1989, the MRS (metal-resistor-semiconductor) photodetector was developed based on this special structure [71].

First tests for physical application of Si-SSPM (Silicon Semiconductor Structure Photomultiplier = SiPM) were made at the end of 1992 in CERN. This study was published by Valeri Saveliev [71].

A novel type of avalanche photodetector (Silicon photomultiplier = SiPM) can operate in the Geiger Mode ,which means the bias voltage is above the junction breakdown voltage and any electron (photoelectron or thermal electron) in the depletion region will produce a large current flow (avalanche process) [72].

Construction form, working principle and size of SiPM are shown in Figure 3.7.

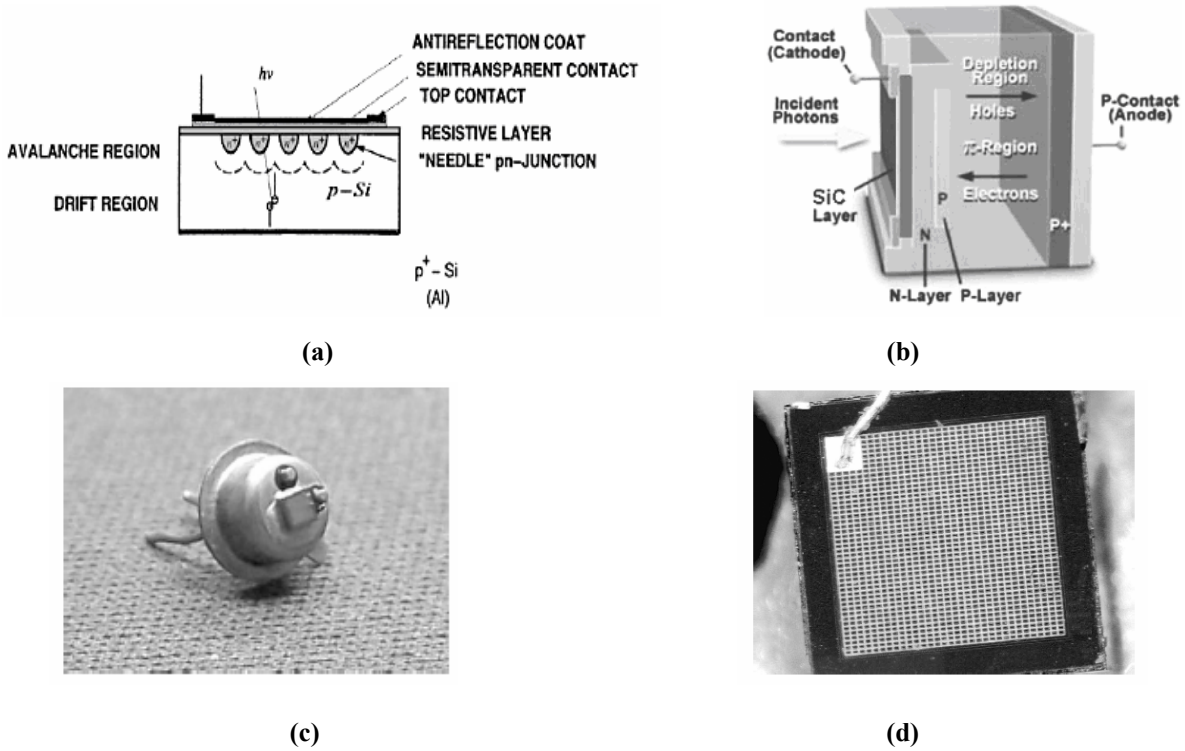

Figure 3.7 (a) Schematic structure of MRS Photodiode. **(b)** Schematic view of the SiPM microcell. **(c)** SiPM test device from CPTA, Moscow. **(d)** Close-up of the SiPM surface; 1440 microcells covering a 1x1mmsurface [72,73,74].

SiPM consists of ~10^3 micropixels, size ~30microns, with very thin (0.75 micron) high field depletion layer. [71, 72, 73, 74]

The gain is applied to the each microcell, i.e. 10^6 is the gain of single microcell. Each microcell can detect only one photon, with gain 10^6, then output of SiPM is sum of microcells signals (each of them produced by single photons in different microcells) that means it is very important the uniformity of gain overall the microcells, to reach the single photon response [71,72,75].

The main advantages of SiPMs are the high internal gain (~10^6) very fast time response (discharge time is typically about 500 ps and rise time is ~1 ns), low operation voltage (50V), insensitivity to the magnetic fields (make it compatible with Magnetic Resonance Instruments , MRI) , excellent single photoelectron resolution, its compactness, improved detection efficiency for blue light , simplest electronics ,relatively low cost mass production potential (low resistivity Si, simple technology) [71,72,75].

As regards their disadvantages: high dark count rate (2-3 MHz at room temperature for single counts), limited dynamic range (i.e. the maximal number of photons that can be simultaneously detected) $10^3/mm^2$, small size (1mm x 1mm, but larger dimensions could be produced), limited geometrical efficiency [71, 72, 75].

3.4 Counting Assembly (Signal processing components block)

There is no direct relation between counting assembly and the topic of this study.

3.5 Coincidence Detection System

3.5.1 The Simplest Coincidence Detection Unit

To detect two 511keV rays of pair production with ideal conditions, two gamma-ray detection units placing opposite direction of each other. The important point in this situation is that each detection unit crystal face must see the other detection unit crystal face perpendicularly (Figure 3.8). This combination is called coincidence detection unit.

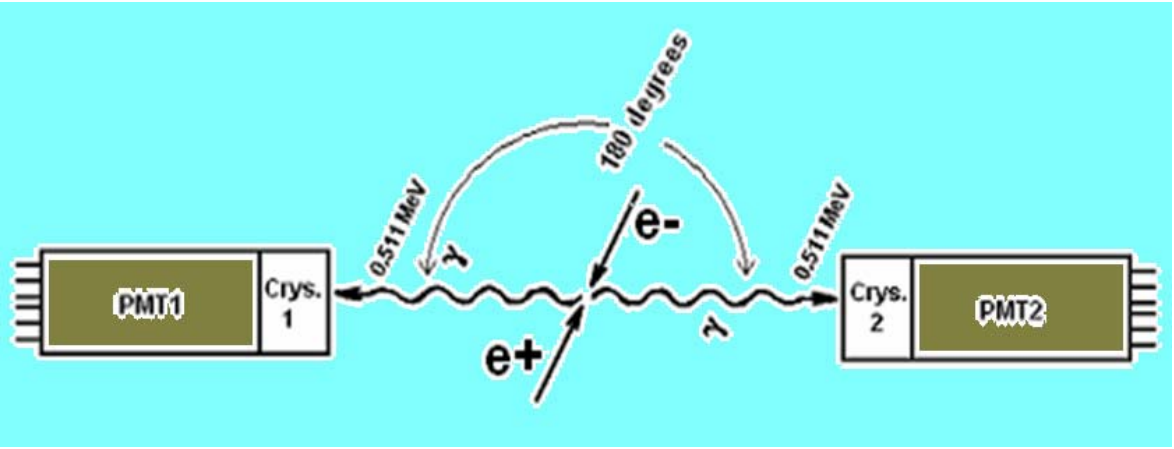

Figure 3.8 The Simplest Coincidence Detection Unit System.

3.5.2 Increasing the Detectibility Power of Coincidence Detection Systems

To obtain the highest detection chance of annihilation radiations and increase sensitivity, more than one pair of coincidence system should be used. The sample multiplication of coincidence detection system is seen in Figure 3.9.

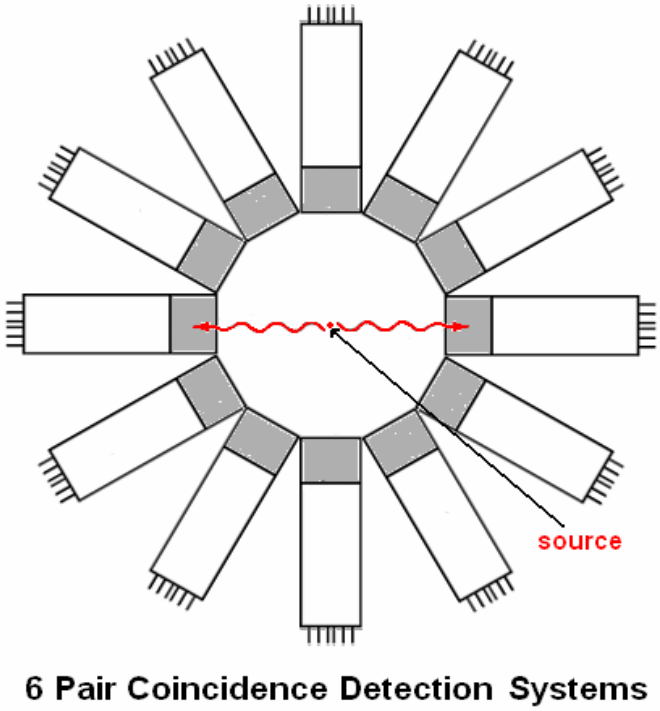

Figure 3.9 An example usage of more than one simple coincidence detection systems.

Available geometries for coincidence detector systems are shown very well by Christopher J. Thompson and reproduced from Phelps and Cherry [76].

Performance, geometric positioning and cost relation of coincidence detection systems is shown in below in Figure 3.10.

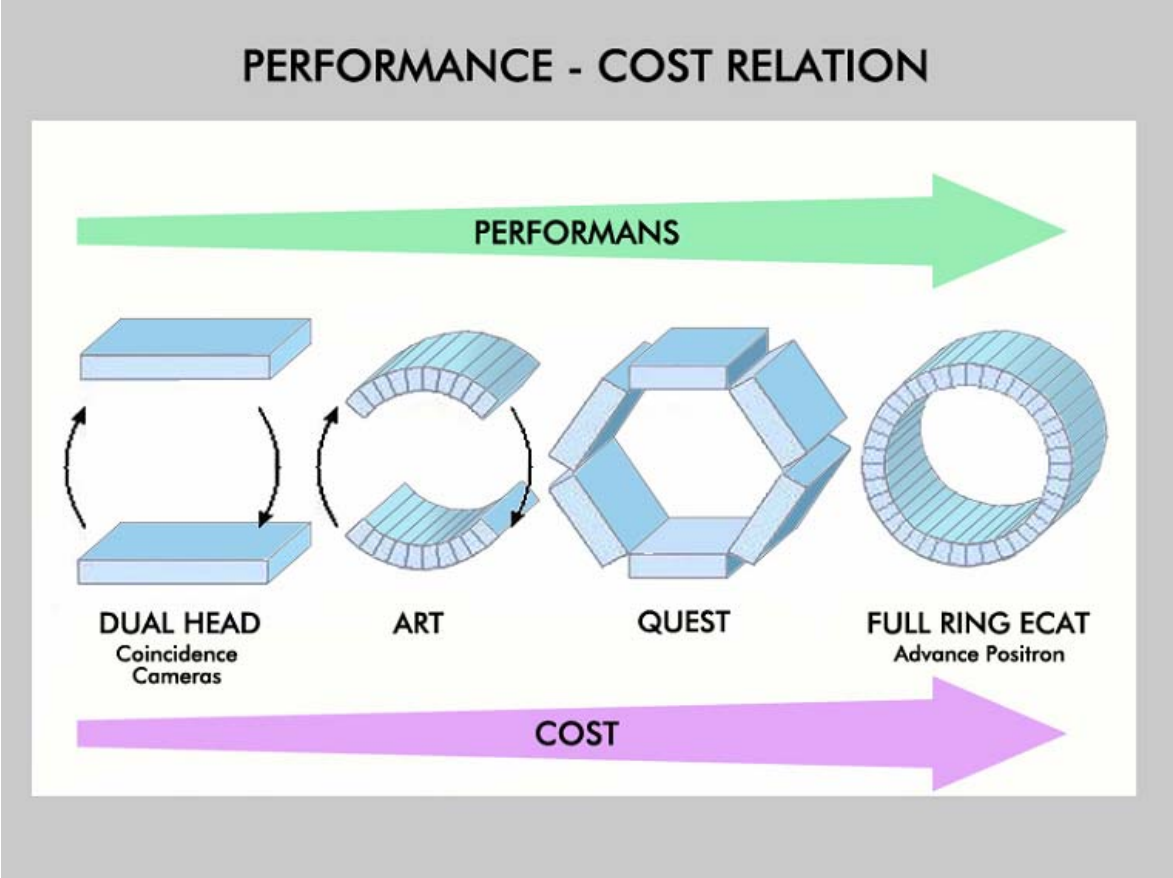

Figure 3.10 Performance and Cost Relation of pair of coincidence circuit systems (shown only detectors) [76].

3.6 Connections Materials between Crystals and Sensors (Light Guide)

Connection materials are:

- air,
- silicon oil,
- fiber optics,
- some plastics.

4. OVERVIEW OF PRESENT PET SYSTEMS DEDICATED TO ANIMALS AND THEIR TECHNOLOGICAL PROPERTIES

Under the light of this knowledge as mentioned above, different types of human PET systems have been produced. However none of them has sufficient power to obtain fully satisfactory images. On the other hand, for many years, different animal models have been used in biomedical research for the study of biological mechanisms and possible cures of human diseases, additionally, for the validation of gene therapies and new drug developments. For these purpose, each year increasing number of small animals were killed. Insomuch that, for research studies, world wide number of killed animals was arrived to 25 millions in the year 2000 [77, 78].

Till 1990, our scientific knowledge does not give permission to produce high resolution PET. For example, the PET systems having 4-5 mm resolution have been used for human body studies.

On the other hand, the average weight of human subject is ~70 kgs whereas rat weight is 300 grams.

While the average brain volume of mankind is 1300 cm^3, rat's brain volume is 1.75 cm^3 and mice brain volume is 0.5 cm^3.

As regards comparison of linear dimensions of human, rat and mice brain, they are 11cm 1.2 cm and is 0.8cm respectively.

After comparison of these, it is easily understood that a standard human PET system (having a 5mm resolution) can not be sufficient to obtain a good image from the small animals such as rat and mice.

Researchers, after 1990, benefiting from technological progression, have produced different types of dedicated small animal PET systems. Some of them have less than 0.7 mm resolution [79].

4.1 Crystal-based animal PET scanners:

4.1.1 MicroPET4:

MicroPET4 is developed at UCLA, California, USA and produced by Concorde Microsystems Inc. Detector type is LSO (Lutetium Oxyorthosilicate) coupled to position sensitive photomultiplier tube via bundled fiber optics. Spatial resolution at center is 1.8 mm [77, 80, 81].

Figure 4.1: Picture of the microPET P4 scanner. (Photograph courtesy of Concorde Microsystems, Knoxville TN) [77].

4.1.2 MADPET:

MADPET shown in Figure 4.2 (a,b) is developed at the University of Munich, Germany. Its construction uses LSO crystal coupled to an APD (avalanche photodiode). Spatial resolution at center is 2.2 mm [77, 80, 82].

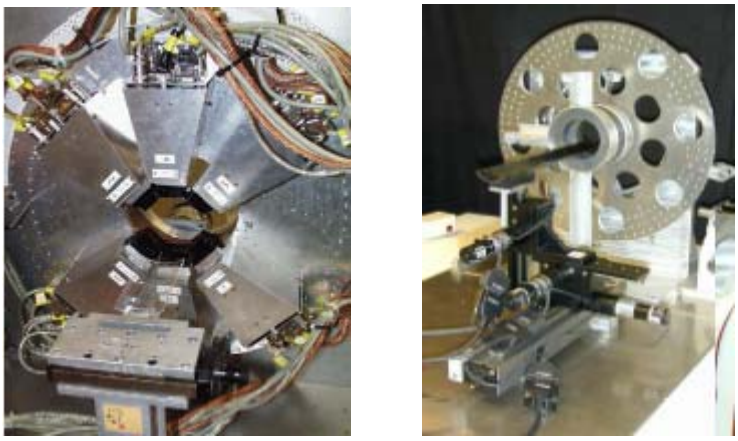

Figure 4.2: MADPETs **(a)** Picture of MADPET. **(b)** Picture of MADPETII [82].

4.1.3 TierPET:

The TierPET shown in Figure 4.3 has been developed at the Central Electronics Laboratory, Research Center Jülich. Its construction uses YAP:Ce (yttrium aluminate perovskite, cerium activated) crystals coupled to position sensitive photomultiplier tubes. Its spatial resolution is 2mm [80, 83].

Figure 4.3: The picture of the TierPET [83].

4.1.4 Hammersmith ratPET:

This tomograph shown in Fig. 4.4 has been developed at the Hammersmith Hospital, London, UK within the Cyclotron Unit. Its construction uses BGO (bismuth germanate) detector blocks and spatial resolution at the center of FOV is 2.3 mm [78, 80].

Figure 4.4: The ratPET prototype at the Hammersmith Hospital, London [78].

4.1.5 Sherbrooke APD-PET:

Sherbrooke (research prototype) shown in Fig. 4.5, is developed at the University of Sherbrooke (Canada), uses small BGO crystals (512 pieces). The crystals are read by avalanche photodiodes (APD) individually. The spatial resolution at center of field of view is 2.1 mm. Detailed information about Sherbrooke animal PET was stated in references 78,80,84.

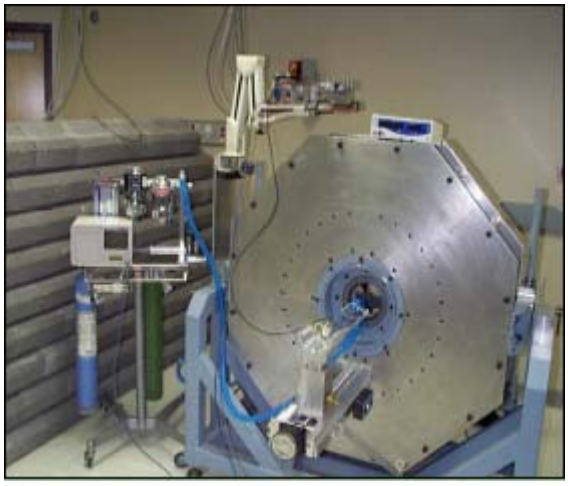

Figure 4.5: Sherbrooke Animal PET Scanner [84].

4.1.6 YAP-PET:

The YAP-PET shown in Figure 4.6 (a, b) (I.S.E. Srl, Migliarino Pisano, Pisa, Italy) is developed at the Universities of Ferrara and Pisa [85, 86]. It has four-head scanner geometry and each one consists of YAP crystals (2x2x30 mm^3) that optically isolated and glued together and coupled to position sensitive photomultiplier tubes. The FWHM at the center is 1.8 mm [78, 79].

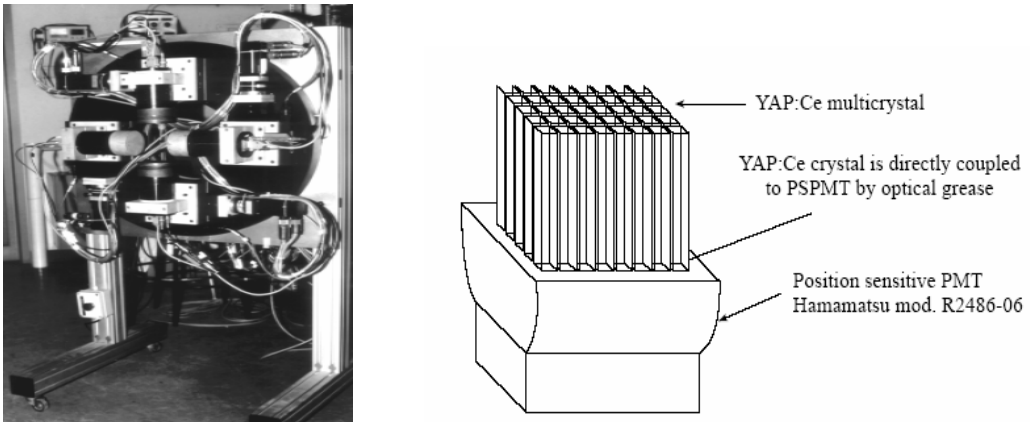

Figure 4.6 (a) YAP-PET scanner. **(b)** Construction scheme of each module [78].

4.1.7 SHR-7700:

SHR-7700 is one of the first animal PET scanner developed by Hamamatsu, JAPAN. Its construction uses BGO crystals and the reconstructed transaxial spatial resolution at the center of field of view is 2.6 mm [77]. (Figure 4.7, 4.8 below)

Figure 4.7: A high-resolution type animal PET scanner. (SHR 7700, 16 rings). In 1996, the 16 rings scanner the SHR 7700 (resolution 2.6 mm) was completed and commercialized [87].

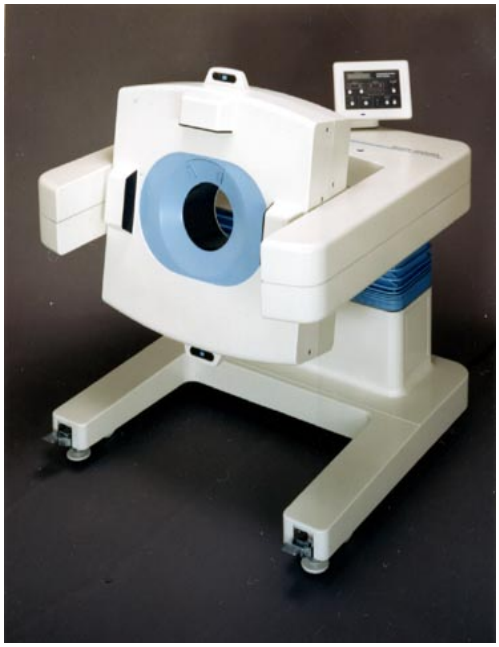

Figure 4.8: A compact type animal PET scanner. (SHR 2000, 4 rings). In 1990, the 4 rings animal PET scanner, the SHR 2000 (resolution 3 mm) using three inch position-sensitive PMT (PS-PMT) was developed [87].

4.1.8 ANIPET:

The ANIPET scanner is developed at McGill University, Dept. of Physics, Canada. It consists of two planar detectors operated in coincidence mode. Each detector consists of a 36 x 36 x 20 mm^3 pixelated BGO crystal coupled to a position sensitive photomultiplier tube .(PS-PMT Hamamatsu R3941-5) Spatial resolution is 2.8 mm (2D) , 3.2 mm (3D) (Figure 4.9 , 4.10) [88].

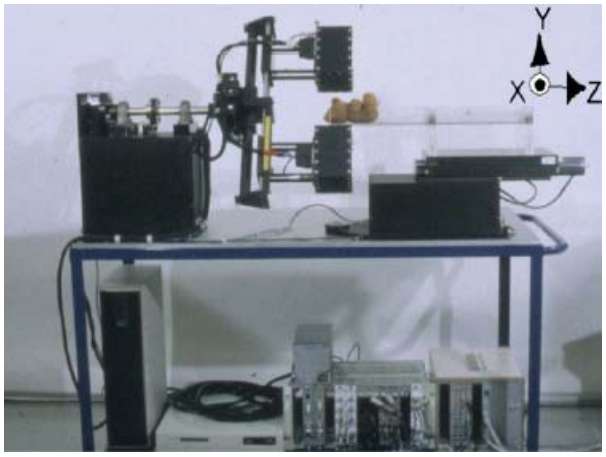

Figure 4.9: Side view in the Rotary scanning mode where the detectors are rotating around the Y axis. The entire system, including data acquisition electronics and computer, is contained on a mobile 0.8 x 1.5 m cart [88].

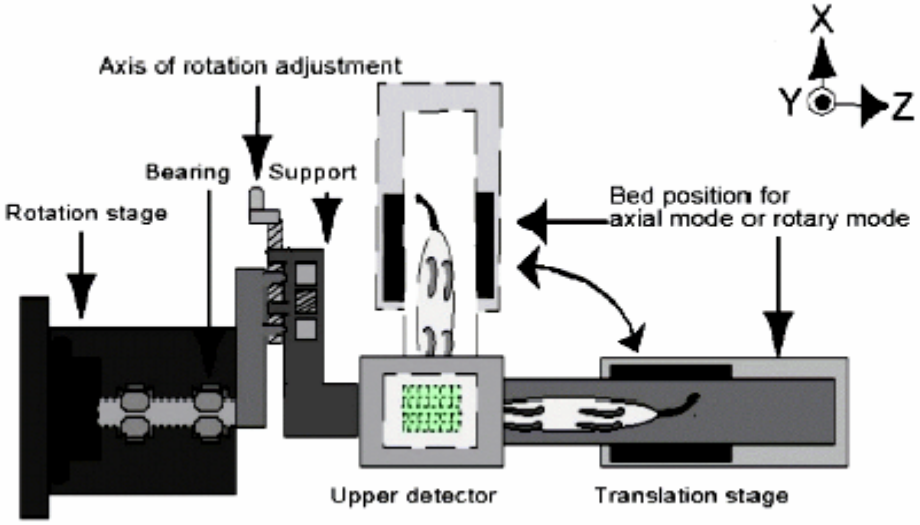

Figure 4.10: Schematics of the ANIPET Detectors and Translation Stage. Top view of the relative translation stage positions: the 3D-Rotary mode (solid); the 2D-axial mode (broken) [88].

4.1.9 ClearPET:

The Clear PET is developed at the CERN Crystal Clear Collaboration. Its detector configuration is composed of two different types of lutetium scintillators (LYSO/LuAP:Ce) of a high density. Reconstructed image resolution at CFOV is 1.5mm [89, 90]. (Figure 4.11)

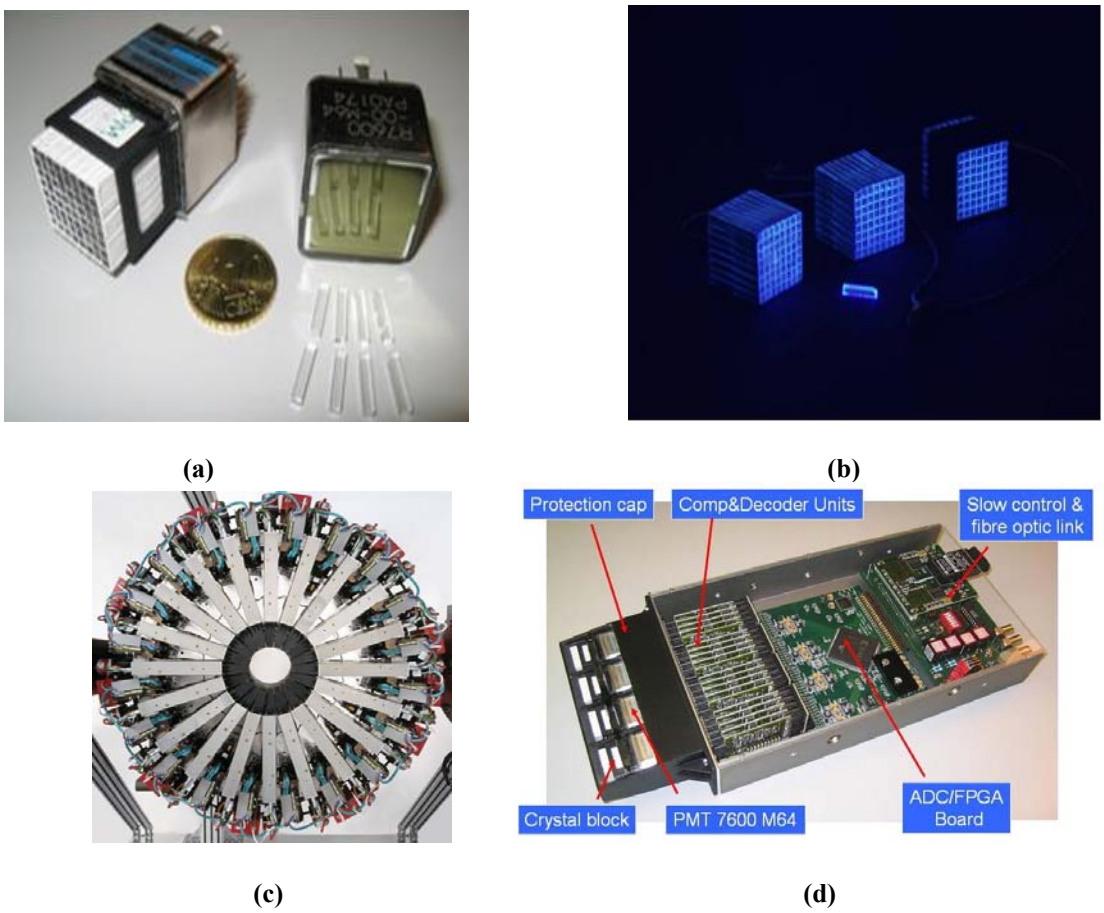

Figure 4.11 (a) Multi channel photomultiplier tube (7600M64, Hamamatsu), light shielding mask (Courtesy of Clear PET Collaboration). **(b)** Dual layer phoswich matrices (Courtesy of Clear PET Collaboration). **(c)** ClearPET Neuro Scanner. (Courtesy of Clear PET Collaboration) **(d)** PMT-detector cassette. (Courtesy of Clear PET Collaboration) [89, 90].

4.2 The Mosaic (Philips Medical Systems, Milpitas, CA, USA):

The Mosaic is developed by Philips in collaboration with the Department of Radiology at the University of Pennsylvania [91]. This scanner consists of 16680 discrete GSO crystals in a ring structure and uses 288 PMTs. The port diameter is 21cm and the crystal is 2.3mm.The spatial resolution at center of field of view (CFOV) is 2.2 mm [79] (Figure 4.12)

Figure 4.12: The Mosaic PET system. (Courtesy of Philips Medical Systems, Milpitas, CA, USA)

4.2.1 Explore Vista DR:

The Explore Vista (General Electric Healthcare, Waukesha, and WN, USA) is a scanner derived by the Atlas project of the National Institutes of Health in Bethesda [92]. The system consists of two rings of 6084 LGSO/GSO phoswich detectors coupled to PS-PMTs. The reconstructed image resolution at the center of field of view is 1.6mm [79, 93]. (Figure 4.13)

Figure 4.13: Explore Vista PET scanner (Courtesy of General Electric Healthcare, Waukesha, WN, USA).

4.2.2 RatCAP (Rat Conscious Animal PET):

A small, head-mounted tomograph is being developed which will allow PET imaging of the brain of an awake rat. This device will permit neurophysiological studies to be carried out on small animals without the use of anaesthesia, which severely suppresses brain functions and behaviour. The tomograph consists of a 4 cm diameter ring consisting of 12 blocks of LSO crystals, each containing a 4x8 matrix of 2x2 mm^2 pixels read out with a Hamamatsu S8550 avalanche photodiode array. The spatial resolution is 1.9 mm (for 5mm thick crystal), 2.5 mm (10mm thick crystal). For more details see Figure 4.14 (a,b,c) below [94, 95].

(a)

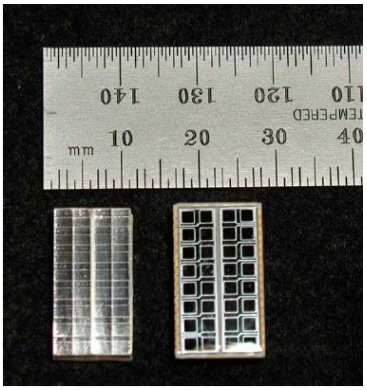

(b) **(c)**

Figure 4.14(a,b,c): (a) Mockup of the RatCAP ring on the head of a rat (left side) and Rat turn bowl used to support ring and allow freedom of movement (right side). **(b)** Proteus crystal array and Hamamatsu S8550 APD. **(c)**Block detectors form a ring connected with a flexible cable that serves as bus for transmitting serial data of the ring and receiving power and control signals [94,95].

4.2.3 IndyPET:

IndyPET is developed by the University of India**.** It composed of two detector banks mounted on a rotating gantry. (IndyPET) [96]. Its construction uses BGO crystal coupled to 4PMTs. The FOV is 18 cm transaxially and 5cm axially with a spatial resolution 2.8 mm in the center of field of view. Then, IndyPET was upgraded and IndyPETII was built. This scanner uses 120, CTI HR detector modules arranged in four detector banks. Each bank of 30 detectors is arranged in three axial rings giving a transaxial fov of 23 cm, and an axial fov of 15 cm. Shielding is provided by two lead plates with a clear aperture of 25 cm which are mounted immediately in front of, and behind, the detector banks. It is composed of 4 detector banks of which contains eight BGO (7x8 array) crystals for an increased sensitivity. IndyPETII has a 2.5 mm spatial resolution at center [97, 98] (Figure 4.15 (a,b,c))

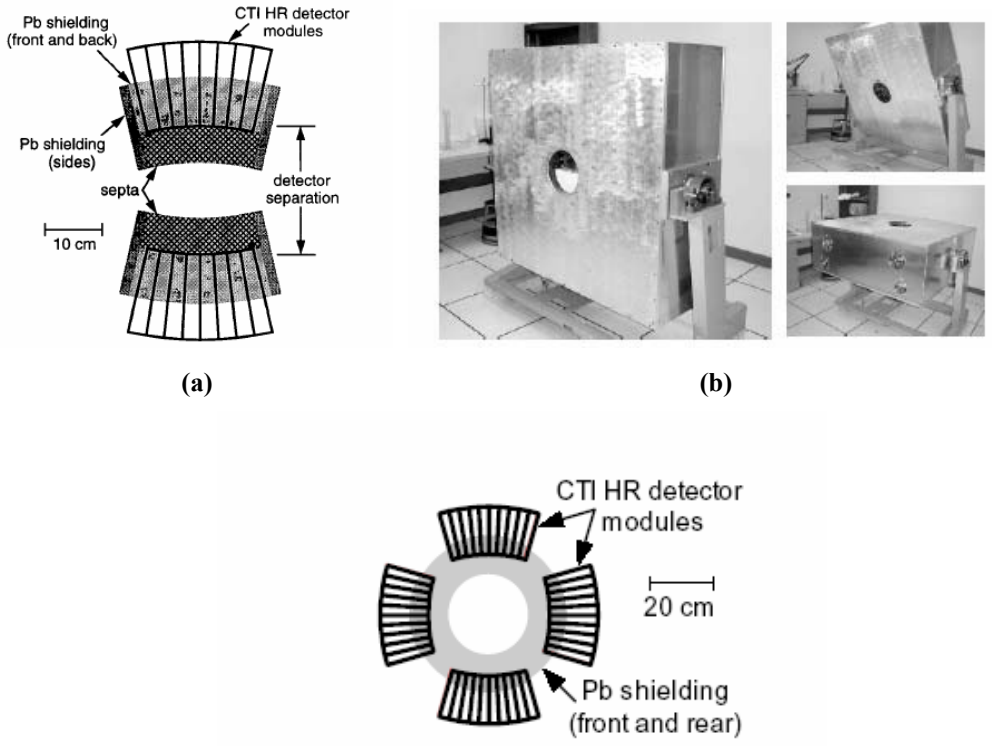

Figure 4.15 (a,b,c): (a) IndyPET detector configuration. (Two detector banks) Layout of the detector modules, septa, and Lead (Pb) shielding.**(b)** Photographs of the IndyPET-II scanner in normal, brain and breast imaging position **(c)** Diagram showing the detector bank layout and lead shielding on the IndyPET-II scanner [96,97].

4.3 Multi-wire chamber animal PET scanners:

4.3.1 QUAD-HIDAC 32:

The quad–HIDAC (Oxford Positron Systems Ltd., Weston–on-the-Green, Oxfordshire, UK) is the only commercial systems based on HIDAC. This large-area gas filled detector is able to measure the impact position of incident gamma-rays with a high spatial resolution [99,100].The scanner has four large area rectangular heads each of which consists of a stack of 8 HIDAC detectors with an active area of 17 cm x 28 cm. The distance between opposite heads is 17 cm. Due to its laminar structure; the detector system has depth-of-interaction capability. The reconstructed image resolution is 1mm [78, 79]. (See Figure 4.16 (a, b))

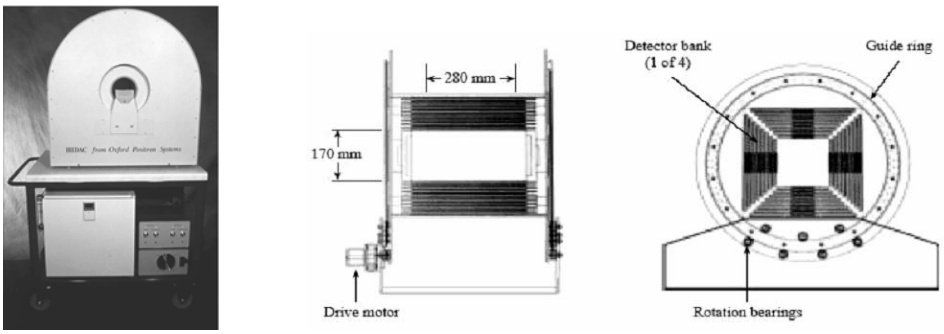

Figure 4.16 (a,b): (a) Picture of the HIDAC system, an animal PET scanner which uses multi-wire proportional chamber technology together with stacks of lead converters. These detectors have an intrinsic spatial resolution of < 1 mm.(Photograph courtesy of Oxford Positron Systems, Weston-on-the-Green, UK) **(b)** Schematic representation of the Quad-HIDAC, side view (left) and front view (right) [77,78,99].

4.3.2 TMAE PET:

The TMAE PET scanner was developed by Inter University Institute for High Energies, Bruxelles, is in use at Royal Marsden Hospital, London, for drugs research. This scanner uses BaF_2 (Barium Fluoride) crystals coupled to a photosensitive multi-wire gas chamber using a gas mixture, based on tetrakisdi-methyl-ammino-ethylene (TMAE) and helium, at a pressure of 8 mbar. The spatial resolution at the center of the FOV (FWHM) is 3 (transaxial) × 3.5 (axial) × 3 mm (tangential). BaF_2 has various components in its scintillation light spectrum; the fastest (λ=220 nm, τ=0.6 ns) with a light yield of about 1500 photons/MeV, is able to produce ionization of the TMAE vapor within the chamber

in the conversion zone where a strong electric field is established. The electrons produced in this way create a first avalanche in the drift region; then the electron cloud is transferred towards the anode wires, in proximity of which a second multiplication occurs. The charge induced on orthogonally orientated cathode wires allows X and Y position measurement of the point of interaction [78]. (Figure 4.17)

Figure 4.17: The TMAE-PET prototype based on TMAE vapour and Multi-Wire gas avalanche chamber [78].

All the published or produced systems can be collected in two tables: Table 4.1 and 4.2

Table 4.1: Overview of animal PET systems.

Name of Device	MicroPET (for rodent)	MicroPET (for primate)	MadPET	TierPET	Hammersmith RatPET	Sheerbrooke APD-PET	YAP-PET	Indy-PETII
Production Place	Ucla, Knoxville, TN,USA	Ucla Knoxville, TN,USA	Germany	Germany	London	Canada	Italy	USA
Producer	Concorde Micro-systems Inc.	Concorde Micro-systems Inc.	The University of Munich	Central Electronics Labs. Research Center	United Kingdom MRC Cyclotron Unit	The University of Sheerbroke	The Univ. of Ferrara	Indiana University
Scanner geometry	Ring	Ring	Ring	Ring	Ring	Ring	Four-head	Four , approx. plane detector banks
Scin. crystal	LSO (pixelated)	LSO (pixelated)	LSO (pixelated)	YAP(Ce) (pixelated)	BGO (block pixelated)	BGO (pixelated)	YAP(Ce) (Block pixelated)	BGO (pixelated)
Crystal size	2.1x2.1x10 mm^3	2.1x2.1x10 mm^3	3.7x3.7x12 mm^3	2x2x15 mm^3	30x6x3 mm^3	3x5x20 mm^3	2x2x30 mm^3	3. 3 x 6. 3 x 30 mm^3
Crystal array	8x8	8x8	8x2	20x20	8x7	16x16	20x20	7x8
Sensor type	Hamamatsu R5900-C8 PS via bundled fiber optics	Hamamatsu R5900-C8 PS via bundled fiber optics	APD array	PS-PMT	PMT	APD array	PS-PMT	PMT
Number of detector modules	24 modules	42 modules	6 modules	4 modules	16 detector blocks	8 modules	4 modules	4 modules
Axial FOV	7.8 cm	7.6 cm	6.4 cm	4.0 cm	5cm	1cm	4cm	15 cm
Transaxial FOV	10cm	10cm	Not informed	Not informed	Not informed	12cm	4cm	23 cm
Ring Diameter	14.8cm	26cm	8.6cm (MadPET) 7.1cm (MadPETII)	Variable between 16cm and 58 cm	11.5cm	31cm	_____	_____
Resolution at center	1.8mm	1.8mm	2.2mm	2mm	2.3mm	2.1mm	1.8mm	2..5mm
Volumetric spatial resolution at center	5.1mm^3	6.4mm^3	17mm^3	8mm^3	23mm^3	13.7mm^3	5.8mm^3	Not informed
Absolute sensitivity	24.5cps/ kBq	14.3cps/ kBq	0.35cps /kBq	16cps/kBq	43cps/kBq	5.4cps/kBq	17.3cps/ kBq	9030cps/ MBq

Table 4.2: Overview of animal PET systems.

Name of Device	SHR -7700	ANIPET	ClearPET	Quad-HIDAC (32) PET	PHILIPS Mosaic	GE Explore Vista DR	TMAE PET	RatCAP
Production Place	Japan	Canada	Switzerland	United Kingdom	U.S.A	U.S.A	Bruxelles	U.S.A
Producer	Hamamatsu	McGill University Depth. of Physics	CERN Crystal Clear Collaboration	Oxford Positron Systems Ltd , Oxford	Philips	GE	Inter University Institute for High Energies	Brookhaven National Laboratory, Physics Department
Scanner geometry	Ring	Dual-head	Ring	Four-head	Ring	Ring	Ring	Ring
Scintillation crystal	BGO (pixelated)	BGO (block pixelated)	LYSO / LuAP:Ce (pixelated)	_____	GSO (pixelated)	two rings of 6084 LGSO/GSO phoswich detectors (pixelated)	BaF_2	LSO:Ce (pixelated)
Crystal size	2.8x 6.95x 30 mm^3	(bi-layer array) 1.8x 1.8x 20 mm^3	2 x 2x 10 mm^3	_____	2 x 2x 10 mm^3	1.5x1.5x15 mm^3	3x3x20 mm^3	2x2x5 mm^3
Crystal array	8x4	20x20(?)	8x8	_____	278columns x 52rows	13x13	Not informed	4x8
Sensor type	Compact 28 mm square PS-PMT (Hamamatsu R5900-C8)	PS-PMT Hamamatsu 72 mm square R3941-5)	Multichannel PMT , Hamamatsu, 7600 M64	HIDAC (MWPC)	288 PMT's 19 mm (round)	36 PS-PMT	Positon sensitive Multi-wire gas chamber (TMAE)	S8550 APD array,Hamamatsu , photonics, Japan
Number of detector modules	4 detector rings (each of which consists of 60 detectors)	(two planar detectors)	80 modules in four rings	8 modules	50 modules	18 modules	6 angular sectors	12 detector blocks
Axial FOV	11.4 cm	25.6cm (2D) 5.4cm (3D)	11 mm	17 cm	11.6 cm	4.6 cm	Not informed	2 cm
Transaxial FOV	33 cm (wide aperture)	5.4cm(2D) 5.9cm-8.4cm(3D)	12.5 cm or 24.5 cm (animal port)	28 cm	12.8 cm	6 cm	Not informed	Not informed
Ring Diameter	50.8 cm	_____	14 cm or 26 cm	_____	21 cm (port diameter)	11.8 cm	20 cm	4 cm
Resolution at center	2.6 mm	2. 8mm (2D) 3. 2 (3D)	1.5 mm	1 mm	2. 26 mm	1.6 mm	3 mm	1. 28 mm
Volumetric spatial resolution at center	22 mm^3	35.8 mm^3	3.4 mm^3	1.09 mm^3	Not informed	4 mm^3	Not informed	Not informed
Absolute sensitivity	23 cps/kBq	8 cps/kBq	17 cps/kBq	18 cps/kBq	5.7 cps/kBq	4% for a 250-750 keV energy window	32 cps/kBq	150cps/µCi

5. MATERIAL AND METHOD

5.1 Overview of Material and Methods

In this chapter, information is given on how to design a PET detector benefiting from theoretical knowledge by the help of DETECT2000 Monte Carlo simulation package for small animal brain imaging describing by high spatial resolution, high sensitivity and good energy resolution.

5.2 The Main Objective of the Work

The aim of this work is to develop a more satisfactory and low cost dedicated PET detector module for small animal brain imaging by using a conventional continuous Lutetium Oxyorthosilicate (LSO) crystal coupled to a position sensitive photomultiplier tube (PS-PMT).

On the other hand, it is expected that the main characteristics of continuous crystal detector (especially energy and spatial resolution) to be strongly related to the crystal thickness and surface treatment. Thus, the power of these relations on the contemplated detector design has been investigated by using DETECT2000 simulation package.

5.3 Requirements of the Study

This simulation study has required a high capacity PC (see Appendix C) suitable for Red Hat Fedora Core3 Linux Operation system, DETECT2000 simulation package, (see Appendix D), Matlab (The Language of Technical Computing) and Gnuplot (A Portable Command-Line Driven Interactive Data and Function Plotting Utility for UNIX Version), graphic programs. A selected suitable continuous scintillation crystal LSO (Lutetium Oxyorthosilicate) and a sensor (position sensitive photomultiplier tube).

5.3.1 Reasons for Preferring a Continuous Crystal

There are two main factors for this selection;

- Discrete designs are expensive and labour-intensive (requires a lot of work and manpower to obtain accurate and consistent crystal size),
- Detector concepts based on discrete designs lead to low packing fraction due to dead spaces between small crystal elements which lead to reduction in the light collection efficiency and also cause inter crystal scatter.

5.3.2 Reasons for Preferring a PS-PMT Instead of a Solid State Sensor

Advantages of position sensitive photomultiplier tubes:

- High sensitivity
- Good energy resolution
- Excellent time resolution
- Low cross-talk between multi anodes
- Low cost [101]

While PS-PMTs have these advantages mentioned above, solid state detectors have many disadvantages as indicated below.

- Smaller signals, mainly because of the much smaller surface area of the light sensitive region ,
- Higher noise, chiefly counting noise ,
- Poorer signal to background ratios, particular for short acquisition time,
- Occasionally worse detection limits, but not necessarily ,
- Poorer spectral resolution - mathematical corrections required ,
- Resolution changes with wavelength in some designs ,
- Blooming at high intensities occurs in nearby pixels ,
- Slower response time ,
- Speed usually limited by the need to integrate to overcome counting noise ,
- Smaller dynamic range of intensities [102].

5.3.3 Selected Sensor for This Study:

In this study, The PS-PMT Hamamatsu H8711-03 has been selected. The cardinal reasons for choosing this PS-PMT are:

- Effective area of photocathode is very suitable for large (front) face of our scintillation crystal, because the area of our continuous crystal is 16×16 mm^2 ,
- Photocathode spectral sensitivity is suitable for the light emission spectrum of our scintillation crystal,

Necessary part of key specifications of this tube are informed below table (Table5.1)

Table 5.1: Specification table of H8711-03 [103].

Head on / Side on	HeadOn
Size	30x30mm
Effective Area	18.1 mm x 18.1mm
Peak Wavelength	420nm
Window Material	UV Glass
Min Wavelength	185nm
Max Wavelength	650nm
Multi Anode	Yes
Number of Elements (X)	4
Number of Elements (Y)	4
Type(Pixelated or PSD)	Pixelated

H8711-03 PS-PMT tube contains 16 (4x4) independent anode pads, characterized by a net area of 4.2×4.2 mm^2 each. (see Figure 5.1) [103].

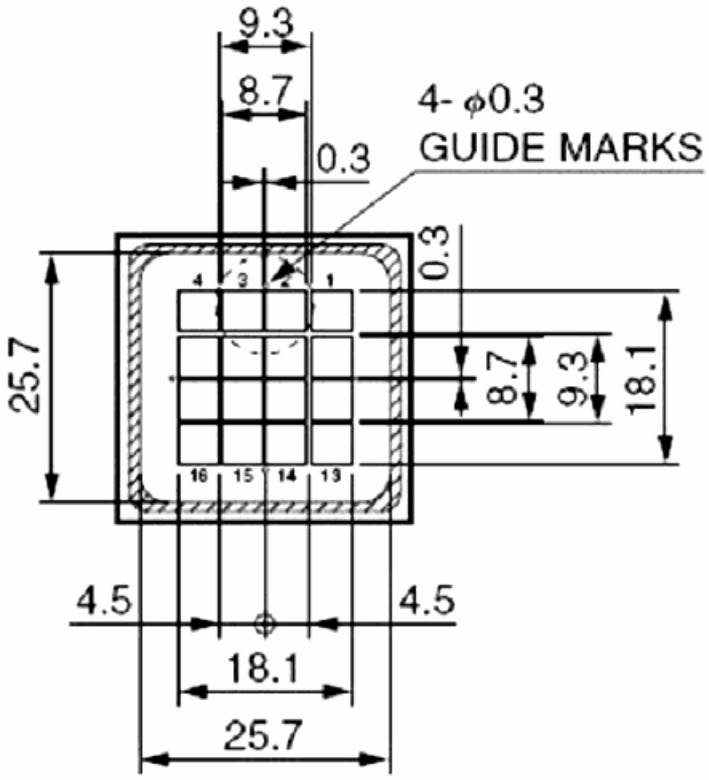

Figure 5.1: H8711-03 PS-PMT [103].

5.3.4 Definition of the Anode Pads in Simulation:

In order to simulate these 16 anode pads mentioned above, 16 independent square photocathodes were defined in the prepared simulation macro.

5.3.5 Selected Scintillation Crystal:

The selected scintillation crystal is LSO, because it offers the best combination of properties for PET of any scintillator known today. It has:

- high density,
- high atomic number,
- short decay constant (good for coincidence timing),
- high light output (allows the use of many small elements per PMT),
- it is mechanically rugged,
- it is non-hygroscopic,
- its fabrication is relatively simple [63].

(For more details see Appendix B)

5.4 Description of Scintillation Crystal Surface Treatments Used in Simulations

5.4.1 Physical Properties and Geometry of Used Scintillation Crystal for Simulation

During the simulations, 16×16 mm^2 LSO crystal with three different thicknesses (3mm, 6mm, 9mm) was used in order to study the properties of the detector according to four different crystal's surface treatments. The following different grades of polishing and painting are considered in this work: POLISHED + Black (PB), GROUND + Black (GB), GROUND + Methacrylate (GM) and GROUND + Air (GA).

a. **POLISHED + Black (PB):** In this configuration, gamma rays entrance surface (F.F) and the surface in contact with the PS-PMT (B.F) are considered polished in the simulation, while the sides are assumed to be ground. It is considered that the black epoxy which covers the crystal is not ideal and therefore, it absorbs only the 95% of the light. As a consequence, a reflection factor of 0.05 is simulated for all surfaces except the one that is in contact with the PS-PMT, which is not painted black (Figure 5.2).

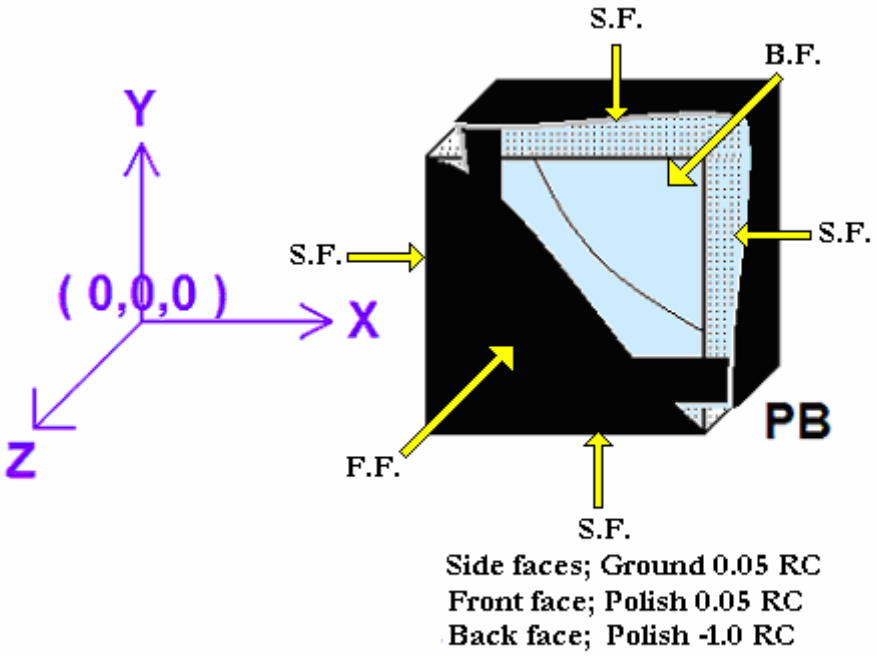

Figure 5.2: Polished + Black surface treatment of the scintillation crystal.

b. GROUND + Black (GB): In this configuration, all the surfaces were simulated to be ground. This model simulates a roughened optical surface. All surfaces except the one that is in contact with the PS-PMT absorbed 95% of the light arriving to them. (Figure 5.3)

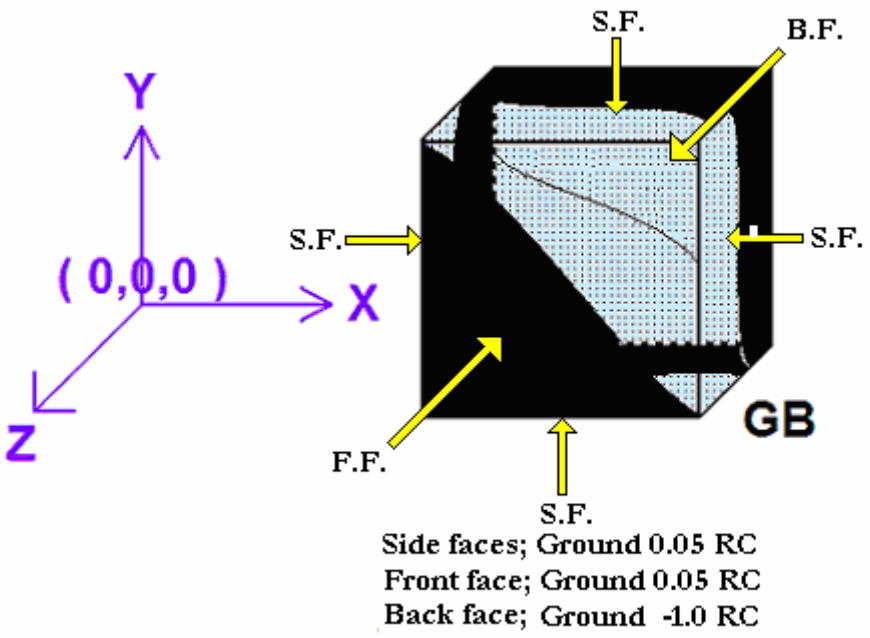

Figure 5.3: Ground + Black surface treatment of the scintillation crystal.

c. GROUND + Methacrylate (GM): In this configuration, it was simulated all the surfaces to be ground. Only the entrance surface has a light absorption of 95%. The crystal sides are in contact with boxes of -x +x sides are 2 x 20 x (3-6-9) mm^3 and -y +y sides 16 x 2 x (3-6-9) mm^3 boxes with a refraction index of 1.44 in order to simulate the methacrylate. In this simulation, the RC (surface reflection coefficient) values of Z_{min}, Z_{max} for methacrylate boxes were taken 0.05 and 0.95 respectively. The function of the methacrylate boxes (4 boxes for side faces) is collecting the light via its refraction in the material. (Figure 5.4.)

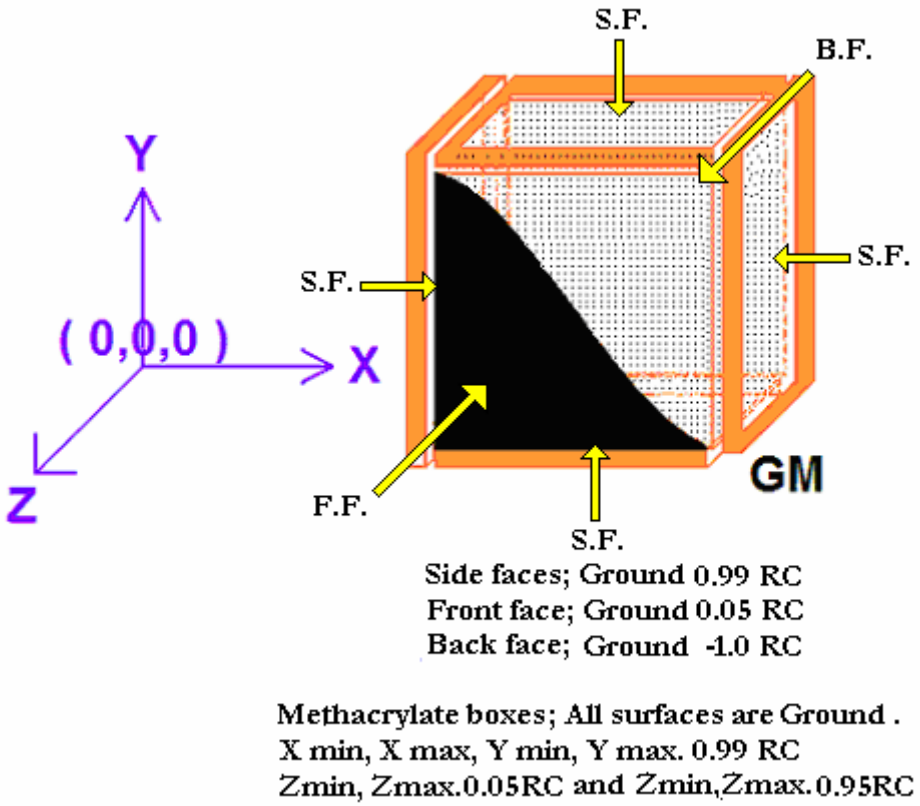

Figure 5.4: Ground + Methacrylate surface treatment of the scintillation crystal.

d. GROUND + Air (GA): For this configuration, all surfaces were simulated to be ground. Only the photon-incident surface has a light absorption of 95%. The crystal sides are in contact with boxes of -x +x sides are 2 x 20 x (3-6-9) mm^3 and -y +y sides 16 x 2 x (3-6-9) mm^3 of air with refraction index of 1.In this simulation, the RC (surface reflection coefficient) values of Z_{min}, Z_{max} for air boxes were taken 0.05 and 0.95 respectively. Four air boxes were selected for side faces to allow a larger collection of the light than with methacrylate. (Figure 5.5) [104].

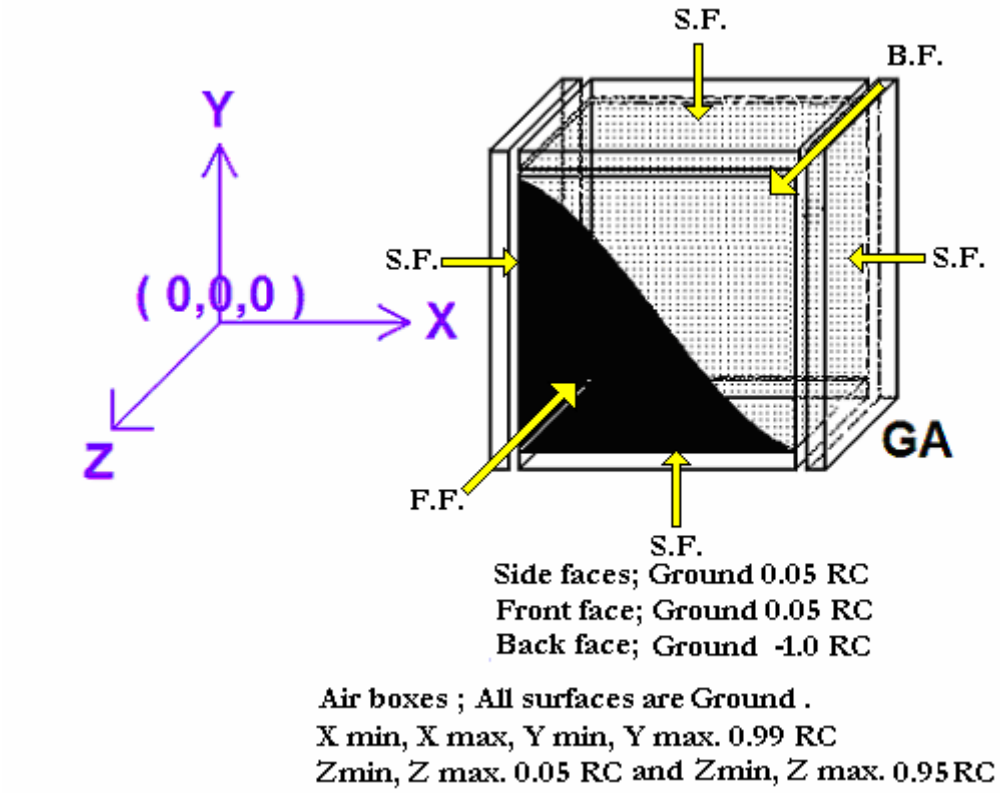

Figure 5.5: Ground + Air surface treatment of the scintillation crystal.

5.4.2 Connecting Material Between Scintillation Crystal and PS-PMT

Connecting material (light guide) is necessary to obtain best contact (parallel plane and homogen) between PS-PMT and scintillation crystal.

In this study, for this purpose, the optical grease (refraction index of 1.55) was used between back face of crystal and PS-PMT glass window. See Figure 5.6 including RC values too [104].

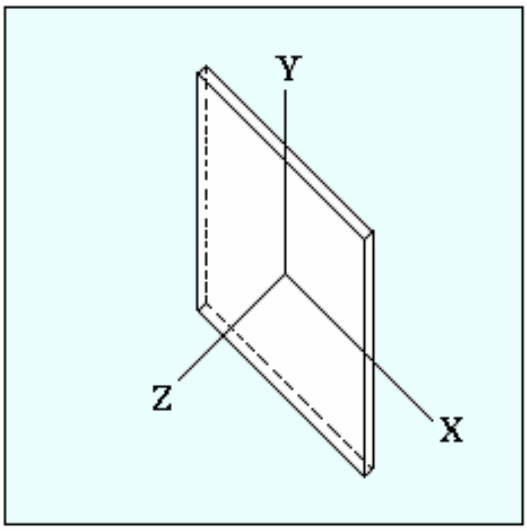

RC's of OPTICAL GREASE

For PB:

X min, X max, Y min, Y max. : Metal 1.0 RC

Z min, Z max. : Polish -1 RC

For GB:

X min, X max, Y min, Y max. : Metal 1.0 RC

Z min, Z max. : Ground -1 RC

For GM:

X min, X max, Y min, Y max. : Ground 0.99 RC

Z min, Z max. : Ground -1 RC

For GA:

X min, X max, Y min, Y max. : Ground 0.99 RC

Z min, Z max. : Ground -1 RC

Figure 5.6: RC values of optical grease.

5.5 Simulation Setup

Schematic view of detector components and simulation setup are seen in Figure 5.7 and 5.8 with full details except source coordinates.

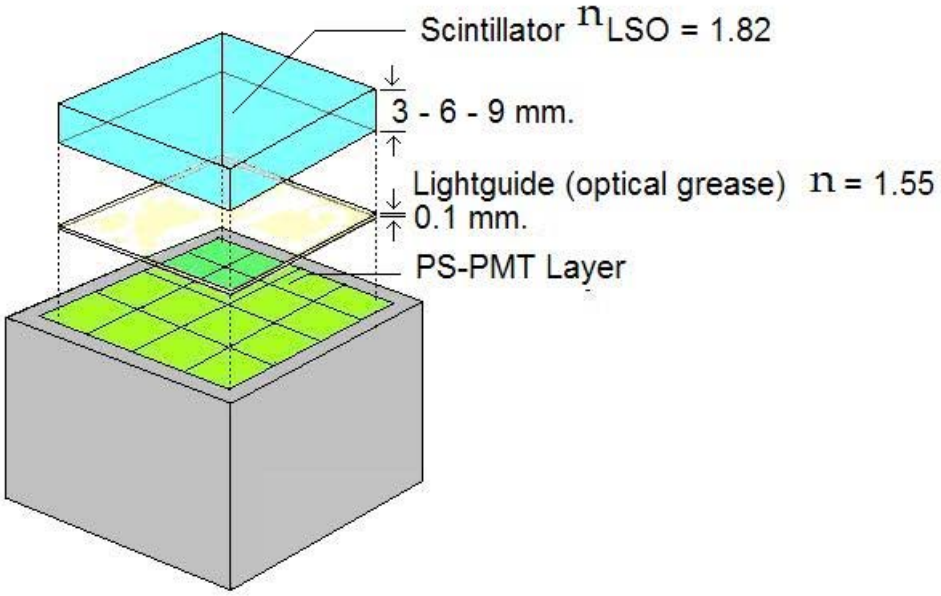

Figure5.7: The schematic diagram of detector components.

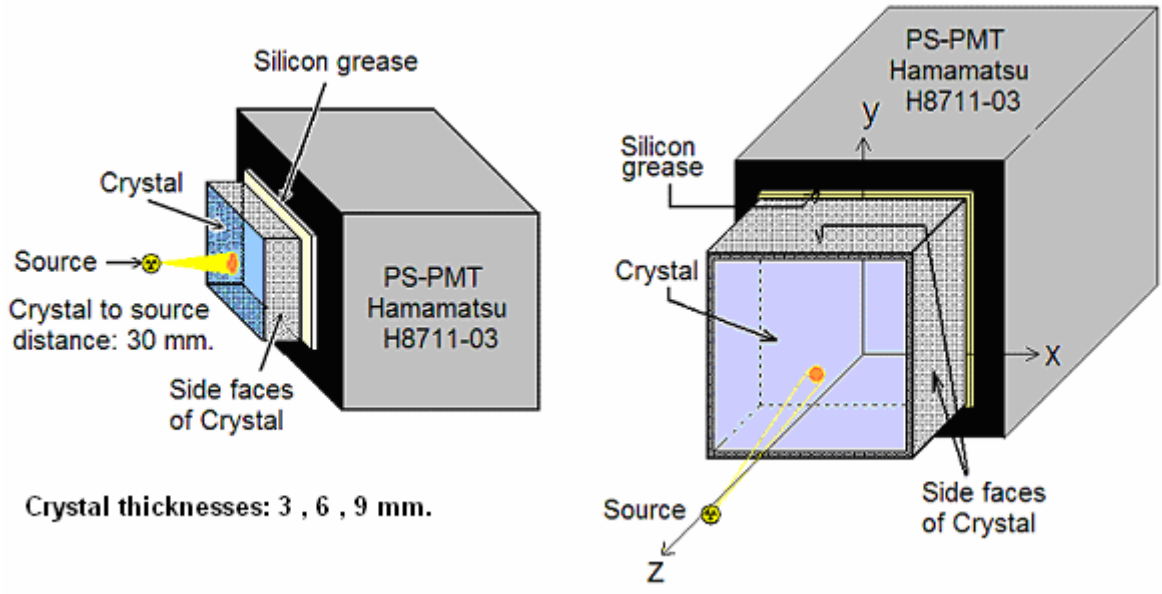

Figure 5.8: Schematic view of simulation setup.

5.5.1 Source Locations:

In the simulation experiment, the distance of source from the front face of the crystal is 30 mm along the Z coordinate. (This distance is fixed during all the simulations).

This source is placed by using two different logics:

1. According to the first logic, the point source was moved to 16 different coordinates along the X-Y axis of the scintillation crystal. Each selected coordinate was exactly identical with the central coordinates of the each independent anode pads of the PS-PMT which means that the source and the central point of each PS-PMT's anode pad was face to face. (They were called central coordinates (cc).) (see Figure 5.7) These coordinates were selected to obtain uniform crystal behaviour. On the other hand, the center of anode pads of PS-PMTs has maximum light collection due to geometric reasons. (see Figure 5.9)

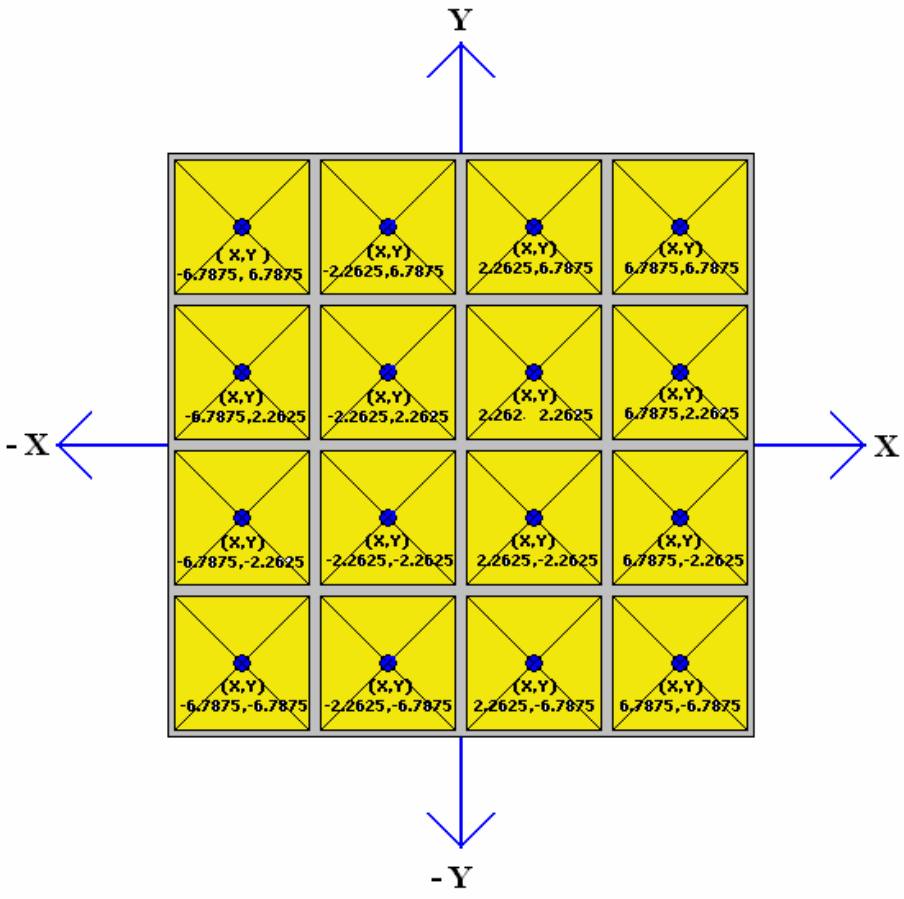

Figure 5.9: Central source coordinates used in the simulations.

2. According to the second logic, the new coordinates were selected such that they are closer to each other, especially at the edge of the crystal to see the results of that region.

For this purpose, 25 different points were chosen away from the anode pad centers of PS-PMT and these points were called as out of center coordinates (oc). (see Figure 5.10)

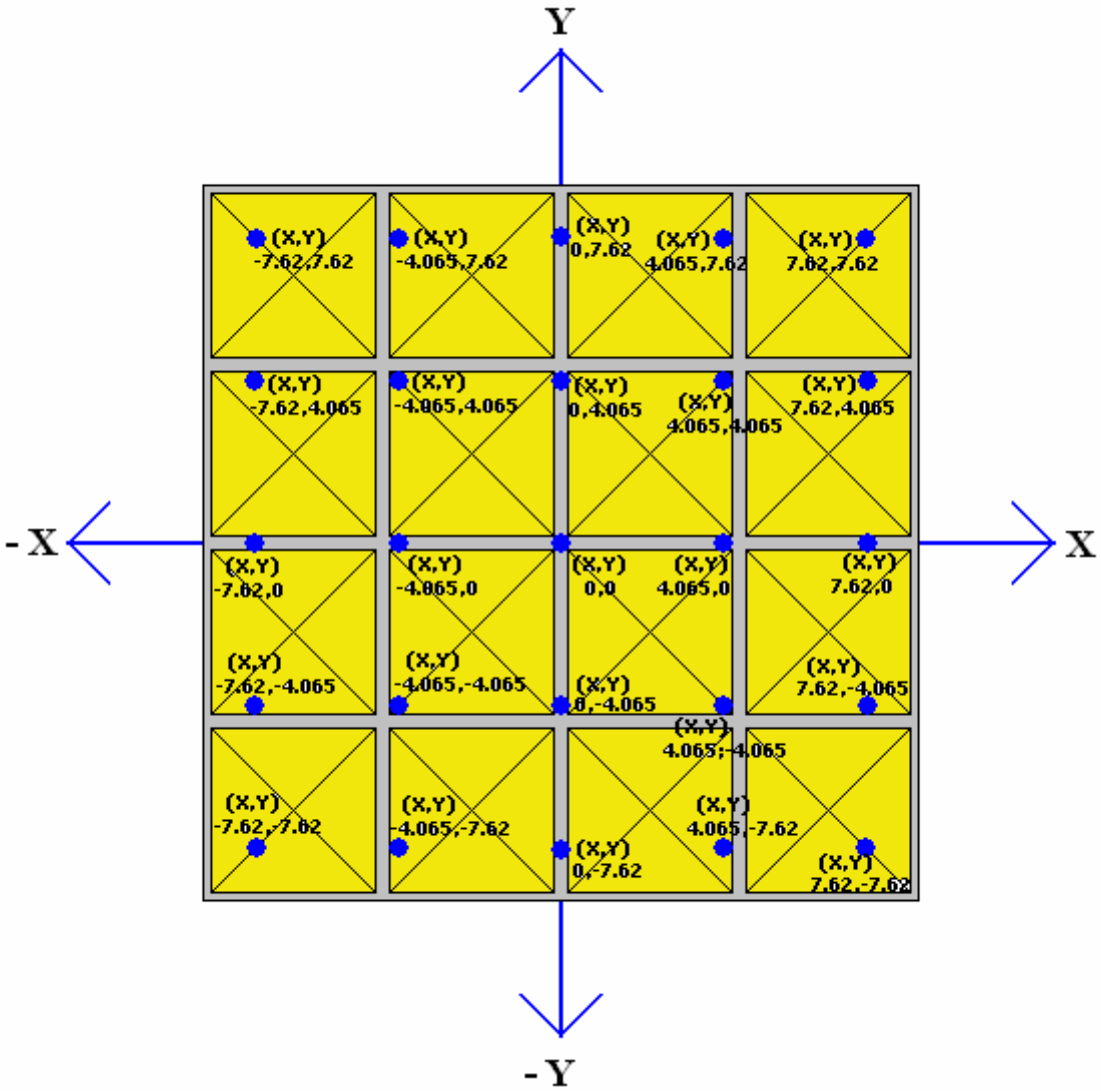

Figure 5.10: Out of centers source coordinates used in the simulations.

5.5.2 Angle of Incident 511 keV Gamma Rays to the Front Face of Crystal

Schematic presentation of the incident gamma rays angle is shown in Figure 5.11 [108].

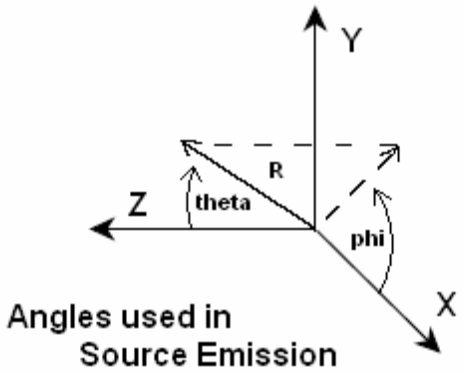

Figure 5.11: Angles used in Source Emission.

In the simulations, the used angles for source emission are informed below;

Theta-low = 3.141592654
Theta-high = 3.141592654
Phi-low = 0.0
Phi-high = 0.0

Thus, the narrow beams of 511 keV gamma rays impinging at the detector crystal surface in a given point and a given incidence angle have been simulated. During the simulations, the values of theta and phi angles were not changed.

5.5.3 Direction and Number of Incident Gamma Rays for Each Coordinate:

For each selected coordinate, 5000 gamma rays were simulated. All 511 keV gamma rays were sent along the –z direction and each simulated point flux was perpendicular to the front face of the crystal at multiple locations to determine the intrinsic spatial resolution. (see Figure 5.8)

5.6 The Used Simulation Program:

In this study, the DETECT2000 simulation package is used to simulate optical light production and transport to the PS-PMT photocathode. It is a Monte-Carlo simulation model (see Appendix E) of the light photon behaviour inside an optical device [105].

5.6.1 DETECT2000 Simulation Package and Its Functionalities

DETECT2000 simulation package was developed as a public domain platform by the TRIUMF PET detector group to simulate the position and energy responses of scintillation counters for hard X-ray and gamma-ray imaging. As seen Figure in 5.10 DETECT2000 simulation package is consists of three main parts in our simulation setup [106,107,108,109]:

- Builder (A High Level Language Interface to DETECT for the Design of Scintillation Detectors),
- GRIT (Gamma-Ray Interaction Tracking)
- DETECT2000 (The Object Oriented C++ Language Version of DETECT a Program for Modelling Optical Properties of Scintillators) (see Appendix F for sample input and output simulation file).

5.6.2 DETECT2000 Simulation Platform

The simulation platform treats the gamma ray interactions in an inorganic scintillator, the geometry of the crystal and also, the propagation and detection of individual scintillation photons. (see Figure 5.12)

The geometry of the crystal module is first used as input to the gamma ray transport module (GRIT). A uniform beam of gamma rays with specified energy is generated from a distant point source. Each incident photon is then followed in the volume of the crystal block for the photoelectric and Compton interactions. For each interaction, an event scintillation vector is written to a gamma ray interaction list file. The first three words in the list file are the coordinates of the interaction point within the crystal block (X_i, Y_i, Z_i). The fourth word gives the calibrated light yield, L_i, at that vertex. The fifth word is a sequential index incremented for each interaction until all the energy of the incoming

gamma is deposited in the block volume or until the gamma escapes from the scintillation crystal volume. Finally, the last two words give the entrance coordinate (X_γ ,Y_γ), of the incoming γ to the scintillation crystal block.

The DETECT syntax translator defines the geometry and optical properties of the block in adherence to the language syntax imposed by the light transport simulator DETECT [113]. When the translation is complete, the geometry and optical properties of the detector are included in the DETECT simulation driver to initialize the block design specifications.

Scintillation events from the gamma ray interaction list file are then simulated sequentially. The coordinates (X_i, Y_i, Z_i) of the interaction point are used to specify an infinitesimal voxel from which L_i scintillation photons are isotropically generated and followed by DETECT. The signal signals collected in detector are written in detect output file (event signal vector).

The event signal vector belongs to same incoming gamma ray are finally merged to compute total energy deposited in the detector and the coordinates of the interaction [57].

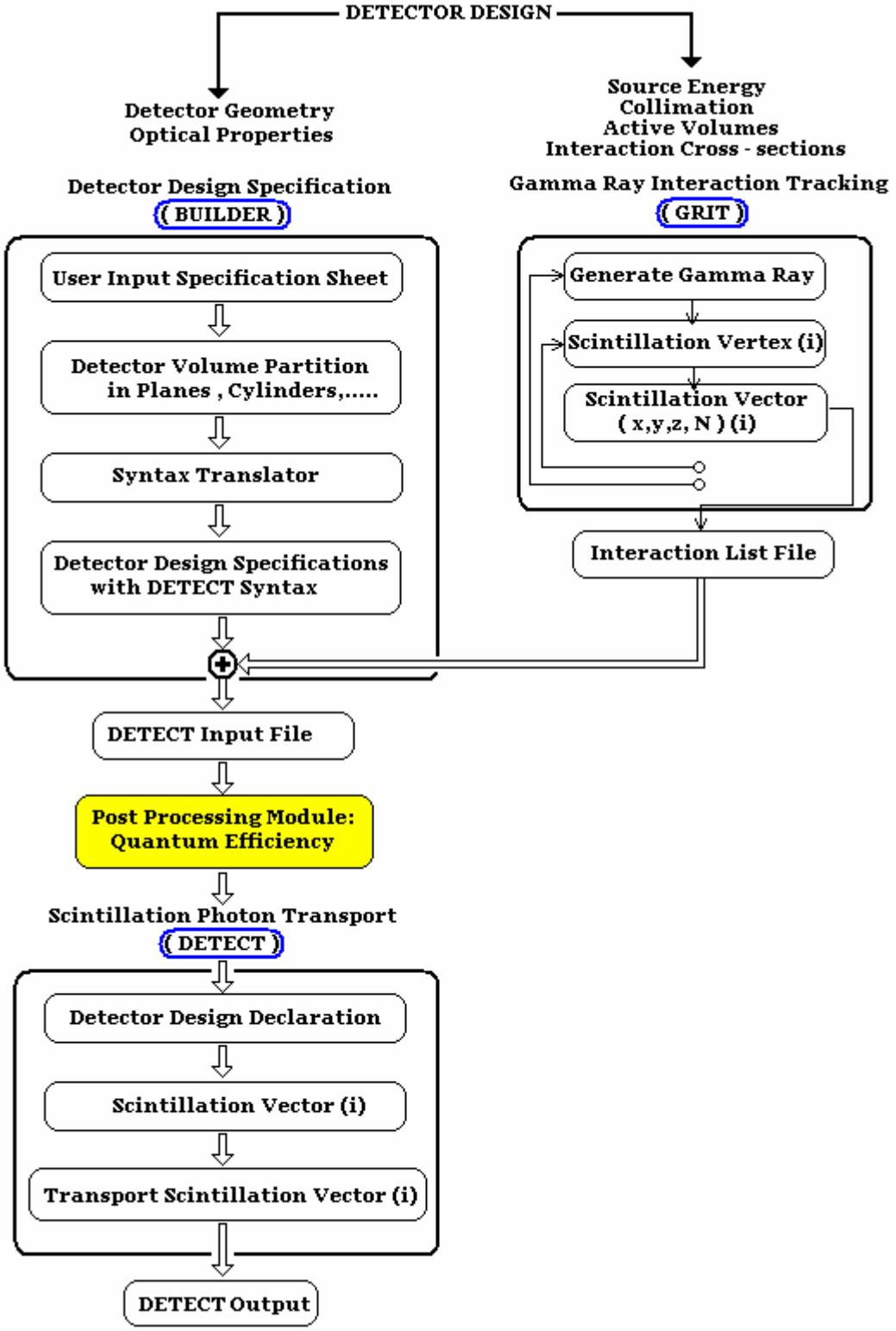

Figure 5.12: The main components of DETECT2000.

5.7 Surface Models in DETECT2000

DETECT2000 allows the user to choose among seven different surface finishes: METAL, PAINT, POLISH, GROUND, UNIFIED, DETECT and PSEUDO. A PSEUDO surface is a non-existent surface and is only employed for the purpose of connecting different components of similar material properties. The remaining five surfaces each treat the absorption and transmission of light at their boundaries differently [110,115].

i. Metal

In this model, the surface is assumed to be smooth and covered with a metallic coating. This surface allows no transmission. The user could specify a reflection coefficient, RC, for the surface. If a photon hits this surface, it is either absorbed in the surface with the probability (1-RC) or reflected back into the component by specular reflection. In the event of a specular reflection, the angles of incidence and reflection with respect to the global normal of the surface are the same [110].

ii. Paint

This model simulates a surface painted with a diffuse reflective material. As with the METAL model, no transmission is allowed and the user has the option of specifying an RC for the surface. If a photon hits this surface, depending on the RC, it is either absorbed in the surface or reflected back into the component by Lambertian reflection. Lambert's law states that the intensity of light scattered from a point on a reflecting surface follows a cosine relationship [110].

$$I(\theta_s) = I_0 \cos(\theta_s) \qquad (5.1)$$

where θ_s is the polar angle of the scattered light and I_0 is the incident light intensity at the point. Lambert's law approximates what is observed in reflection from rough surfaces where many randomizing events may occur before the light leaves the surface [110].

iii. Polish

This model simulates a perfectly polished surface that may or may not be in contact with another component. If no other component is specified, the surface is assumed to be

in contact with vacuum. If a photon hits a POLISH surface, it is first tested for the probability of Fresnel (near source) reflection. This probability, R, is given by equation 5.7.2 [111].

$$R = \frac{1}{2}\left[\frac{\sin^2(\theta'_i - \theta'_t)}{\sin^2(\theta'_t + \theta'_t)} + \frac{\tan^2(\theta'_{i-}\theta'_t)}{\tan^2(\theta'_i - \theta'_t)}\right] \tag{5.2}$$

where and θ'_i and θ'_t are respectively the angles of incidence and refraction with respect to the local normal (which in this model is parallel to the global normal),. This probability of transmittance, T, in this model is given by:

$$T=1 -R \tag{5.3}$$

In case of refraction, Snell's law is followed. This law is stated as: [110]

$$n_i \sin\theta_i = n_t \sin\theta_t \tag{5.4}$$

where n_i and n_t are the refractive indices of the incidence and transmittance media respectively ; and θ_i and θ_t are the angles of incidence and transmittance with respect to the local normal respectively. Depending on the values of the n_i , n_t , θ_i , total internal reflection may occur in which case the photons are directed back into the incidence medium at an angle which again follows Snell's law. An external diffuse reflective coating with a reflection coefficient, RC, may be specified for this model to redirect some of the transmitted photons back into the incidence medium by Lambertian reflection [111].

iv. Ground

This model simulates a roughened optical surface. The only physical difference between this model and a POLISH surface is that the local surface normals do not all point in the same direction. Therefore, the local normals are not parallel to the global normal but follow a Lambertian distribution. As with the POLISH model, the user has the option of specifying an external diffuse reflective coating with a reflection coefficient, RC, to redirect some of the transmitted photons back into the incidence medium by Lambertian reflection. The distribution of light created by the POLISH and GROUND models are shown in Figure 5.13.

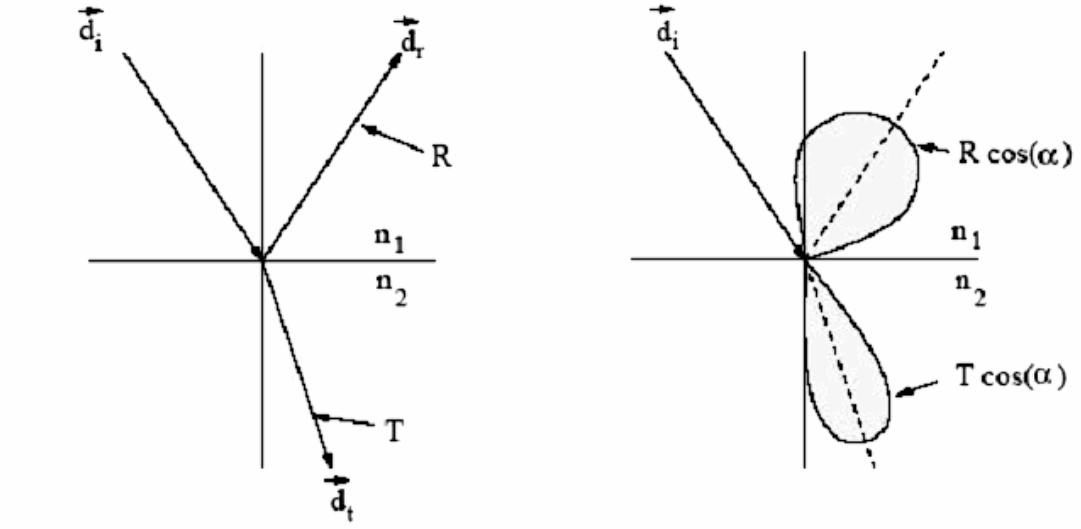

Figure 5.13: Polar plot of the distribution of light created by POLISH (left) and GROUND (right) surface models. $\vec{d}_i$: direction vector of incident photon, $\vec{d}_r$: direction vector of reflected photon, $\vec{d}_t$ direction vector of refracted photon, n_1: index of refraction of incidence medium, n_2: index of refraction of the transmission medium, α: the angle between the local and global normal vectors [112].

v.Unified

In the UNIFIED model, the angle between the local and global normals, α, follows a Gaussian distribution with a mean of zero and a standard deviation, SA, defined by the user. Therefore, the user has the option of defining the degree of surface roughness in this model. As with GROUND and POLISH surfaces, this model allows the user to define an RC for an external diffuse reflective coating to redirect some of the transmitted optical photons back in the medium by Lambertian reflection. In the UNIFIED model the user has the additional option of specifying an index of refraction, NRC, for this surface. This model also allows the user to specify a value for any of the following four types of reflection coefficients:

- C_{sl}: the specular lobe constant. This coefficient controls the probability of specular reflection around a local normal.

- C_{ss}: the specular spike constant. This coefficient controls the probability of specular reflection around the global normal.

- C_{bs}: the backscatter spike constant. This coefficient controls the probability of backward reflection and is usually only applicable to very rough surfaces where a photon may go through several reflections in a deep imperfection and then be reflected back along its initial direction.

- C_{dl}**:** the diffuse lobe constant. This coefficient controls the probability of internal Lambertian reflection.

The sum of these four coefficients is constrained to unity to conserve the probabilities of reflection and transmittance from the surface. A polar plot of the distribution of light created by the UNIFIED model is shown in Figure 5.14. In the figure:

- $\vec{d}_i$: direction vector of incident photon,

- $\vec{d}_r$: direction vector of reflected photon,

- $\vec{d}_t$ direction vector of refracted photon,

- n_1: index of refraction of incidence medium,

- n_2: index of refraction of the transmission medium,

- SA: the standard deviation of the distribution of the angle of the local normal vectors with the global normal,

- T: transmittance distribution.

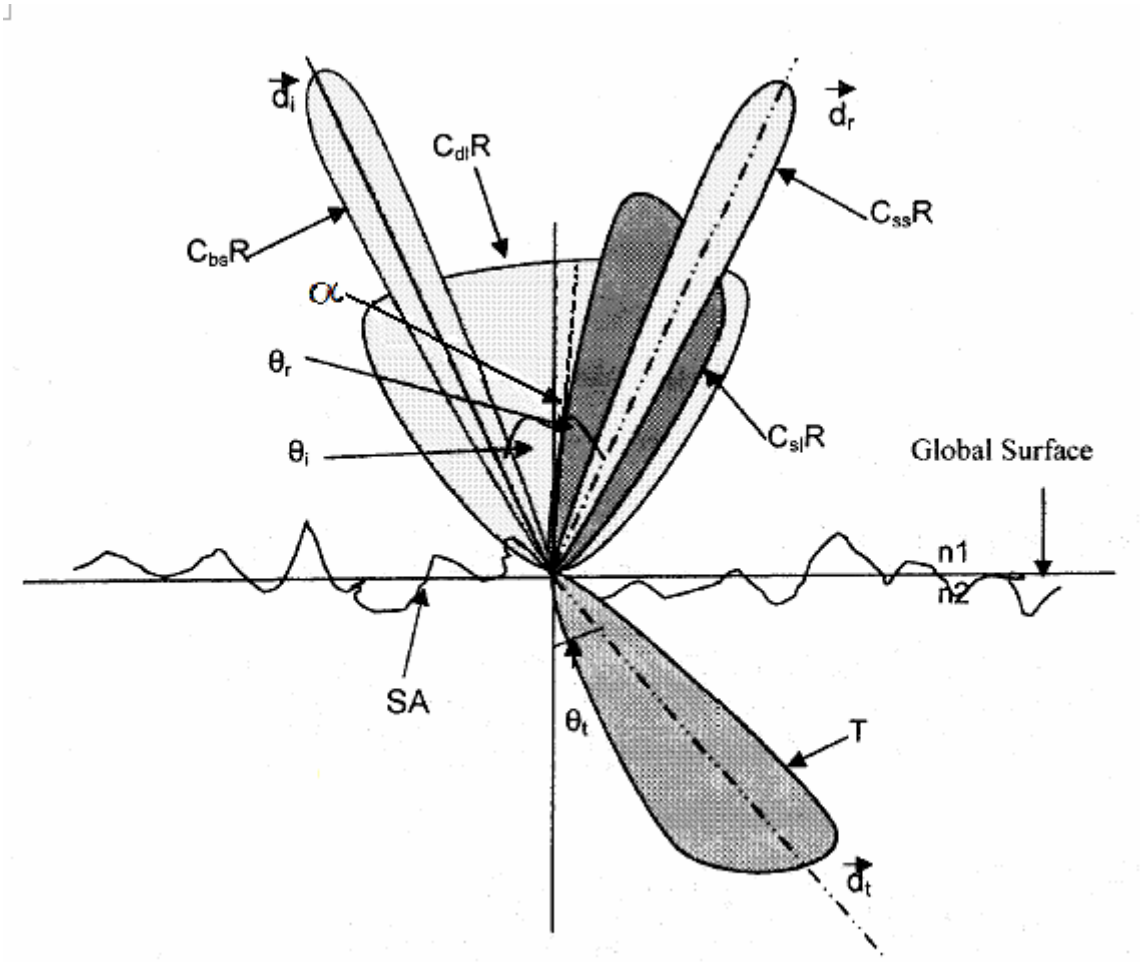

Figure 5.14: Polar plot of the distribution of light created by UNIFIED surface models [109, 110].

vi. Detect

This specification represents a photo sensor (a photocathode or any other photon detecting layer). As an option, the photocathode may be located on the opposite surface of a thin window of chosen refractive index. Unless otherwise specified, the quantum efficiency is assumed to be unity, so that every photon reaching the photocathode is detected [105].

5.8 Position Sensitive Surface Definition with DETECT2000:

A new feature that has been developed in DETECT2000 is the position sensitive detection surfaces to simulate the behaviour of PS-PMT. This kind of detection surfaces in fact an optional that can be activated for any detection surface in the model. When this is activated, the position of each detected light photon is recorded inside the surface. At the end of each simulation, the centroid of all the detected photon is written along with the simulation results. Because the data is stored inside the surface finish definition, it is possible to merge many detection surfaces into one centroid data [105].

The centroid is computed for all photons that interact with that finish, i.e. there is no individual centroids for each component containing the position sensitive DETECT finish. In order to have an individual centroid, each component should have its unique DETECT finish.

The declaration of a position sensitive DETECT surface is done by adding PS suffix in the finish declaration line [109].

5.9 Simulation Assumptions

To optimize the detector, several parameters were also adjusted:

1- During the simulation studies the number photons per keV for LSO:Ce crystal was accepted 27.1 as informed in the GRIT documentation. For each interaction vertex the number of scintillation photons released was computed as the product of the energy lost at the vertex and the known light yield (27.1 photons /keV) per unit of deposited energy for the scintillator material [116]. The LSO light yield relates the number of scintillation photons emitted at an interaction point, L_i to the energy deposited, E_i by:

$$L_i = E_i \text{ x } 27.1 \text{ photons/keV} \qquad (5.5)$$

During the simulations, it was assumed that for a 511 keV gamma ray that was absorbed in a photoelectric effect, approximately 13848 scintillation photons were produced. Also, performed simulations showed that changes in the light yield of LSO

have no effect on position reconstruction distribution [57]. Apart from these, in reality, light yield of LSO has a big variation depend on the total amount of doping material of cerium (Ce). The total Ce can be measured by various techniques including glow discharge mass spectroscopy, inductively coupled plasma mass spectroscopy, and X-ray fluorescence. However, according to crystal developer's experiences, the results of light yield belong to LSO(Ce) usually have uncertainties in excess of 20% and often times much greater due to the lack of reliable calibration standards in the matrix of interest [57,108,113,114] .

2- An inconvenience of DETECT is the hard-coding of the quantum efficiency in the program which does not allow for quick modifications because re-compilation is necessary. Therefore, an additional module was written to solve this problem related with the quantum efficiency of PS-PMTs. The single photon detection efficiency of PS-PMT was taken as 22,5%. Therefore, the number of light photons tracked were just reduced by a factor of 22,5 for the given detection efficiency of PS-PMT model. However, in the original TRIUMF simulator, DETECT module assumes quantum efficiency 1 for simulation time consideration. (see Appendix H)

3- The crystal surface roughness was accepted truly random.

4- During the simulations, it was accepted that there was no crack in the scintillation crystal.

5- The coupling material between the scintillation block and the PMT did not absorb or scatter light photons. When a light photon crosses the optical glue, it cannot go back.

6- It was, also, accepted that the crystal has maximum stopping power.

7- It was assumed that all photon interactions occurred at the same interaction depth. (Subsequent Compton events belongs to same gamma ray interaction were accepted as one event)

8- The selected energy window was between 300 to 511keV.

5.10 Positioning Logic Used in the Simulation:

Events were positioned from the collected light signals using Anger logic (Center of gravity). Classical algorithm commonly used in PET for photon positioning is the Anger algorithm, which is based on centroid arithmetic. This algorithm finds the centroid point (center of gravity or mass) according to the ratio of the PS-PMT anode signals. The centroid serves an estimation of the scintillation point. The image is then reconstructed calculating the single event centroid coordinates of X and Y using the algorithm below:

$$X = \frac{\sum_{1}^{i} w_i q_{xi}}{\sum_{1}^{i} q_{xi}} \qquad Y = \frac{\sum_{1}^{i} w_i q_{yi}}{\sum_{1}^{i} q_{yi}} \tag{5.6}$$

w_{xi}, w_{yi} being the charge-weighting factors assumed linearly proportional to the anode position, that is the distance from the center (x=0) and q_{Xi}, q_{Yi} the digitized values proportional to the charges on the i^{th} anode along X and Y directions, respectively [117,118].

5.11 A Sample Input Macro and Output File:

For one simulation, a sample input macro and output file is given in Appendix F.

6. RESULTS AND DISCUSSION

6.1 Results:

The results of the simulation studies are presented under three different titles:

- Averaged Energy Resolution
- Average Spatial Resolution
- Averaged Image Compression

Average Energy and Spatial resolution graphics can be obtained as Gaussian distribution curves. These curves can be quantified as the FWHM. (For more information see Appendix G)

Regarding average image compression graphics, they can be obtained by the help of flood source position maps resulting from a position sensitive PMT model and linear Anger Logic.

6.1.1 Average Energy Resolution

During the simulations, it was assumed that for a 511 keV gamma ray that was absorbed in a photoelectric effect, approximately 13848 scintillation photons were produced. In fact, the all optical flashes have a range of energies, and this will affect the final image quality, if compensatory steps are not taken. Firstly, the optical pulse height spectrum for monoenergetic incident gamma rays has been considered. A sample energy resolution graphic obtained from the simulation is shown below in Figure 6.1.

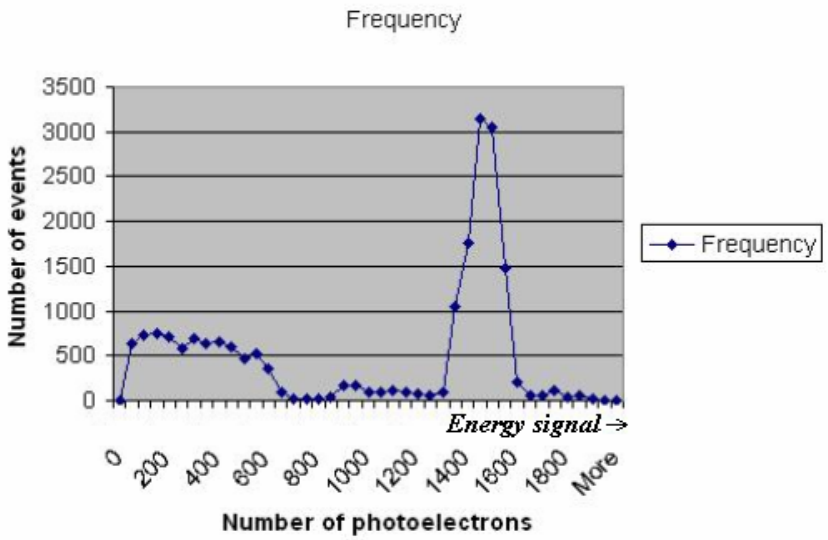

Figure 6.1: A sample energy resolution graphic obtained from the simulations.

After calculating average value of energy resolution results (according to crystal thickness and surface treatment type), the related graphics were plotted altogether below in Figure 6.2.

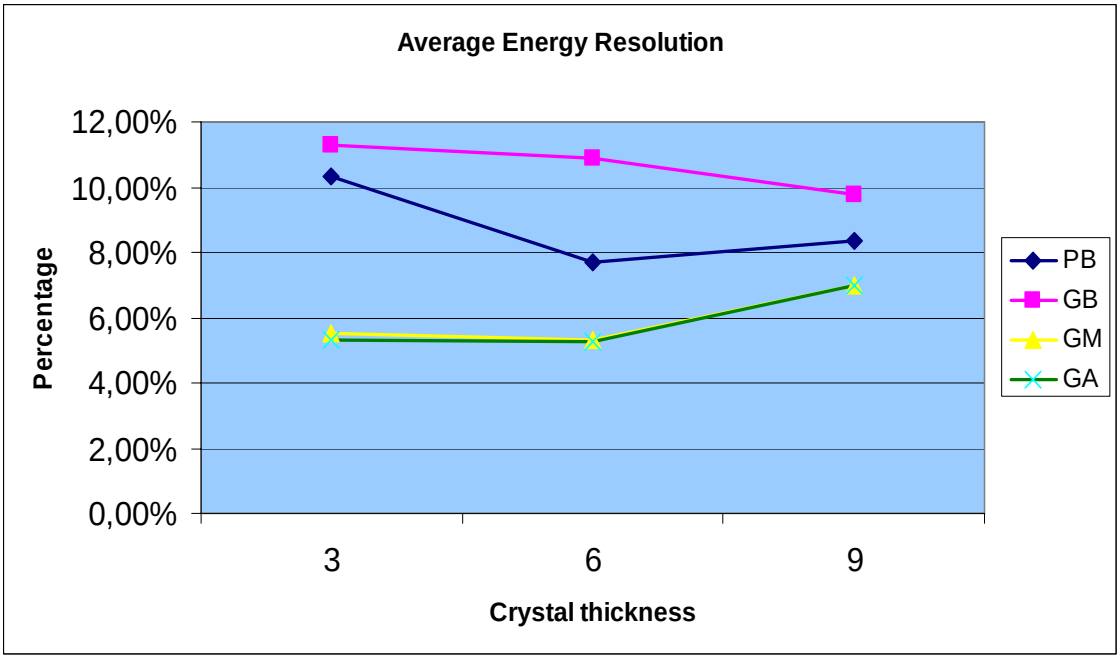

Figure 6.2: Average energy resolution according to crystal thickness and the surface treatments.

6.1.2 Average Spatial Resolution

When a point source emission passes through a very small diameter channel of a collimator, it is detected by a scintillation crystal and as a result, a scintillation spot occurs.

Even the scintillation crystal side of collimator is in direct contact with the scintillation crystal face, this spot is always bigger than collimator channel diameter, (light spreading = blurring).

Common method to measure this blurring in positron emission tomography is to image this point source giving a point spread function (PSF) (Gaussian distribution curve). 2-D graph of this function is shown in Figure 6.3.

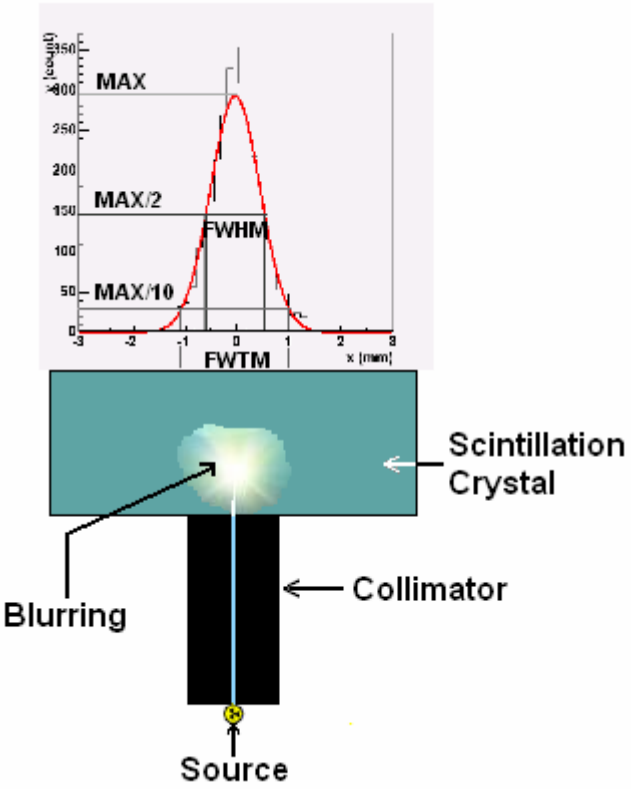

Figure 6.3: Schematic presentation of point spread function (FWHM-FWTM)

When it is worked with a line or more than one point sources throughout one straight line or if it is moved a point source more than one coordinates along a straight line, in this case, it is obtained more than one point spread functions (PSFs) and PSF term is turned into LSF (line spread function).

The source locations in this study were explained in Chapter 5 with full details and the all the detection results were given as LSF (Line Spread Function) graphics, respectively.

These graphics showed us the importance of the LSF variations according to crystal thickness differences, explored surface treatments and source locations. See Figures 6.4-6.12.

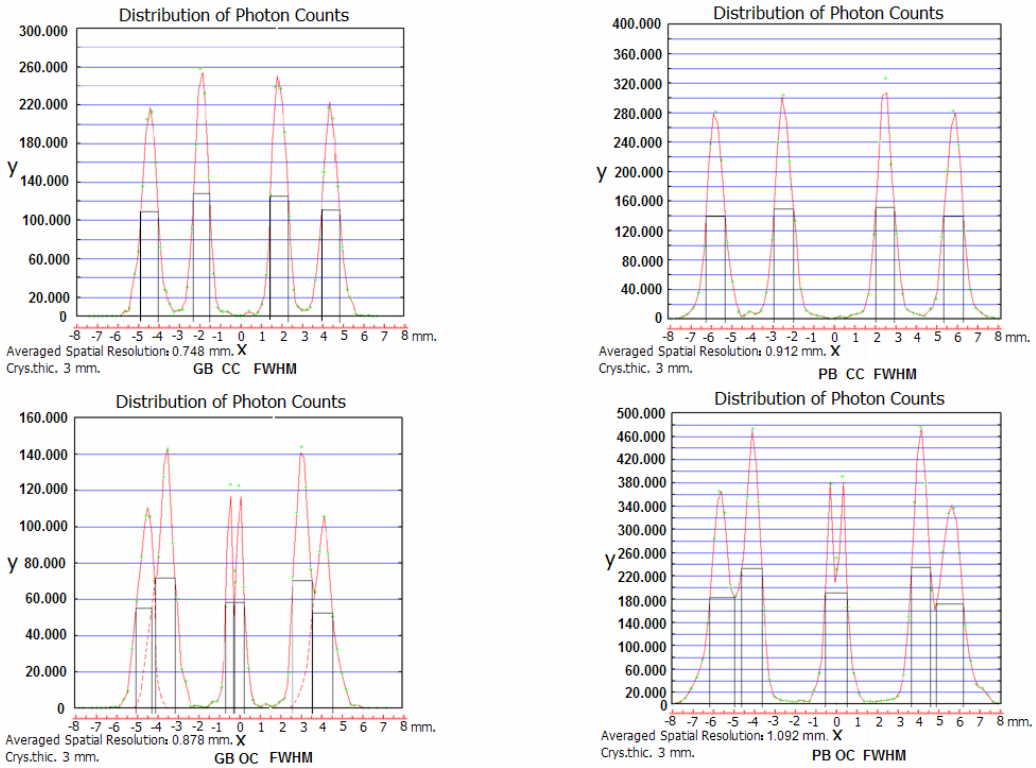

Figure 6.4: Ground + Black, Polished + Black 3mm 0.05RC-0.95RC, 3mm, center (cc) and out of center (oc) LSF graphs.

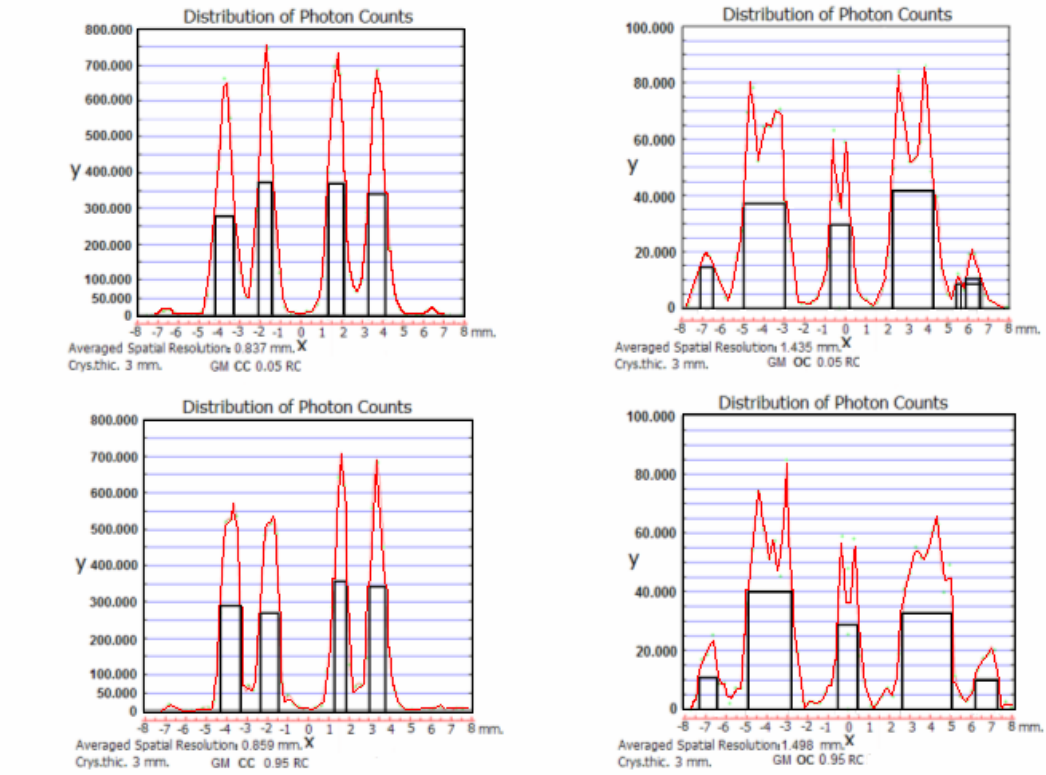

Figure 6.5: Ground + Methacrylate, 0.05RC-0.95RC, 3mm, center (cc) and out of center (oc) LSF graphs.

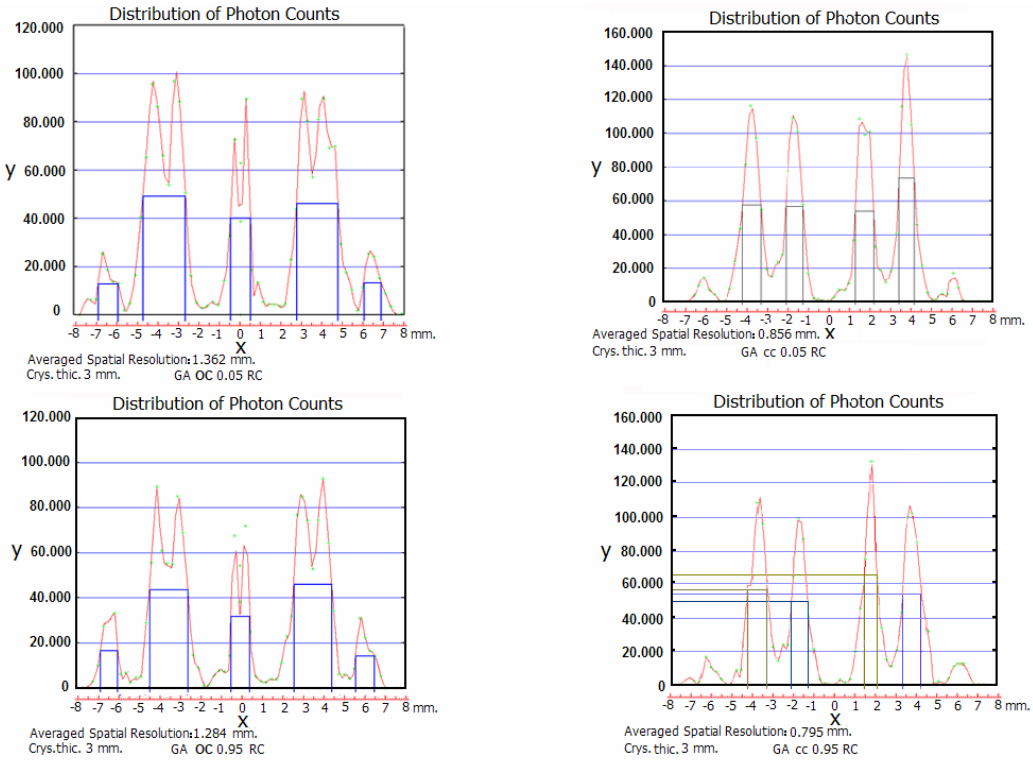

Figure 6.6: Ground + Air, 0.05RC-0.95RC, 3mm, center (cc) and out of center (oc) graphs.

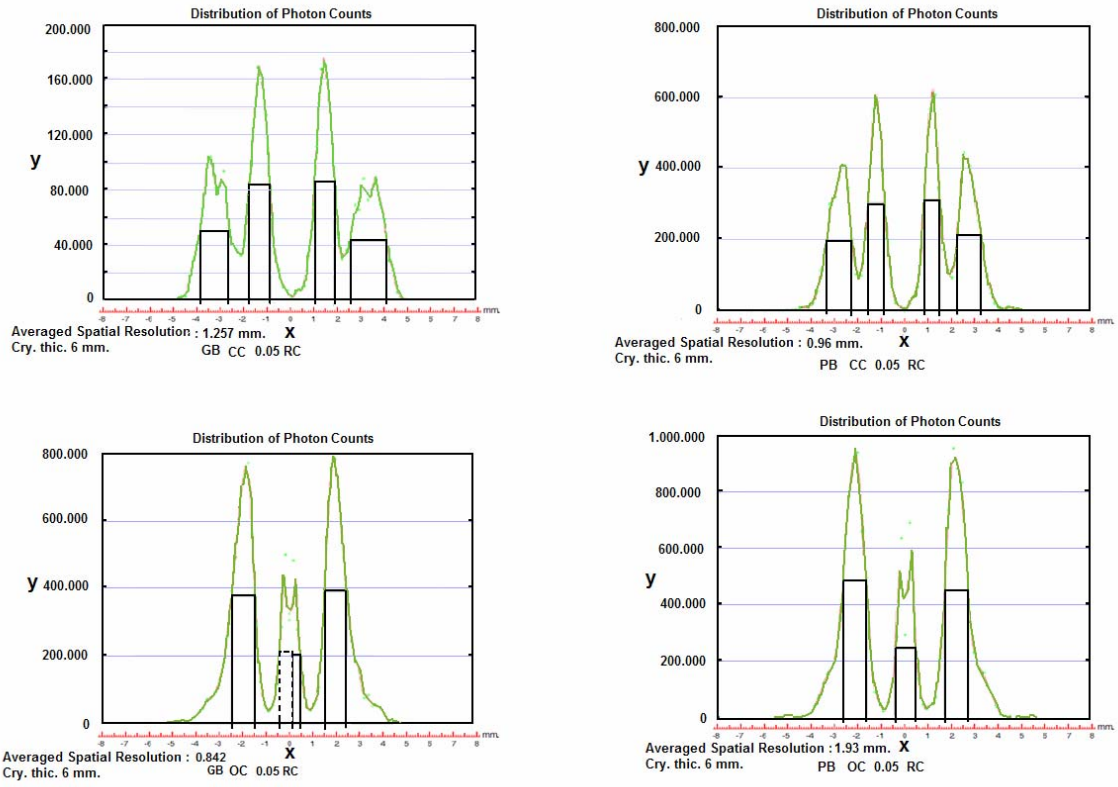

Figure 6.7: Ground + Black, Polish + Black 6mm 0.05RC - 0.95RC, 6 mm, center (cc) and out of center (oc) LSF graphs.

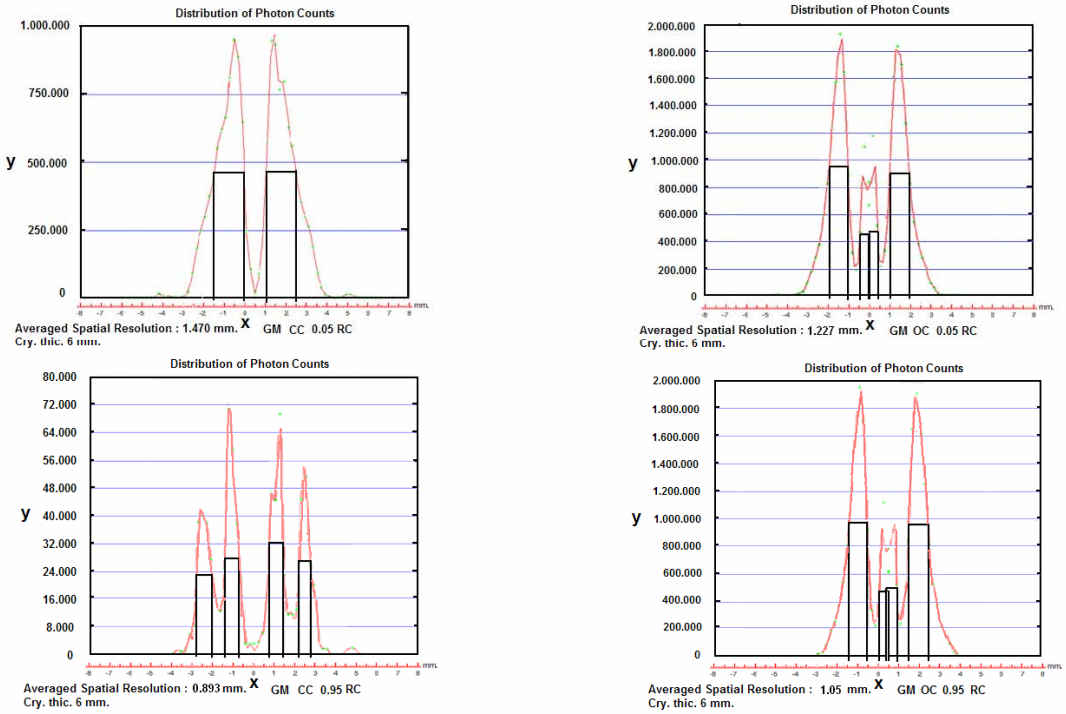

Figure 6.8: Ground + Methacrylate, 0.05RC-0.95RC, 6mm, center (cc) and out of center (oc) LSF graphs.

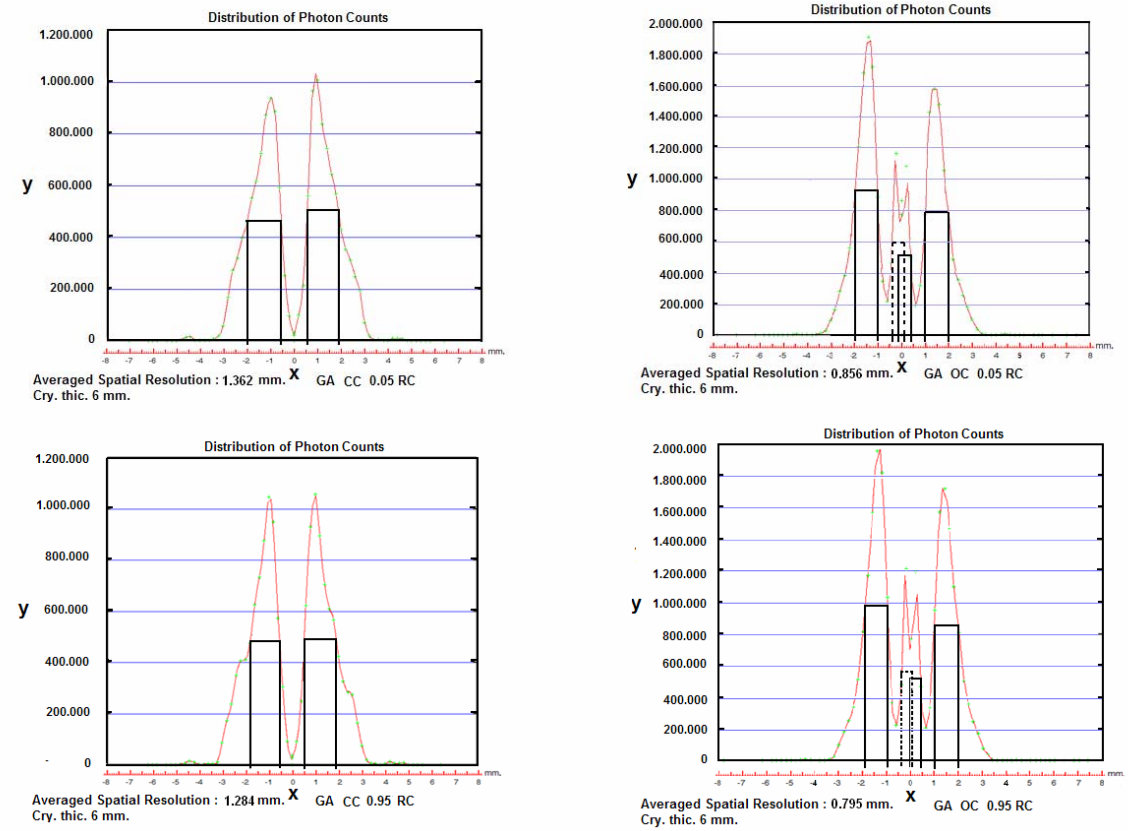

Figure 6.9: Ground +Air, 0.05RC-0.95RC, 6mm, center (cc) and out of center (oc) LSF graphs.

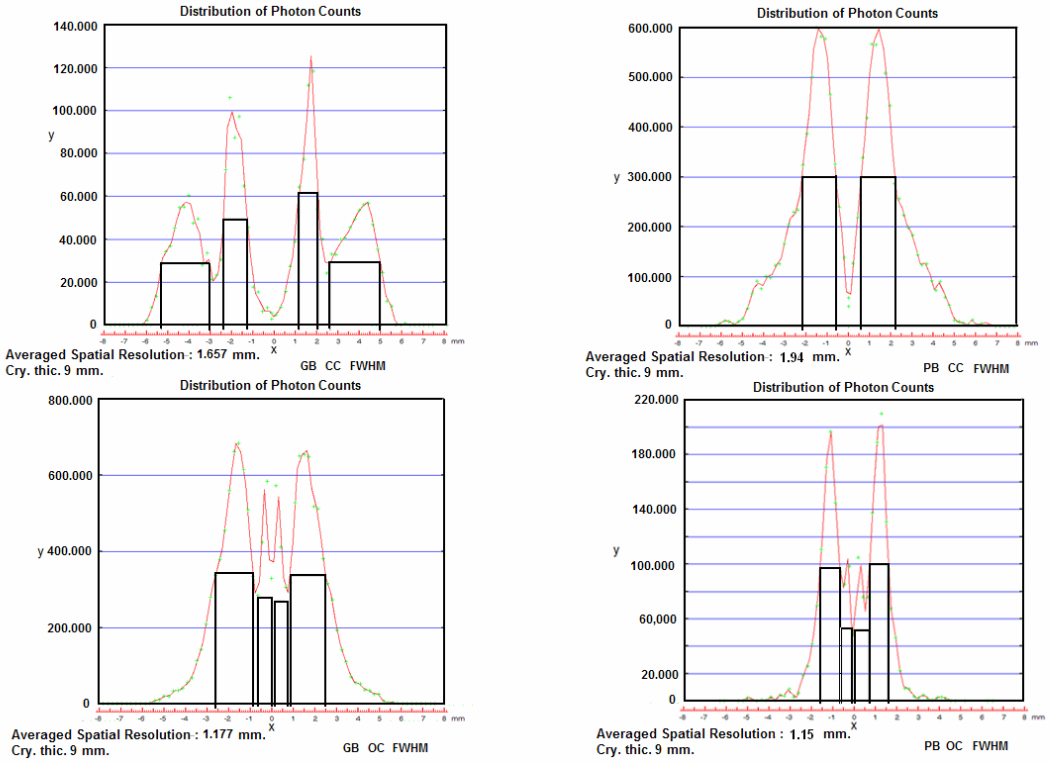

Figure 6.10: Ground + Black, Polish +Black 9mm 0.05RC-0.95RC, center (cc) and out of center (oc) LSF graphs.

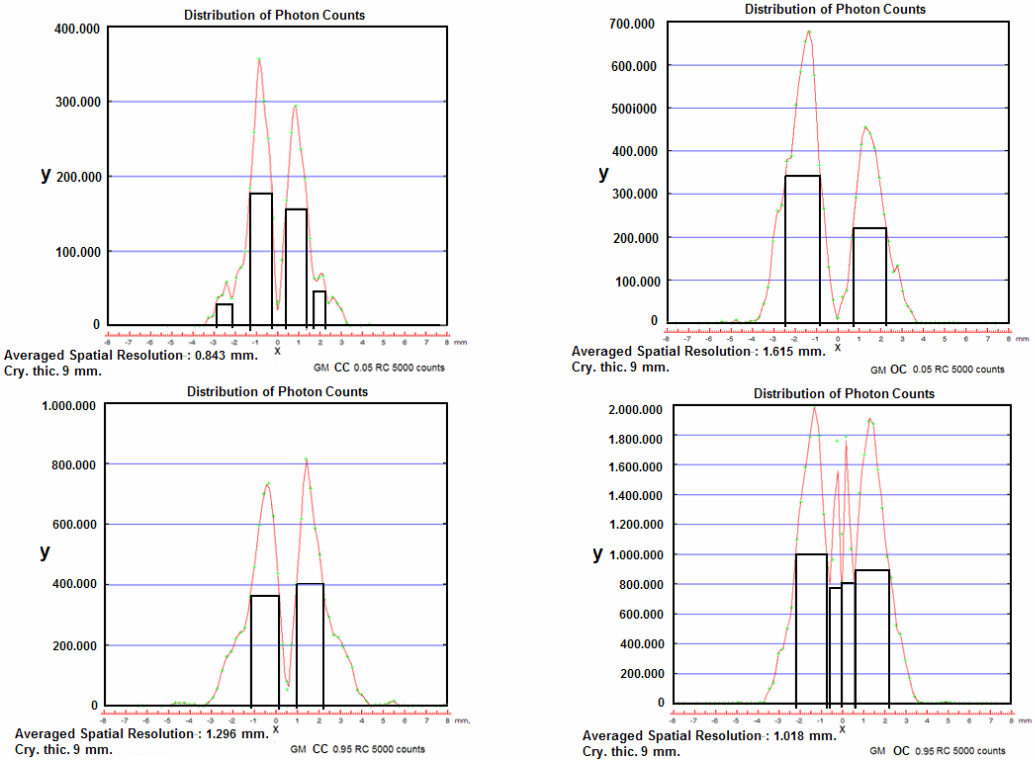

Figure 6.11: Ground + Methacrylate, 0.05RC-0.95RC, 9 mm, center (cc) and out of center (oc) LSF graphs.

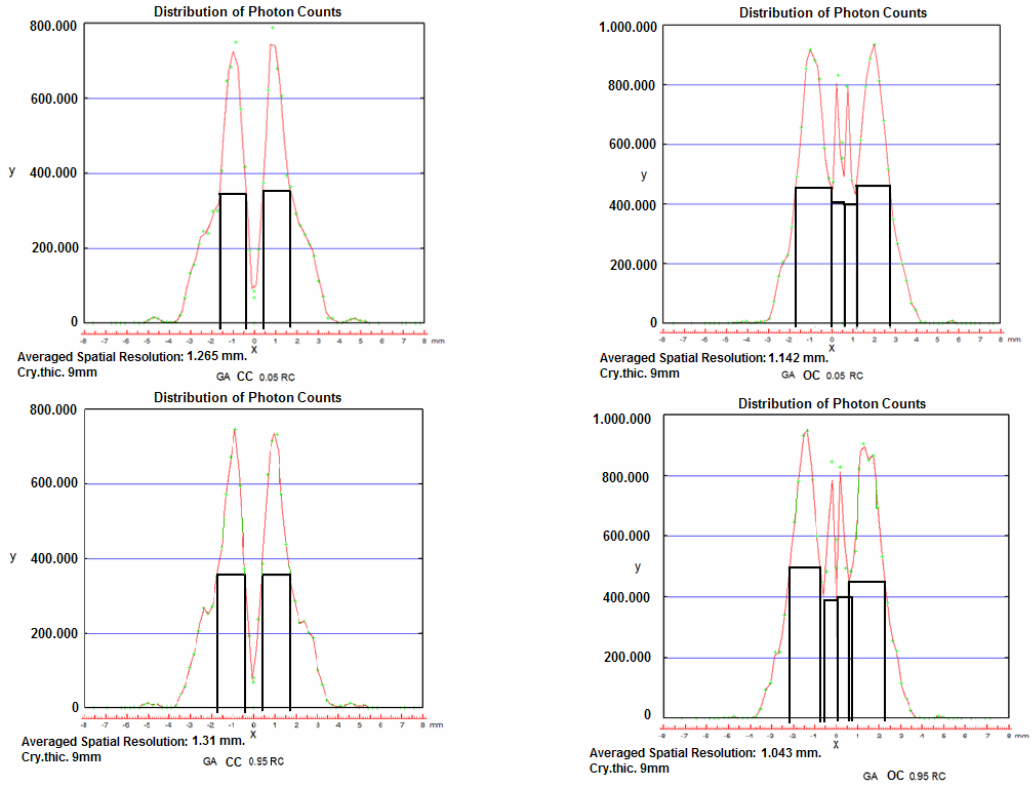

Figure 6.12: Ground + Air, 0.05RC- 0.95RC, 9mm, center (cc) and out of center (oc) LSF graphs.

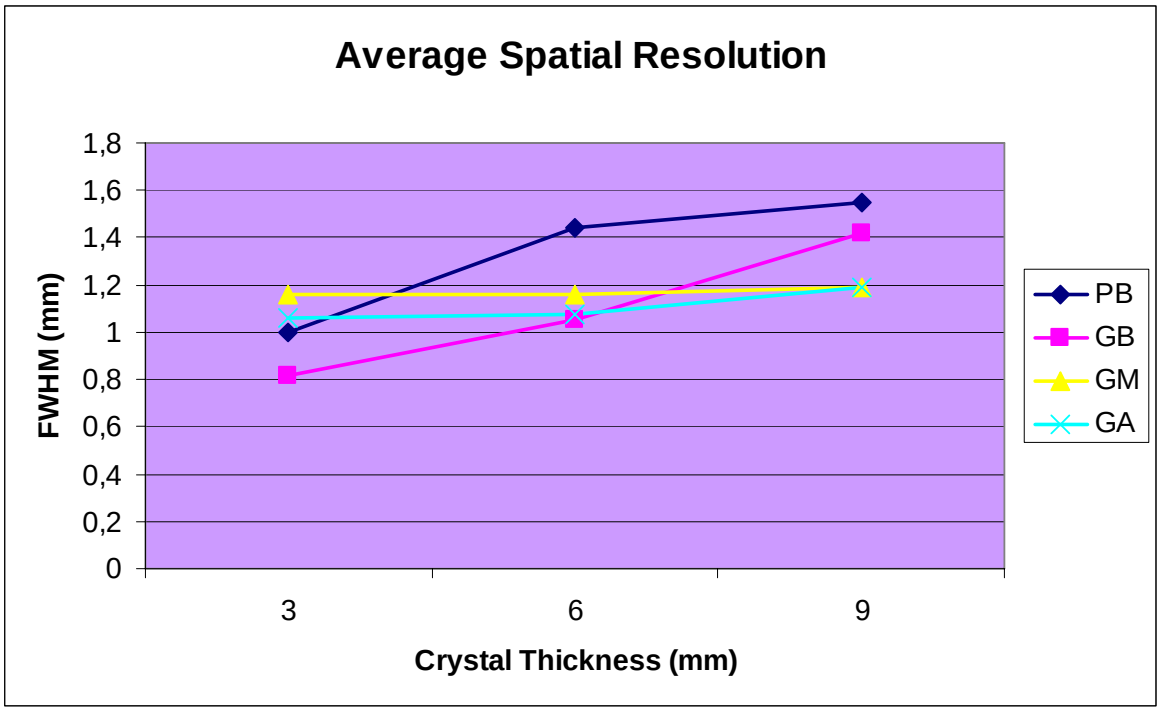

Figure 6.13: Average spatial resolution graph according to crystal thickness and the surface treatments.

6.1.3 Average Image Compression:

The simulation results related with the image compression were plotted benefiting from Matlab.

The name of this plotting is the map of flood source positioning and the colours of maps were selected for the best interpretation of them. One of the examples from these maps is shown below in Figure 6.14.

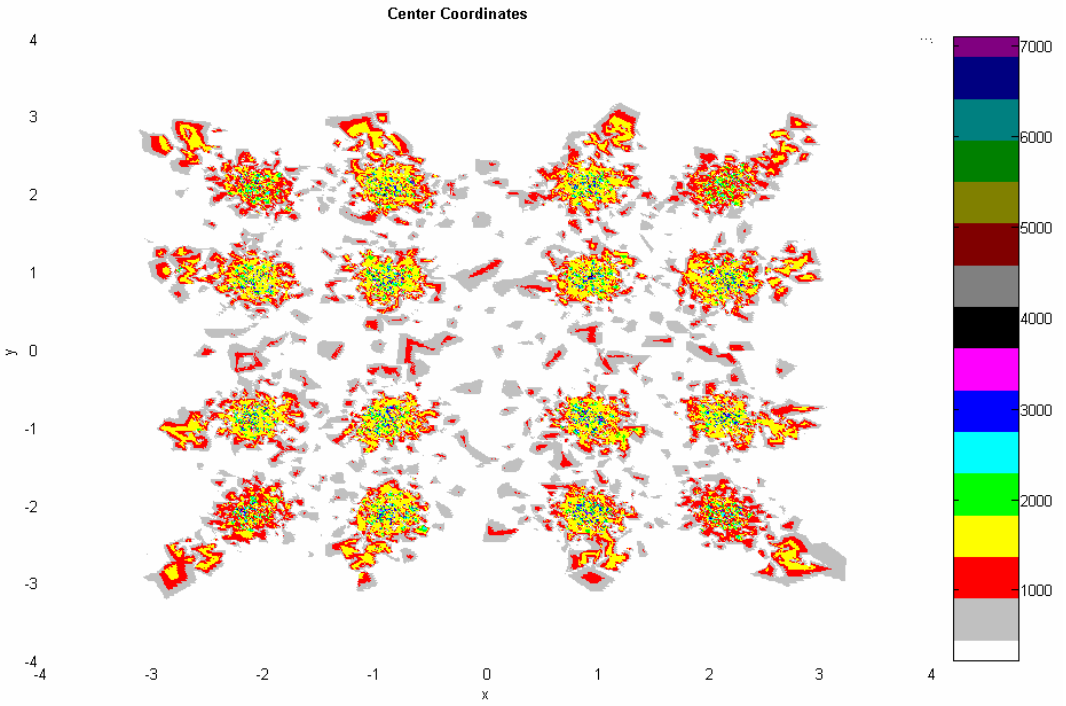

Figure 6.14: A flood source position map resulting from a position sensitive photomultiplier tube (PS-PMT) and linear Anger logic.

In this figure, there are two components. The first component represents the scintillation crystal behaviour according to the source coordinates; the second component (a colored vertical rectangular) represents the count number or concentration according to the specific source location.

Typical flood source position maps are shown below respectively according to the crystal thickness, explored surface treatment (RC values and surface finishes) and the source locations. (Figures 6.15 - 6.50)

6.1.4 Flood Source Position Maps for 3mm Crystal Thickness

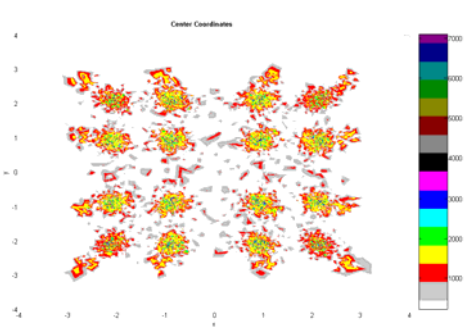

Figure 6.15: Polished +Black_3mm_cc

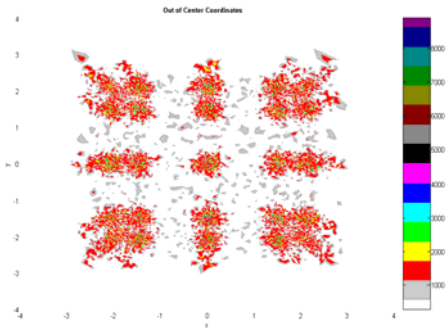

Figure 6.16: Polished +Black_3mm_oc

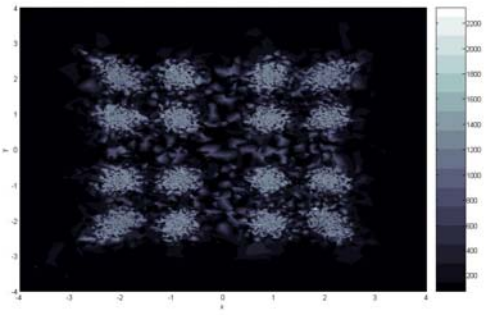

Figure 6.17: Ground + Black_3mm_cc_3mm

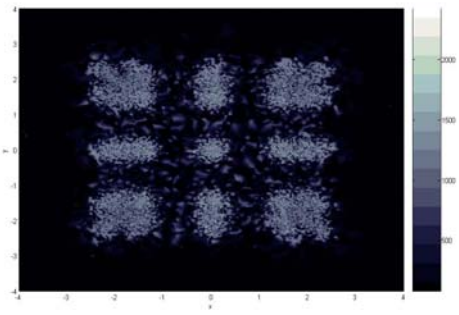

Figure 6.18: Ground + Black_3mm_oc_3mm

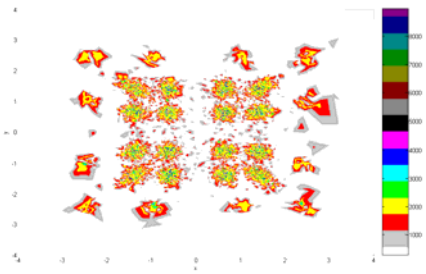

Figure 6.19: Ground + Metha._3mm_cc_0.05RC

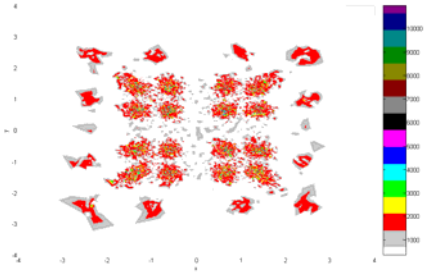

Figure 6.20: Ground + Metha._cc_0.95RC_3mm

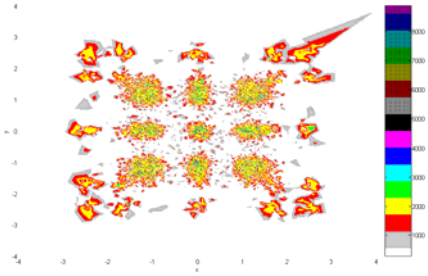

Figure 6.21: Ground +Metha._oc_3mm_0.05RC

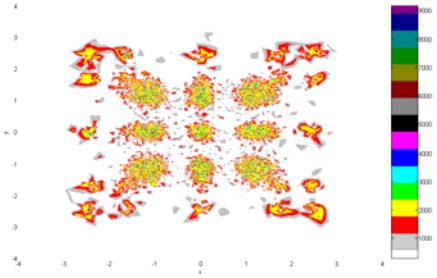

Figure 6.22: Ground + Metha._oc_0.95RC_3mm

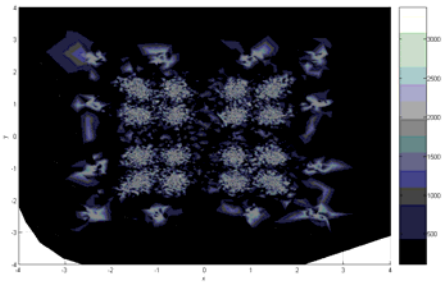

Figure 6.23: Ground + Air_3mm_0.05RC_3mm_cc

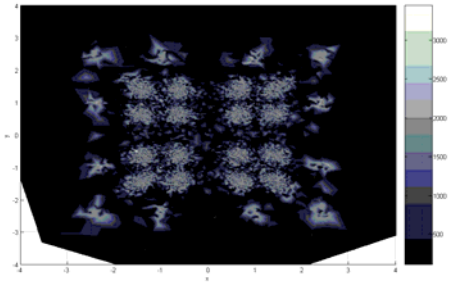

Figure 6.24: Ground + Air_0.95RC_cc_3mm

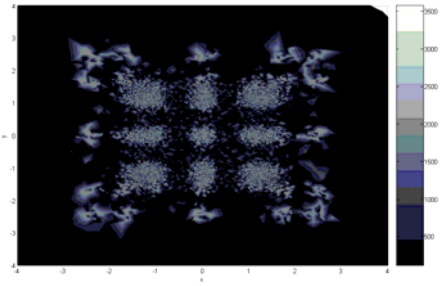

Figure 6.25: Ground + Air_0.05RC_oc_3mm

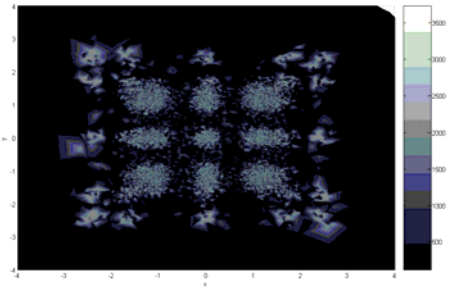

Figure 6.26: Ground + Air_0.95RC_oc_3mm

6.1.5 Flood Source Position Maps for 6 mm Crystal Thickness

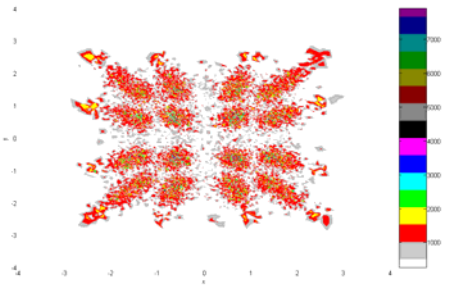

Figure 6.27: Polished + Black_cc_6mm

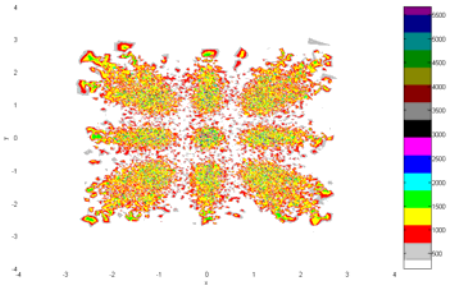

Figure 6.28: Polished + Black_oc_6mm

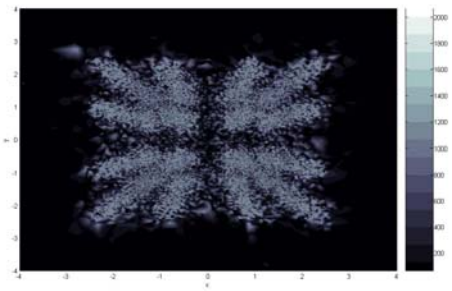

Figure 6.29: Ground + Black_cc_6mm

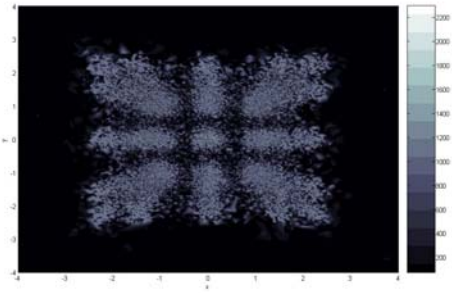

Figure 6.30: Ground + Black_oc_6mm

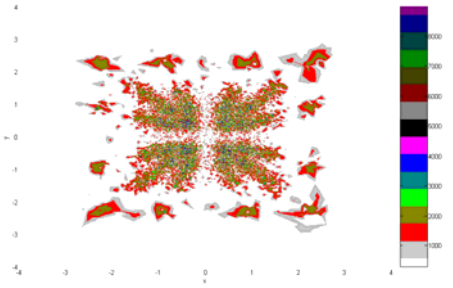

Figure 6.31: Ground + Metha._6mm_cc_0.05RC

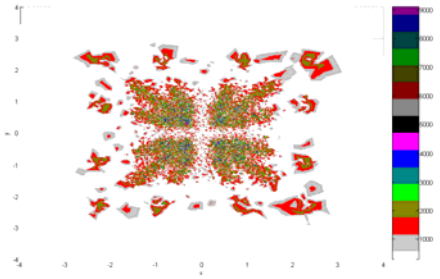

Figure 6.32: Ground + Metha._cc_0.95RC_6mm

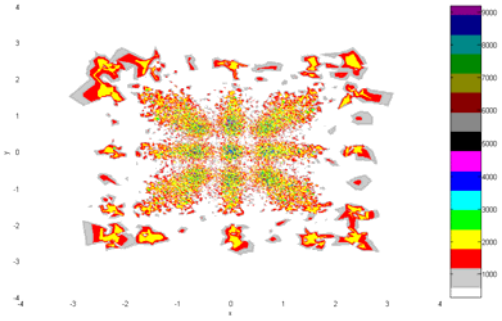

Figure 6.33: Ground + Metha._oc_6mm_0.05RC

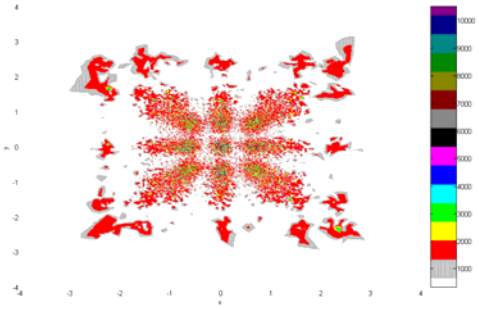

Figure 6.34: Ground + Metha._oc_0.95RC_6mm

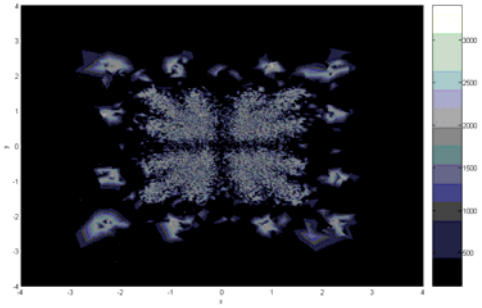

Figure 6.35: Ground + Air_6mm_0.05RC_cc

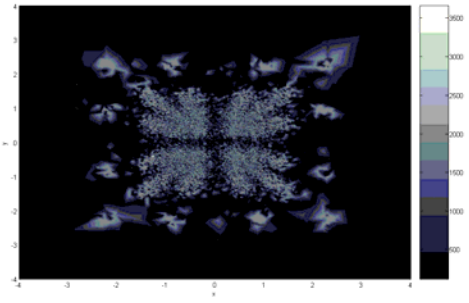

Figure 6.36: Ground +Air_cc_0.95RC_6mm

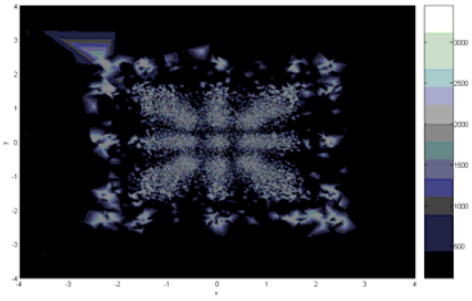

Figure 6.37: Ground + Air_oc_6mm_0.05RC

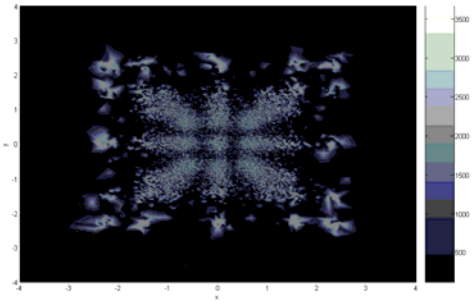

Figure 6.38: Ground +Air_oc_0.95RC_6mm

6.1.6 Flood Source Position Maps for 9 mm Crystal Thickness

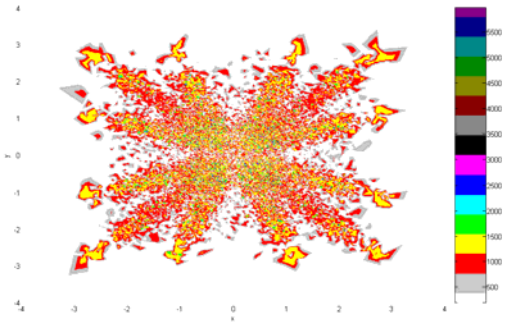

Figure 6.39: Polished +Black_cc_9mm

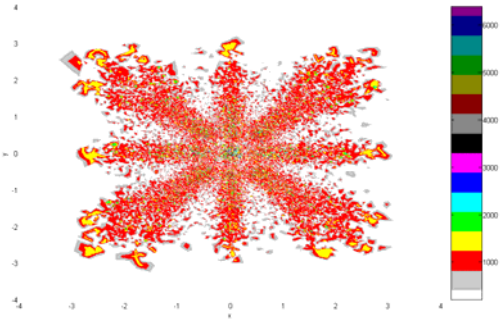

Figure 6.40: Polished +Black_oc_9mm

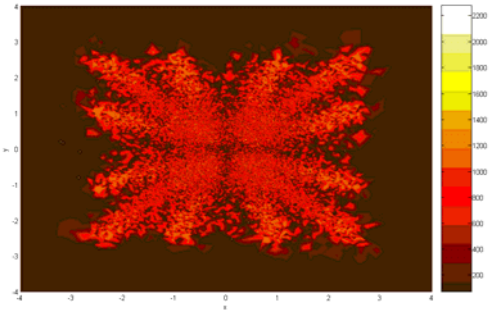

Figure 6.41: Ground + Black_cc_9mm

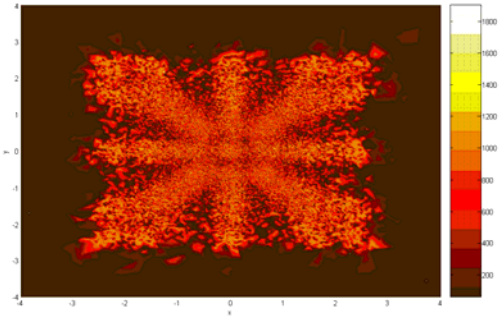

Figure 6.42: Ground + Black_oc_9mm

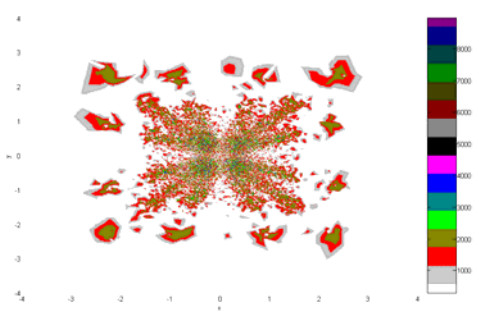

Figure 6.43: Ground + Metha._cc_9mm_0.05RC

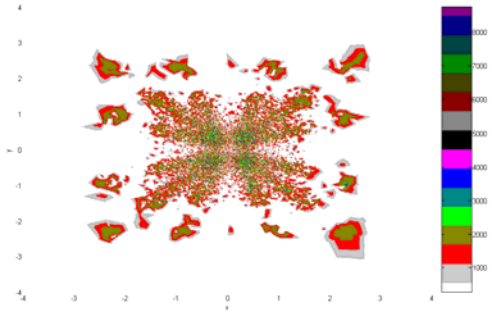

Figure 6.44: Ground + Metha._cc_0.95RC_9mm

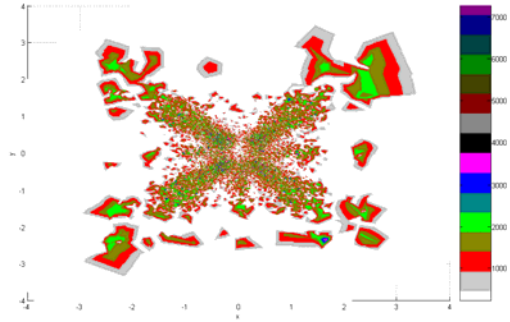

Figure 6.45: Ground + Metha._oc_0.05RC_9mm

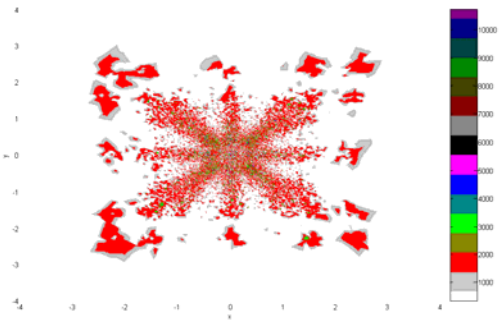

Figure 6.46: Ground + Metha._oc_0.95RC_9mm

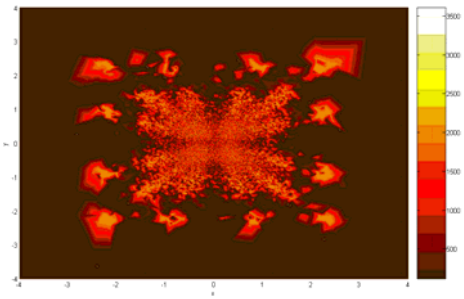

Figure 6.47 : Ground +Air_9mm_cc_0.05RC

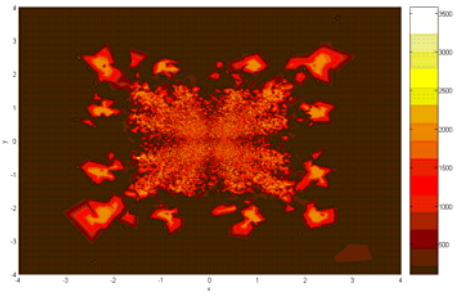

Figure 6.48 : Ground + Air_cc_0.95RC_9mm

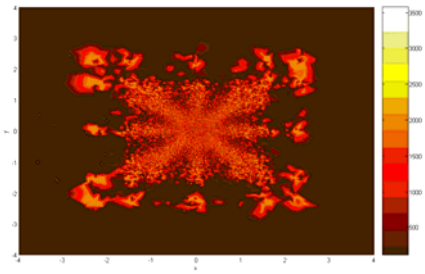

Figure 6.49: Ground + Air_oc_0.05RC_9mm

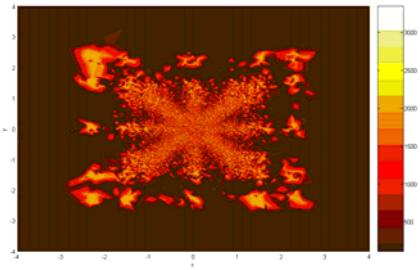

Figure 6.50: Ground + Air_oc_0.95RC_9mm

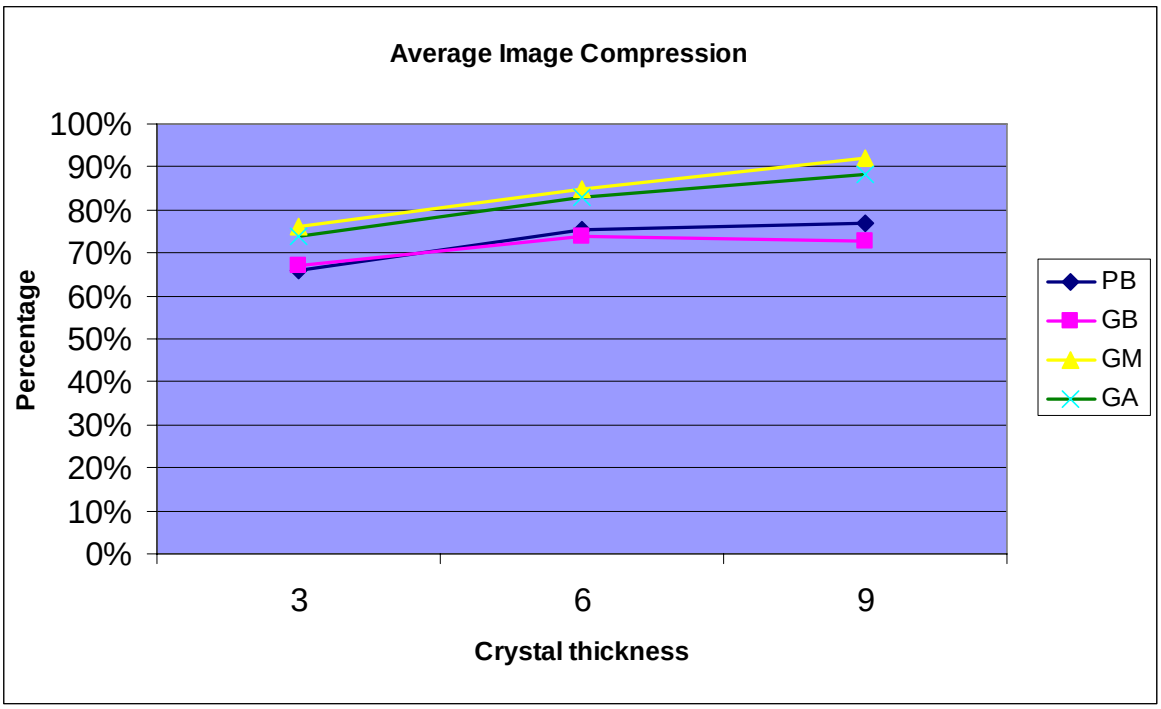

Figure 6.51: Average image compression according to crystal thickness and surface treatment

Finally, all of three variation averages are given below in Table 6.1

Table 6.1: Average values obtained from the simulations.

Polished-Black (PB)			
Thickness	Average Energy Resolution	Average Spatial Resolution	Average Image Compression
3	10,34%	1,002 mm	66,00%
6	7,69%	1,445 mm	75,40%
9	8,33%	1,545 mm	76,83%
Ground-Black (GB)			
Thickness	Average Energy Resolution	Average Spatial Resolution	Average Image Compression
3	11,30%	0,8130 mm	67,00%
6	10,87%	1,0495 mm	73,90%
9	9,76%	1,4170 mm	72,80%
Ground-Methacrylate (GM)			
Thickness	Average Energy Resolution	Average Spatial Resolution	Average Image Compression
3	5,51%	1,157 mm	76,00%
6	5,33%	1,160 mm	85,00%
9	7,00%	1,193 mm	92,00%
Ground-Air (GA)			
Thickness	Average Energy Resolution	Average Spatial Resolution	Average Image Compression
3	5,30%	1,059 mm	74,00%
6	5,26%	1,074 mm	83,00%
9	7,00%	1,190 mm	88,40%

All of these graphics shown above (including energy and spatial resolution and image compression) are the results of 738 different simulation studies.

6.2 DISCUSSION

Discussions of our findings are made in the same order with the initial part of the Chapter 6.

6.2.1 Discussion of Energy Resolution Results:

According to classical knowledge related with energy resolution in a scintillation crystal, there should be a parallelism with the thickness of the scintillation detector and the measured energy resolution percentage in the opposite direction. However, the value of energy resolution percentage is not satisfactory yet, because the full width at half maximum (FWHM) of energy resolution is still high for small animal PET detectors.

In order to obtain more satisfactory FWHM values, many investigators have explored different crystal thickness, chemistry, density, geometric structure and surface treatment since 1980s.

In this work, before selecting the crystal thickness and reflection coefficient (RC), all the obtainable publications were checked. It was seen that a few research teams have worked with a monolithic crystal by using three different thicknesses(1mm-2mm-3mm) [124] and studied different RC values for different surface finishes of the selected scintillation crystals [125].

For these reasons, three different thicknesses as 3mm-6mm-9mm and different RC values (0.05RC and 0.95RC) for different crystal coatings were preferred.

In this study, the light output of different surface treatments and reflector materials at LSO crystal were explored and it was found that Ground + Air (GA) and Ground + Methacrylate (GM) gave the best results in terms of the average energy resolution.

Apart from these, when the simulation results related with the energy resolution of the GA and GM were compared, it was seen that GA gave the slightly better results than GM.

Regarding the crystal thickness, the best energy resolution results were obtained at 6 mm crystal thickness except GB (Ground + Black surface treatment).

6.2.2 Discussion of Spatial Resolution Results:

According to classical knowledge related with spatial resolution in a scintillation crystal, there should be a parallelism with the thickness of the scintillation detector and the measured energy resolution percentage in the same direction.

In this study, the best spatial resolution result was obtained with Ground + Methacrylate (GM) and Ground + Air (GA). When dealing with all the simulation results in terms of the spatial and energy resolution and also image compression, it is seen that GA (Ground + Air) surpasses the all the others. Also, Ground + Methacrylate surface treatment results are the close pursuer of Ground + Air one.

6.2.3 Discussion of Image Compression Results:

Pin cushion distortion is a divergence from rectilinear projection in geometric optics where image magnification increases with increasing distance from the optical axis.

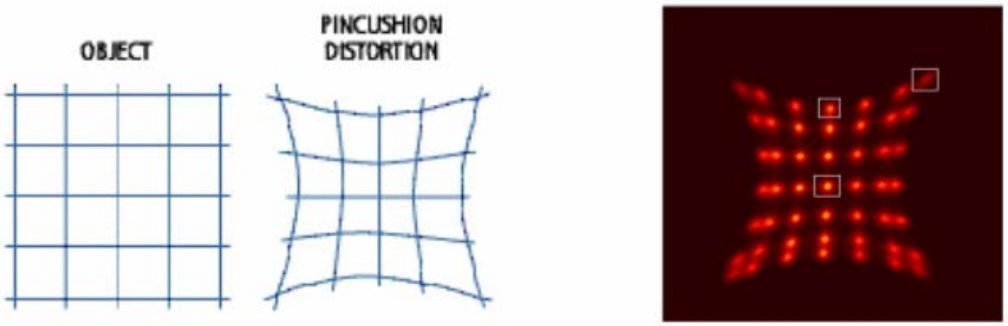

Figure 6.52: Pincushion Distortion [121].

Results of the simulation studies showed severe image compression .The name of the image compression in geometric optics is the pincushion effect. See Appendix G for reasons of image compression [119,120,121,122,123].

In this work, the better image compression results were obtained with Ground + Black (GB) and Polished + Black (PB). When the image compression results of GB and

PB are compared, GB is slightly better than PB. In contrast to spatial and energy resolution results, image compression is better for PB and GB.

However, when dealing with all the simulation results in terms of the spatial and energy resolution and also image compression, it is seen that GA (Ground + Air) surpasses all the others. Also, Ground + Methacrylate (GM) surface treatment results are the close pursuer of Ground + Air (GA) one. Additionally, 6mm crystal thickness is found more satisfactory.

7. CONCLUDING REMARKS

At the beginning aims of this study were to develop a more satisfactory and low cost PET detector design dedicated to small animal brain imaging using a conventional continuous Lutetium Oxyorthosilicate (LSO) crystal coupled to a position sensitive photomultiplier tube (PS-PMT). For this aim, DETECT2000 simulation platform was used to simulate the explored monolithic (continuous) position encoding scintillation crystal design.

Main feature of the simulation program is this interface between gamma ray interaction with the propagation and detection of scintillation photons. The former feature is determined by the bulk properties of the inorganic scintillator and allow to realistically modelling the energy deposition in the active volume of the continuous detector through photoelectric and Compton interactions. The latter feature is dominated by the geometry and optical properties of monolithic LSO, as well as the PS-PMT coupling scheme. Combining the two clearly provides and realistic optimization tool more than geometrical and optical optimization alone.

However, an inconvenience of DETECT2000 is the hard-coding of the quantum efficiency in the program which does not allow for quick modifications because re-compilation is necessary. Therefore, an additional module was written to solve this problem related with the quantum efficiency of PS-PMTs. The written special module took the single photon detection efficiency of PS-PMT is 22, 5%. Therefore, the number of light photons tracked have been just reduced by a factor of 22,5 for the given detection efficiency of PS-PMT model. However, in the original TRIUMF simulator, DETECT module assumes quantum efficiency 1 for simulation time consideration.

The data analysis of simulation outputs have taken for a long time. Therefore, all the data lines in the output files belong to GRIT and DETECT programs were checked by the help of using Linux operation system. Then, by taking only the necessary lines and figures (all data were separated by commas), a text file which can be imported to the Excel in Windows XP operation system was prepared. Thus, spending of time for the data analysis was reduced. Finally, all the average energy resolution, average spatial resolution and average image compression graphics were obtained by using Excel, Gnuplot and Matlab.

All flood source position maps resulting from a position sensitive photomultiplier tube formed by the help of Matlab.

According to the simulation results, the light output of different surface treatments and reflector materials were explored at LSO crystal and it was found that Ground + Air (GA) and Ground + Methacrylate (GM) gave the best results in terms of the average energy resolution.

Apart from these, when comparing the simulation results of the GA and GM related with the energy resolution, GA gave the slightly better results than GM.

Regarding the crystal thickness, the best energy resolution results were obtained at 6 mm crystal thickness except GB (Ground + Black surface treatment).

In this study, the best spatial resolution results were obtained with GM and GA. When dealing with all the simulation results in terms of the spatial and energy resolution, it is seen that GA (Ground + Air) surpasses the all the others. Also, Ground + Methacrylate surface treatment results are the close pursuer of Ground + Air one.

In this work, severe image compression has been seen (pin-cushioning). The main reason of this image compression is a natural consequence of using linear Anger logic (Weighted-Centroid based algorithm) on a resistive plate type position encoding photo sensor (PS-PMT). Today, this algorithm is still widely used for position estimation for PET detectors. The widespread use of this algorithm is due to their sample hardware realization and reasonable performance. However, this type of position estimator disregards the statistical fluctuations of scintillation photons and the non-linear properties of the response of the PMT or PS-PMT tubes as a function of event position [126].

In this research, the better image compression results were obtained with (Ground + Black) GB and (Polished + Black) PB. When comparing image compression results of GB and PB, GB is slightly better than PB. In contrast to spatial and energy resolution results, image compression is better for PB and GB.

However, when dealing with all the simulation results in terms of the spatial and energy resolution and also image compression, it is seen that GA (Ground + Air) surpasses all the others except image compression. Also, Ground + Methacrylate (GM) surface

treatment results are the close pursuer of Ground + Air (GA) one. Additionally, 6mm crystal thickness is found more satisfactory.

The obtained results were checked by changing RC values too. In this situation;

- There has been no any change in average energy resolution either 0.05RC or 0.95RC for 6mm crystal thickness of GA (Ground + Air).

- However, regarding average spatial resolution, it has been found that it was 1,392mm for central coordinates at 0.05RC whereas this value has changed to 1.284mm at 0.95RC (positively %7.76).On the other hand, average spatial resolution value at out of central coordinates reduces from 0.856mm from 0.795mm (positively %7.12).

When discussing the image compression of 6mm LSO scintillation crystal for Ground + Air surface treatment detector design, it was found that at the central coordinates image compression is %82.7 for 0.05RC and %81.74 for 0.95RC (positively %0.95).

On the other hand, this value has increased from %83.7 to %85.15 for out of central coordinates (negatively %1.45). Therefore, it has been understood that 0.05RC value has given better results.

The end word, high spatial resolution is the most important parameter for a PET detector. In this work, Ground + Air surface treatment gives the highest spatial resolution but, the image compression is poor. However, this poorness can be avoided by using certain statistics based positioning (SBP) algorithms [127].

Although, many researchers have still tried to develop new positioning algorithms to eliminate this problem, more research is underway.

7.1 Future Work:

In the future works, further development of this study can be expected. First of all, it can be started with further testing of the proposed detector design with SBP (statistics based positioning) algorithms in order to eliminate the image compression problem. For this reason, the larger scintillation crystal (e.g.6mm thickness) with SBP will be used and then the impact of crystal thickness on SBP algorithm will be investigated.

Finally, phoswich detector designs can be explored to obtain better energy and spatial resolution results.

APPENDIX A

A.1 POSITRON EMISSION TOMOGRAPHY

One of the major methods for tomographic imaging in nuclear medicine is positron emission tomography (PET). PET has progressed with the development of modern nuclear medicine through the discovery of new radiopharmaceuticals. It has gained widespread clinical acceptance in recent years. This promising technology makes possible to study physiological and biochemical processes easily not realizable with standard nuclear medicine techniques in living organism. PET is a complex functional imaging technique. It requires many conditions altogether. These are radionuclide production facilities, advanced radiochemistry, PET scanners, mathematical modelling of biochemical processes and also trained personnel [128].

PET is based on the detection of two high-energy gamma rays (511 keV) which are emitted during positron–electron annihilation. Annihilation photons can be detected by the single photon emission tomography (SPECT) operating in conventional single-photon counting mode. However, these systems are not optimally designed for the high energy annihilation photons (511 keV) .SPECT has relatively low detection efficiencies at these energies and requires inefficient high-energy collimators. PET systems take the advantage of back-to-back directional characteristics of annihilation photons (511 keV) with special annihilation-coincidence detector systems [129].

Classical imaging modalities such as Magnetic Resonance Imaging (MRI), X-rays and Computerized Tomography (CT) are anatomical imaging techniques which show the density of several biological tissues. However, while some body tissues may have very similar densities, some may have varying ones. In such situations, it is difficult to identify problems such as tumors [105].

The main advantage of the PET imaging is the ability of obtaining quantitative images of biochemical processes in living subject without invasive measurements. It can display the concentration of radioactive chemicals. These organic compounds used in the chemical processes can be synthesized from short-lived radioactive isotopes such as carbon, nitrogen, oxygen, and fluorine, the resulting radiopharmaceutical can be given into the

subject by a simple intravenous injection lacking disturbing the existing metabolism and their concentration can be linked to a specific activity in the living body. For example, FDG 2-[F-18]-fluoro-2-deoxy-D-glucose [-F-18-FDG] acts like normal glucose, (basic cell fuel). A high concentration of FDG in a body region displays that there is high cellular metabolism in that region. Because tumors have a very high metabolism, FDG concentration is one of the best indicators of tumors [105,130,131].

PET imaging has also been used for in study of brain functions. By using FDG, it is possible to see which region of the brain is activated when specific actions or thought are realized. Moreover, it is possible to study cardiac activity, blood flow oxygen inhalation and specific illnesses related to brain e.g. epilepsy, Alzheimer [105]

Nowadays, The PET production companies (GE, Siemens, Phillips) are focusing their production efforts on integrated CT-PET scanners that gives both anatomical and functional images.

A.2 Physics of PET

PET uses positron emitting isotopes to visualize the activity in the body. A positron emitter must have more protons than the neutrons in the atomic nucleus. In a normal case, an atomic nucleus either has an equal number of protons and neutrons or more neutrons. The proton surplus in the nucleus leads to instability of an atom and for stabilization of an atomic nucleus , one proton turns into a neutron by emitting its positive charge that is positron [131].

$$p = n + \beta^{+} + v + \text{energy} \quad \text{(positron decay)}$$

In the table below, common positron emitters and their characteristics are shown.

Table A.1: List of the common isotopes used in PET together with main characteristic and usage.

Radionuclide	$t_{1/2}$ (min.)	Maximum range (mm)	Maximum Positron Energy (MeV)	Compound application
Carbon 11 (^{11}C)	20.4	5.0	0.97	Methionine,protein synthesis
Nitrogen 13 (^{13}N)	9.96	5.4	1.19	Brain physiology and pathology
Oxygen 18 (^{18}O)	2.07	8.2	1.7	Water,blood flow utilisation
Fluorine 18 (^{18}F)	109.7	2.4	0.64	FDG,glucose utilisation

The half-lives of common positron emitters used for PET are between 2 and 110 minutes. Short half-life radioisotopes are very good for PET imaging. Since the positron emitters used in human PET studies have very short half-life, they have to be created in a site where they are used, so medical cyclotrons are needed to create positron emitting isotopes. The basic mechanism of the cyclotron is to accelerate protons or deuterons onto a target. For instance, the creation of O^{15} includes a proton bombardment of N^{14} (the most common nitrogen isotope)

After creating the radioisotopes, some chemicals procedures are required to form the right compound for the PET imaging. Then this compound is injected to the (living body (human being, rodents or primates).

When a positron emitter decays, the formed positron goes into a random direction. Since it is so energetic, it can not directly interact and then integrate with an electron. Before this integration, firstly, the positron loses its energy through collision with surrounding medium. (The known positron range is in the order of the millimetre.)

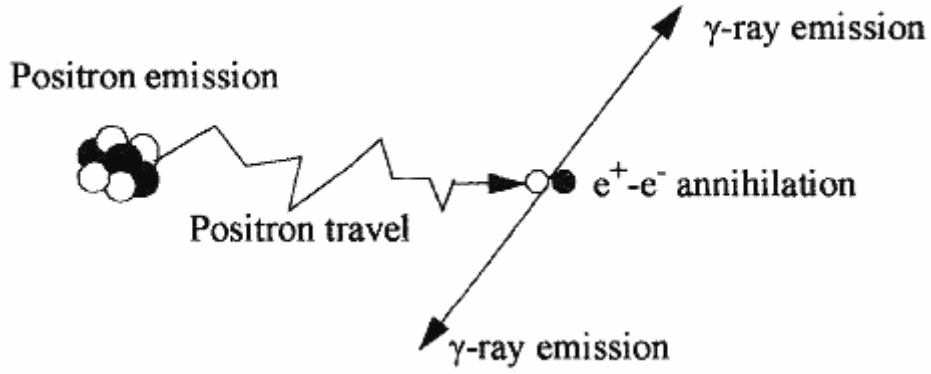

Figure A.1: Positron decay, travel and disintegration [105].

A.3 Interaction of Gamma Rays

Although a large number of possible interaction mechanisms are known for gamma rays in matter, only three major types play an important role in radiation measurement: photoelectric effect, Compton scattering and pair production.

However, for PET, 511 keV gamma rays interact with solid matter mainly through 2 types of interaction: one of them is the photoelectric effect and the other one is the Compton Effect.

All these processes cause the partial or complete transfer of the gamma ray photon energy to electron energy [66].

A.3.1 Photoelectric Absorption

The photoelectric effect is an interaction that takes place between an incident photon and an inner orbital electron. In order to be a photoelectric occurrence, the energy of the incident photon must be greater than the binding energy of the orbital electron. In the photoelectric effect the photon energy totally absorbed. Some of this energy is used to break the bond of the electron in its shell and remaining one given to the electron in the form of kinetic energy (motion). The generalized relationship for this interaction can be written as:

Photon energy = Electron binding energy + electron kinetic energy

The photoelectric effect usually occurs with the electrons of K or L shell of the atomic nucleus. Since an electron has been removed from the atom, there is no longer an electrically neutral balance between the number of protons and electrons; therefore the atom has been ionized with an inner shell vacancy created. In this interaction an ion pair has been formed that is the positively charged atom and negatively charged photoelectron which leaves the atom.

The electron vacancy can be filled by another orbital electron dropping into fill vacancy with the subsequent emission of a characteristic x-ray or by an Auger electron. The disappearance of the incident photon is important clinically because the energy has been absorbed completely by the living subject.

The probability of a photoelectric interaction occurring depends on the energy of the incident gamma ray and the atomic number of the material. As photon energy increases, the probability of a photoelectric interaction decreases. The photoelectric interactions are likely to occur in high Z materials (e.g. lead) but, are unlikely to occur in low Z ones (water and tissue).

The photoelectric effect is therefore the primary interaction type for detecting gamma rays with nuclear medicine instruments (e.g. PET) .[131]I

A.3.2 Compton Scattering

Compton scattering is an incomplete absorption of gamma rays or scattering gamma radiation. The Compton Effect involves an inelastic interaction of photons with outer orbital electrons. Compton Effect was observed by Arthur Holly Compton in 1923, for which he earned the 1927 Nobel Prize in Physics.

In Compton Effect, there is the emission of an electron that is ejected from the atom. In contrast to photoelectric effect, not all of the incident gamma ray energy is absorbed and a scattered photon of lower energy and longer wavelength is emitted [131,132].

A.3.3 Pair Production

Pair production is an interaction produced when a photon with energy greater than 1.02MeV passes near the high electric field of the nucleus. The strong electric force brings about the energy-mass conversion. When the photon comes near the nucleus, it disappears totally and two particles of matter are created, an electron and positron, each possessing the mass equivalence of 0.511MeV. For this interaction to occur, the initial photon must possess 1.02MeV or more of energy [131].

A.3.4 Types of Coincidence Events

The schematically presentation of coincidence event types are shown in the Figure A.2.

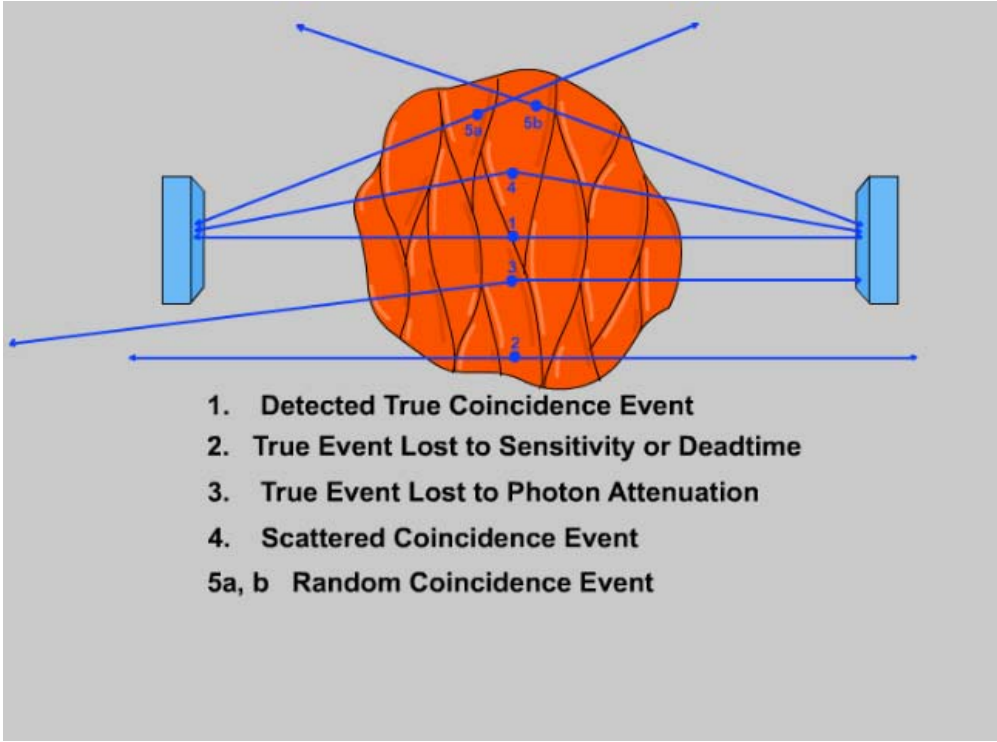

Figure A.2: Types of coincidence events.

APPENDIX B

B.1 Scintillator (definition and types):

A scintillator absorbs ionizing radiation, such as X-ray or gamma ray and converts a fraction of the absorbed energy into visible or ultraviolet light. This conversion process happens on time scale of nanoseconds to microseconds. High-energy photon emitted by the radioisotope interacts with the crystal. At certain point in the volume, (referred to as the scintillation point) the energetic photon (X-ray or gamma ray) leads to a flood of low-energy light photons (in visible or UV spectra) propagating isotropically in the crystal. Gamma quanta can interact several times with the scintillator, thus producing several scintillation points.

Scintillators can be liquid, solid, organic, inorganic, crystalline and non crystalline. Organic, liquid and plastic scintillators are generally used for detection of β particles and fast neutrons. However , for the detection of X- and γ-ray , such as the 511keV γ-rays used in PET, inorganic single-crystal scintillators are chosen, because of their generally higher density and atomic number that provides better detection efficiency.

A typical scintillator, the valance and conduction band are separated by a band gap of 5 eV or more. However, most of the scintillators are doped with an activator ions which lead to the emission of scintillation photons typically around 4 eV, corresponding to visible blue light.

In the early years of PET, NaI (Tl) scintillation crystals that individually coupled to PMTs were made. Then, with the discovery of bismuth germanate (Bi4Ge3O12 or BGO) most detector producers converted to this material due to its higher γ-ray detection efficiency. Other scintillators have included barium fluoride (BaF_2), yttrium aluminate (YAlO3 [Ce] or cerium doped gadolinium oxyorthosilicate Gd_2SiO_5 [Ce] or GSO.

In recent years, cerium doped lutetium oxyorthosilicate (Lu_2SiO_5 [Ce] or LSO are used and is likely to be used widely for the new generation PET scanners [133,134,135,136].

B.2 Characteristics of the Ideal Scintillators:

The ideal scintillator would have a several physical and scintillation properties. The most important one is the stopping power of scintillation crystals for γ-rays. The stopping power of a scintillator for γ-rays refers to its ability to absorb γ's within a short distance. For a given material, it depends on the incident photon energy so that someone talks about stopping power for a particular γ-energy. The notion of stopping power is expressed in terms of attenuation length of theγ's in the material and of photo fraction. To make an efficient detector, the cross section for photoelectric effect must be large compared to Compton scattering cross section. A higher density will also increase the interaction probability and thus shorten the path of the particule into the scintillator. Usually, PET applications require a density greater than 7 g/cm^3

In reality, there is no ideal scintillator. (see Table B.1)

Table B.1: Properties of ideal scintillation crystal for PET [136].

Crystal Property	Purpose
High Density	High γ-ray detection efficiency
High atomic number	High γ-ray detection efficiency
Short decay time	Good coincidence timing
High light output	Allows large number of crystal elements per photodetector
Good energy resolution	Clear energy identification of full energy events
Emission wavelength near 400 nm	Good match to photomultiplier tube response
Transparent at emission wavelength	Allows light to travel unimpeded to photomultiplier tube
Index of refraction near 1.5	Good transmission of light from crystal to photomultiplier tube
Radiation hard	Stable crystal performance
Non-hygroscopic	Simplifies packaging
Rugged	Allows fabrication of smaller crystal elements
Economic growth process	Reasonable cost

Therefore, someone must look at the characteristics of materials and choose the one best suited to the application.

B.3 Scintillators Used In PET

NaI (Tl) was discovered in 1948 by Hofstadter. It quickly became the scintillator of choice for radiation detection because of its high light output, i.e., efficient conversion of deposited gamma-ray energy to scintillation photons [136].

The main disadvantage of NaI (Tl) is its low detection efficiency for gamma-rays above 200 keV, as a result of low density and moderately low atomic number.

At the energies typically used in SPECT (140 keV), the detection efficiency of NaI (Tl) is satisfactory, and it is used almost exclusively in that application. However, for higher energy applications, such as PET (511 keV), NaI (Tl) has been replaced by materials with higher density and atomic number.

An additional disadvantage of NaI (Tl) is that it is highly hygroscopic. As a result, a great deal of effort has gone into the development of hermetic packaging to protect the material from moisture in the atmosphere.

BGO emerged in the early 1970s, with initial studies reported by Weber and Monchamp. Although the light output of BGO is only about 15% of that of NaI(Tl), its detection efficiency is dramatically higher than that of NaI due to its density which is almost twice that of NaI [137].

As regards CsF has very low light output and is very hygroscopic and, consequently, has seen little use despite its short decay constant of 4 ns.

BaF_2 has an even faster decay of less than 1ns, greater light output, and is non-hygroscopic. Therefore, in the early 1980s it was used in several PET scanners. However, because of its relatively low density and atomic number, it eventually gave way to BGO [138].

One way to increase the spatial resolution of a tomograph is to use phoswich detectors (coupling multiple scintillator crystals with different decay constants to a single photodetector) Pulse-shape discrimination is used to identify the crystal element of interaction. GSO has been used in conjunction with BGO in this way for a high-resolution tomograph. A tomographic design using GSO exclusively has also been reported.

However, fabrication of GSO detectors requires great care, because the crystals cleave easily. Thus, special techniques are needed to avoid cracking the crystal elements during cutting [135,139,140].

LSO offers the best combination of properties for PET of any scintillator known today. It has high density and high atomic number, short decay constant (good for coincidence timing), and high light output (allows the use of many small elements per PMT), so, it is good for gamma-ray detection. In addition these, it is mechanically rugged and non-hygroscopic, thus allowing relatively simple fabrication of detectors [141].

LSO has been used in a high-resolution brain tomograph, high-resolution animal tomographs, combined PET/MRI detectors, and combined PET/SPECT cameras [143,144,145].

APPENDIX C

Time period of one simulation is approximately 20-25 minutes below configuration.

C.1 Facilities Required

915G CHIPSET 775 PIN 915ME AGP8XV PCIEX16X MOTHERBOARD GIGABYTE

P4 3.0 LGA 775 800MHZ, INTEL P4 3.0 LGA 2MB

512 MB 400 MHZ PC 3200 DDRRAM CL3 KINGSTON KVR 400X64C3/512 (2)

200GB 7200 RPM 8MB CACHE SERIAL ATA NCQ SEAGATE

16X +/- DVDROM 50X CD READER PHILIPS BBD-410

TA230 300W WHITE ATX ASUS CASE BK-108

SP-400P1B 400WATT SILVER POWER SUPPLY

APPENDIX D

D.1 DETECT2000 Simulation Package

DETECT2000 simulation package deals with tracking of the gamma ray interactions in the active volume of the detector, the propagation and detection of individual scintillation photons through different crystal geometries.

DETECT2000 is the successor of DETECT97 and DETECT97 is one version of the original DETECT which originated from the University of Michigan. The program DETECT first was written in the Pascal language. However, DETECT2000 has been coded in C++ , an object-oriented language. It is in fact total rewrite of the DETECT97 that was coded in the C language. During this rewrite period, many features such as the tracking of the time and wavelength history of individual optical photons have been added.

Testing the theoretical performance of a photon sensing device before it is actually constructed can be of great help. With the appropriate Monte-Carlo simulator, it would be possible to study the light photon transport inside the device and give important information that could be used to improve the efficiency of the device. DETECT2000 is a Monte-Carlo simulation model of the light photon behaviour inside an optical device.

DETECT2000's general geometric syntax can create any complex by joining together four basic geometrical forms: planes, cones, cylinders and spheres [105].

D.2 Overview of the Modelling Platform

DETECT2000 is used to simulate the light transport for a given crystal arrays and detector systems. By using it, particular photo detectors (e.g. PS-PMT or PS-APD) with their physical characteristics and different crystal geometries can be simulated.

DETECT2000 suite is composed of three main parts: Builder (A High Level Language Interface to DETECT for the Design of Scintillation Detectors, DETECT2000 (The Object Oriented C++ Language Version of DETECT A Program for Modelling Optical Properties of Scintillators) and GRIT (Gamma-Ray Interaction Tracking) [146].

1-BUILDER (A High Level Language Interface to DETECT for the Design of Scintillation Detectors):

BUILDER is a high level language interface which simplifies the definition of the geometry, optical properties and readout configuration of a given imaging scintillation detector component. BUILDER was designed to extend the functionality of DETECT as part of the simulation platform developed by the PET group at TRIUMF for modelling Positron Emission Tomography detectors.

Conceptually, BUILDER sits on top of DETECT, and is an interface between the user's model definition and the DETECT simulation driver. BUILDER simplifies the task of defining the geometrical properties of a model to DETECT by translating a higher level component definition syntax into the language imposed by DETECT.

The user can define complicated scintillation detector designs by connecting, for example, simple box components, cylindrical or rectangular PMTs, a block detector, or a stack collection [106,107].

2-GRIT (Gamma-Ray Interaction Tracking):

GRIT takes for inputs the photon source energy, angular distributions, collimator positions detector active volume and cross-sections. It simulates the Compton, photoelectric, possibly pair production interactions of γ-rays and creates a source file. GRIT's job is to determine how the γ-rays deposit their energy in the scintillator and to define a geometric model and optical properties of a block design that is in accordance with the DETECT syntax [108].

The active volume of the block first used as input to the gamma ray transport module (GRIT). A uniform beam of gamma rays with specified energy is produced from a distant point source. Each incident photon is then tracked in the crystal volume for photoelectric and Compton interactions. Cross sections for these two processes are derived from GEANT for the inorganic scintillator considered in the crystal detector design. Their relatively ratio is used to randomly choose which of the two processes occurs, and the trajectory of the interacting gamma is randomly generated according to exponential distribution. The total cross section at the energy of the interacting gamma determines the

interaction length of the exponential. Values of the cross-sections are tabulated from 15 to 511 keV in bins of 5 keV.

Tracking is stopped either by a photoelectric interaction, escape of the photons from the block volume, or by a Compton interaction leaving less than 15keV to the recoil photon. For Compton interactions, the direction of the scattered gamma follows the Klein Nishina angular distribution and the energy of the recoil electron is assumed to be converted to light at the interaction vertex. Scattering of gamma rays into the detector from the canister or surrounding supports is not modelled.

Scintillation event information comprising location and the number of light photons generated are produced as output [57,147,148]

3- DETECT2000 (The Object Oriented C++ Language Version of DETECT):

DETECT2000 is a public domain optical photon transport simulation capable of realistically modelling the optics of scintillation detectors. The program is created by Dr. G.F. Knoll .After definition of the detector by the user; the program isotropically generates a number of scintillation photons from a specified volume element and tracks them individually throughout their passage within its components as well as their interactions with its surfaces. Optical tracking of a scintillation photon is followed until it is either absorbed, reaches a detection element or escapes from the detector volume.

D.3 Introduction to DETECT:

DETECT allows for the specification of the geometry of a detector with a very general syntax. Any complex system can be modelled as long as it is possible to separate it into constituent parts composed of a volume specified by multiple planar, cylindrical, conical or spherical surfaces with arbitrary orientation. Also, common unphysical surfaces between adjacent elements can be defined pseudo-surfaces and are ignored by the tracking.

The optical behaviour of real surfaces can be specified to simulate possible reflections under polished, ground, painted, or metallised conditions. Surfaces in optical contact are treated using Fresnel's equation controlling reflection and transmission as well as Snell's law of refraction. Within each optical element, bulk absorption, scattering and wavelength shifting are simulated by specifying a mean distance of photon travel for each

process. Only one wavelength shift is permitted per history, and is accompanied by appropriate changes in absorption, reflection and scattering properties.

The program is well organized using initial definition statements to specify the optical properties of all materials used in the system. A component is selected from this list of possible materials and its geometry delineated by specifying multiple bounding surfaces. These surfaces can be selected from previously defined planes, cylinders, cones or spheres and can be used in either convex or concave orientation.

When the geometry is defined, the scintillation voxel can be defined with the scintillation photons produced in it. These isotropically generated scintillation photons are then followed one by one until they are absorbed, detected or have escaped from the system. At each photon reflection or scattering, the program logic determines the new direction of the photon, identifies the component in which it is travelling and computes the next intersection with a surface.

Then a random sampling is made if a photon is bulk absorbed, escaped, scattered or wavelength shifted over this path. If none of these processes occur, the optical properties of the next surface determine whether the photon is reflected, refracted, detected or absorbed. This process is repeated for all subsequent paths in the history. A maximum flight time per history is defined to abort those cases in which a photon becomes internally trapped.

After the specified number of histories have been completed, a report is prepared that summarizes the probability of occurrence with statistical uncertainty estimate for each of the possible fates. Data are also reported on the probability for wavelength shift, mean age and mean number of surfaces encountered. These data are separately tabulated for all photons. Also, a histogram describing the elapsed time to detection can also be generated [57,107,109].

APPENDIX E

E.1 Introduction to the Monte Carlo Method

Monte Carlo numerical simulation methods can be defined as statistical methods that use random numbers as a base to perform simulation of any specified situation. The name was chosen during the World War II Manhattan Project because of the close connection to the games based on chance and because of the location of a very famous casino in Monte Carlo.

All Monte Carlo codes share some common components, such as random number generator, rules to sample probability distributions, and sets of probability density functions. The features that make the codes different are related to the accuracy, flexibility, efficiency and ease to use of the codes [149].

In most Monte Carlo applications, the physical process can be simulated directly. It only requires that the system and the physical processes can be modelled from known probability density functions (pdfs). If these pdfs can be defined accurately, the simulation can be made by random sampling from the pdfs. A large number of simulations of histories (e.g. photon or electron tracks) are necessary to obtain an accurate estimate of the parameters to be calculated.

Generally simulation studies have various advantages over experimental studies. For instance, for a given model, it is very easy to change different parameters and investigate the effect of these changes on the performance of the system under investigation. Thus, the optimization of an imaging system can be done greatly by the use of simulations. Also, one can study the effects of parameters that cannot be measured experimentally. For example, it is impossible to measure the scatter component of the radiation emitted from a distributed source independently of the unscattered component. By using a Monte Carlo technique incorporating the known physics of scattering process it is possible to simulate scatter events from the object and determine their effect on the final image. Hence, a simulation program can help the understanding of the underlying processes since all details of the simulation are accessible [128].

Several SPECT/PET dedicated Monte Carlo software packages were developed for simulating a variety of emission tomography studies. Among them, public domain codes have been made available in last years, allowing the use of the Monte Carlo method by the whole scientific community and even in the clinical environment.

Several topics were researched by Monte Carlo simulations in both PET and SPECT, among which optimization of imaging system design (including detector, collimator, and shield design), development of correction methods for improved image quantitation, evaluation of correction techniques (scatter/random/attenuation correction, partial volume effect), development and assessment of image reconstruction algorithms, ROC studies, pharmacokinetic modelling.

Two types of Monte Carlo codes can be used for simulating SPECT and PET: 1) general purpose code, which simulate particle transportation and were developed for high energy physics or for dosimetry, 2) dedicated codes, designed specifically for SPECT or PET simulations.

Table summarises the main codes currently available. General-purpose packages include well-validated physics models, geometry modelling tools and efficient visualization utilities. However, it is quite difficult to use or taylor these packages to PET and SPECT.

On the other hand, the dedicated Monte Carlo codes developed for PET and SPECT suffer from a variety of drawbacks and limitations in terms of validation, accuracy and user support [149].

Table E.1: Types of Monte Carlo codes can be used for simulating SPECT and PET [149-167].

Generic codes	
Dedicated codes	EGS4 (radiation dosimetry) MNCP(radiation dosimetry) ITS (high energy phyiscs) GEANT 3 (high energy physics) GEANT 4 (high enerhy phyiscs)
SPECT only:	SIMIND SimsSPECT(derived from MNCP) MCMATV
PET only:	PETSIM EIDOLON Reilhac PET-EGS
SPECT and PET : Dedicated based on Generic codes	SIMSET
SPECT and PET :	GATE (based on GEANT 4)

APPENDIX F

A typical input file is approximately 18 word pages. On the other hand an output file is approximately 1240 word pages.

F.1 Example Input File

```
#*** Input for unmod hrp block geometry with LSO crystal *** #
#n_scintillator=1.825
# -------------- Crystal Block ------------- #
start_box
#boundaries -8.0 8.0 -8.0 8.0 0.0 3.0
boundaries -8.0 8.0 -8.0 8.0 0.1 3.1
n 1.82
absorption_coeff 10000000.0
scattering_coeff 138.0
fin_xmin GROUND 0.05RC
fin_xmax GROUND 0.05RC
fin_ymin GROUND 0.05RC
fin_ymax GROUND 0.05RC
fin_zmin POLISH -1.0RC
fin_zmax POLISH 0.05RC
end_box
# ------------------------------------------- #

# -------------- Optical Grease ------------- #
start_box
boundaries -8.0 8.0 -8.0 8.0 0.0 0.1
n 1.55
absorption_coeff 4000.0
scattering_coeff 4000.0
fin_xmin METAL 1.0RC
fin_xmax METAL 1.0RC
fin_ymin METAL 1.0RC
fin_ymax METAL 1.0RC
fin_zmin POLISH
fin_zmax POLISH
end_box
# ------------------------------------------- #
```

```
***# ANODE1 #***
start_square_pmt
backwards FALSE
position -4.525 9.05 0.0
width 4.525
height 4.525
window_depth 3.0
holder_depth 3.0
pmt_depth 3.0
pmt_gap 0.1
pmt_width 4.2
pmt_height 4.2
offset 0.0 0.0

dummy_plane_depth 100
dummy_fin PAINT 0.85RC

window_side_fins
PAINT 0.85RC
PSEUDO
PSEUDO
PAINT 0.85RC

holder_side_fins
PAINT 0.85RC
PSEUDO
PSEUDO
PAINT 0.85RC

faceplate_interface_fin POLISH

pmt_sides_fin POLISH 1.0RC
window_n 1.52
window_ad -1.0
window_sd -1.0
holder_n 1.52
holder_ad -1.0
holder_sd -1.0
pmt_n 1.52
pmt_ad -1.0
pmt_sd -1.0
detect_n -1.0

connecting_fin POLISH -1RC
holder_hole_fin PAINT 0.85RC
holder_bottom_fin PAINT 0.85RC
```

```
end_square_pmt

***# ANODE2 #***
start_square_pmt
backwards FALSE
position 0.0 9.05 0.0
width 4.525
height 4.525
window_depth 3.0
holder_depth 3.0
pmt_depth 3.0
pmt_gap 0.1
pmt_width 4.2
pmt_height 4.2
offset 0.0 0.0

dummy_plane_depth 100
dummy_fin PAINT 0.85RC

window_side_fins
PSEUDO
PSEUDO
PSEUDO
PAINT 0.85RC

holder_side_fins
PSEUDO
PSEUDO
PSEUDO
PAINT 0.85RC

faceplate_interface_fin POLISH

pmt_sides_fin POLISH 1.0RC
window_n 1.52
window_ad -1.0
window_sd -1.0
holder_n 1.52
holder_ad -1.0
holder_sd -1.0
pmt_n 1.52
pmt_ad -1.0
pmt_sd -1.0
detect_n -1.0

connecting_fin POLISH -1RC
holder_hole_fin PAINT 0.85RC
holder_bottom_fin PAINT 0.85RC
```

```
end_square_pmt

***# ANODE3 #***
start_square_pmt
backwards FALSE
position 4.525 9.05 0.0
width 4.525
height 4.525
window_depth 3.0
holder_depth 3.0
pmt_depth 3.0
pmt_gap 0.1
pmt_width 4.2
pmt_height 4.2
offset 0.0 0.0

dummy_plane_depth 100
dummy_fin PAINT 0.85RC

window_side_fins
PSEUDO
PSEUDO
PSEUDO
PAINT 0.85RC

holder_side_fins
PSEUDO
PSEUDO
PSEUDO
PAINT 0.85RC

faceplate_interface_fin POLISH

pmt_sides_fin POLISH 1.0RC
window_n 1.52
window_ad -1.0
window_sd -1.0
holder_n 1.52
holder_ad -1.0
holder_sd -1.0
pmt_n 1.52
pmt_ad -1.0
pmt_sd -1.0
detect_n -1.0

connecting_fin POLISH -1RC
holder_hole_fin PAINT 0.85RC
holder_bottom_fin PAINT 0.85RC
```

```
end_square_pmt


***# ANODE4 #***
start_square_pmt
backwards FALSE
position 9.05 9.05 0.0
width 4.525
height 4.525
window_depth 3.0
holder_depth 3.0
pmt_depth 3.0
pmt_gap 0.1
pmt_width 4.2
pmt_height 4.2
offset 0.0 0.0

dummy_plane_depth 100
dummy_fin PAINT 0.85RC

window_side_fins
PSEUDO
PAINT 0.85RC
PSEUDO
PAINT 0.85RC

holder_side_fins
PSEUDO
PAINT 0.85RC
PSEUDO
PAINT 0.85RC

faceplate_interface_fin POLISH

pmt_sides_fin POLISH 1.0RC
window_n 1.52
window_ad -1.0
window_sd -1.0
holder_n 1.52
holder_ad -1.0
holder_sd -1.0
pmt_n 1.52
pmt_ad -1.0
pmt_sd -1.0
detect_n -1.0

connecting_fin POLISH -1RC
holder_hole_fin PAINT 0.85RC
```

```
holder_bottom_fin PAINT 0.85RC

end_square_pmt

***# ANODE5 #***
start_square_pmt
backwards FALSE
position -4.525 4.525 0.0
width 4.525
height 4.525
window_depth 3.0
holder_depth 3.0
pmt_depth 3.0
pmt_gap 0.1
pmt_width 4.2
pmt_height 4.2
offset 0.0 0.0

dummy_plane_depth 100
dummy_fin PAINT 0.85RC

window_side_fins
PAINT 0.85RC
PSEUDO
PSEUDO
PSEUDO

holder_side_fins
PAINT 0.85RC
PSEUDO
PSEUDO
PSEUDO

faceplate_interface_fin POLISH

pmt_sides_fin POLISH 1.0RC
window_n 1.52
window_ad -1.0
window_sd -1.0
holder_n 1.52
holder_ad -1.0
holder_sd -1.0
pmt_n 1.52
pmt_ad -1.0
pmt_sd -1.0
detect_n -1.0

connecting_fin POLISH -1RC
holder_hole_fin PAINT 0.85RC
```

```
holder_bottom_fin PAINT 0.85RC

end_square_pmt

***# ANODE6 #***
start_square_pmt
backwards FALSE
position 0.0 4.525 0.0
width 4.525
height 4.525
window_depth 3.0
holder_depth 3.0
pmt_depth 3.0
pmt_gap 0.1
pmt_width 4.2
pmt_height 4.2
offset 0.0 0.0

dummy_plane_depth 100
dummy_fin PAINT 0.85RC

window_side_fins
PSEUDO
PSEUDO
PSEUDO
PSEUDO

holder_side_fins
PSEUDO
PSEUDO
PSEUDO
PSEUDO

faceplate_interface_fin POLISH

pmt_sides_fin POLISH 1.0RC
window_n 1.52
window_ad -1.0
window_sd -1.0
holder_n 1.52
holder_ad -1.0
holder_sd -1.0
pmt_n 1.52
pmt_ad -1.0
pmt_sd -1.0
detect_n -1.0

connecting_fin POLISH -1RC
holder_hole_fin PAINT 0.85RC
```

```
holder_bottom_fin PAINT 0.85RC

end_square_pmt

***# ANODE7 #***
start_square_pmt
backwards FALSE
position 4.525 4.525 0.0
width 4.525
height 4.525
window_depth 3.0
holder_depth 3.0
pmt_depth 3.0
pmt_gap 0.1
pmt_width 4.2
pmt_height 4.2
offset 0.0 0.0

dummy_plane_depth 100
dummy_fin PAINT 0.85RC

window_side_fins
PSEUDO
PSEUDO
PSEUDO
PSEUDO

holder_side_fins
PSEUDO
PSEUDO
PSEUDO
PSEUDO

faceplate_interface_fin POLISH

pmt_sides_fin POLISH 1.0RC
window_n 1.52
window_ad -1.0
window_sd -1.0
holder_n 1.52
holder_ad -1.0
holder_sd -1.0
pmt_n 1.52
pmt_ad -1.0
pmt_sd -1.0
detect_n -1.0

connecting_fin POLISH -1RC
holder_hole_fin PAINT 0.85RC
```

```
holder_bottom_fin PAINT 0.85RC

end_square_pmt

***# ANODE8 #***
start_square_pmt
backwards FALSE
position 9.05 4.525 0.0
width 4.525
height 4.525
window_depth 3.0
holder_depth 3.0
pmt_depth 3.0
pmt_gap 0.1
pmt_width 4.2
pmt_height 4.2
offset 0.0 0.0

dummy_plane_depth 100
dummy_fin PAINT 0.85RC

window_side_fins
PSEUDO
PAINT 0.85RC
PSEUDO
PSEUDO

holder_side_fins
PSEUDO
PAINT 0.85RC
PSEUDO
PSEUDO

faceplate_interface_fin POLISH

pmt_sides_fin POLISH 1.0RC
window_n 1.52
window_ad -1.0
window_sd -1.0
holder_n 1.52
holder_ad -1.0
holder_sd -1.0
pmt_n 1.52
pmt_ad -1.0
pmt_sd -1.0
detect_n -1.0

connecting_fin POLISH -1RC
holder_hole_fin PAINT 0.85RC
```

```
holder_bottom_fin PAINT 0.85RC

end_square_pmt

***# ANODE9 #***
start_square_pmt
backwards FALSE
position -4.525 0.0 0.0
width 4.525
height 4.525
window_depth 3.0
holder_depth 3.0
pmt_depth 3.0
pmt_gap 0.1
pmt_width 4.2
pmt_height 4.2
offset 0.0 0.0

dummy_plane_depth 100
dummy_fin PAINT 0.85RC

window_side_fins
PAINT 0.85RC
PSEUDO
PSEUDO
PSEUDO

holder_side_fins
PAINT 0.85RC
PSEUDO
PSEUDO
PSEUDO

faceplate_interface_fin POLISH

pmt_sides_fin POLISH 1.0RC
window_n 1.52
window_ad -1.0
window_sd -1.0
holder_n 1.52
holder_ad -1.0
holder_sd -1.0
pmt_n 1.52
pmt_ad -1.0
pmt_sd -1.0
detect_n -1.0

connecting_fin POLISH -1RC
holder_hole_fin PAINT 0.85RC
```

```
holder_bottom_fin PAINT 0.85RC

end_square_pmt

***# ANODE10 #***
start_square_pmt
backwards FALSE
position 0.0 0.0 0.0
width 4.525
height 4.525
window_depth 3.0
holder_depth 3.0
pmt_depth 3.0
pmt_gap 0.1
pmt_width 4.2
pmt_height 4.2
offset 0.0 0.0

dummy_plane_depth 100
dummy_fin PAINT 0.85RC

window_side_fins
PSEUDO
PSEUDO
PSEUDO
PSEUDO

holder_side_fins
PSEUDO
PSEUDO
PSEUDO
PSEUDO

faceplate_interface_fin POLISH

pmt_sides_fin POLISH 1.0RC
window_n 1.52
window_ad -1.0
window_sd -1.0
holder_n 1.52
holder_ad -1.0
holder_sd -1.0
pmt_n 1.52
pmt_ad -1.0
pmt_sd -1.0
detect_n -1.0

connecting_fin POLISH -1RC
holder_hole_fin PAINT 0.85RC
```

```
holder_bottom_fin PAINT 0.85RC

end_square_pmt

***# ANODE11 #***
start_square_pmt
backwards FALSE
position 4.525 0.0 0.0
width 4.525
height 4.525
window_depth 3.0
holder_depth 3.0
pmt_depth 3.0
pmt_gap 0.1
pmt_width 4.2
pmt_height 4.2
offset 0.0 0.0

dummy_plane_depth 100
dummy_fin PAINT 0.85RC

window_side_fins
PSEUDO
PSEUDO
PSEUDO
PSEUDO

holder_side_fins
PSEUDO
PSEUDO
PSEUDO
PSEUDO

faceplate_interface_fin POLISH

pmt_sides_fin POLISH 1.0RC
window_n 1.52
window_ad -1.0
window_sd -1.0
holder_n 1.52
holder_ad -1.0
holder_sd -1.0
pmt_n 1.52
pmt_ad -1.0
pmt_sd -1.0
detect_n -1.0

connecting_fin POLISH -1RC
holder_hole_fin PAINT 0.85RC
```

```
holder_bottom_fin PAINT 0.85RC

end_square_pmt

***# ANODE12 #***
start_square_pmt
backwards FALSE
position 9.05 0.0 0.0
width 4.525
height 4.525
window_depth 3.0
holder_depth 3.0
pmt_depth 3.0
pmt_gap 0.1
pmt_width 4.2
pmt_height 4.2
offset 0.0 0.0

dummy_plane_depth 100
dummy_fin PAINT 0.85RC

window_side_fins
PSEUDO
PAINT 0.85RC
PSEUDO
PSEUDO

holder_side_fins
PSEUDO
PAINT 0.85RC
PSEUDO
PSEUDO

faceplate_interface_fin POLISH

pmt_sides_fin POLISH 1.0RC
window_n 1.52
window_ad -1.0
window_sd -1.0
holder_n 1.52
holder_ad -1.0
holder_sd -1.0
pmt_n 1.52
pmt_ad -1.0
pmt_sd -1.0
detect_n -1.0

connecting_fin POLISH -1RC
holder_hole_fin PAINT 0.85RC
```

```
holder_bottom_fin PAINT 0.85RC

end_square_pmt

***# ANODE13 #***
start_square_pmt
backwards FALSE
position -4.525 -4.525 0.0
width 4.525
height 4.525
window_depth 3.0
holder_depth 3.0
pmt_depth 3.0
pmt_gap 0.1
pmt_width 4.2
pmt_height 4.2
offset 0.0 0.0

dummy_plane_depth 100
dummy_fin PAINT 0.85RC

window_side_fins
PAINT 0.85RC
PSEUDO
PAINT 0.85RC
PSEUDO

holder_side_fins
PAINT 0.85RC
PSEUDO
PAINT 0.85RC
PSEUDO

faceplate_interface_fin POLISH

pmt_sides_fin POLISH 1.0RC
window_n 1.52
window_ad -1.0
window_sd -1.0
holder_n 1.52
holder_ad -1.0
holder_sd -1.0
pmt_n 1.52
pmt_ad -1.0
pmt_sd -1.0
detect_n -1.0

connecting_fin POLISH -1RC
holder_hole_fin PAINT 0.85RC
```

```
holder_bottom_fin PAINT 0.85RC

end_square_pmt

***# ANODE14 #***
start_square_pmt
backwards FALSE
position 0.0 -4.525 0.0
width 4.525
height 4.525
window_depth 3.0
holder_depth 3.0
pmt_depth 3.0
pmt_gap 0.1
pmt_width 4.2
pmt_height 4.2
offset 0.0 0.0

dummy_plane_depth 100
dummy_fin PAINT 0.85RC

window_side_fins
PSEUDO
PSEUDO
PAINT 0.85RC
PSEUDO

holder_side_fins
PSEUDO
PSEUDO
PAINT 0.85RC
PSEUDO

faceplate_interface_fin POLISH

pmt_sides_fin POLISH 1.0RC
window_n 1.52
window_ad -1.0
window_sd -1.0
holder_n 1.52
holder_ad -1.0
holder_sd -1.0
pmt_n 1.52
pmt_ad -1.0
pmt_sd -1.0
detect_n -1.0

connecting_fin POLISH -1RC
holder_hole_fin PAINT 0.85RC
```

```
holder_bottom_fin PAINT 0.85RC

end_square_pmt

***# ANODE15 #***
start_square_pmt
backwards FALSE
position 4.525 -4.525 0.0
width 4.525
height 4.525
window_depth 3.0
holder_depth 3.0
pmt_depth 3.0
pmt_gap 0.1
pmt_width 4.2
pmt_height 4.2
offset 0.0 0.0

dummy_plane_depth 100
dummy_fin PAINT 0.85RC

window_side_fins
PSEUDO
PSEUDO
PAINT 0.85RC
PSEUDO

holder_side_fins
PSEUDO
PSEUDO
PAINT 0.85RC
PSEUDO

faceplate_interface_fin POLISH

pmt_sides_fin POLISH 1.0RC
window_n 1.52
window_ad -1.0
window_sd -1.0
holder_n 1.52
holder_ad -1.0
holder_sd -1.0
pmt_n 1.52
pmt_ad -1.0
pmt_sd -1.0
detect_n -1.0

connecting_fin POLISH -1RC
holder_hole_fin PAINT 0.85RC
```

```
holder_bottom_fin PAINT 0.85RC

end_square_pmt

***# ANODE16 #***
start_square_pmt
backwards FALSE
position 9.05 -4.525 0.0
width 4.525
height 4.525
window_depth 3.0
holder_depth 3.0
pmt_depth 3.0
pmt_gap 0.1
pmt_width 4.2
pmt_height 4.2
offset 0.0 0.0

dummy_plane_depth 100
dummy_fin PAINT 0.85RC

window_side_fins
PSEUDO
PAINT 0.85RC
PAINT 0.85RC
PSEUDO

holder_side_fins
PSEUDO
PAINT 0.85RC
PAINT 0.85RC
PSEUDO

faceplate_interface_fin POLISH

pmt_sides_fin POLISH 1.0RC
window_n 1.52
window_ad -1.0
window_sd -1.0
holder_n 1.52
holder_ad -1.0
holder_sd -1.0
pmt_n 1.52
pmt_ad -1.0
pmt_sd -1.0
detect_n -1.0

connecting_fin POLISH -1RC
holder_hole_fin PAINT 0.85RC
```

```
holder_bottom_fin PAINT 0.85RC

end_square_pmt

max_life 10000
max_seed 20000
flag fast_qe 0
flag verbose 0
vms FALSE
ignore_outside_events FALSE
n_gen 1.85
absorption_coeff_gen 4000
scattering_coeff_gen 4000
```

F.2 Example Output File

```
Photons simulated:                    3116
Photons counted:                      49.2298% (0.895612%)
Photons escaped:                      0.320924% (0.101322%)
Photons Bulk Absorbed:                0.00000%
Photons Surface Absorbed:             50.4493% (0.895682%)
Photons Timed Out:                    0.00000%
Photons Transmitted:                  0.00000%
Photons shifted (counted):            0.00000%
Photons Shifted (all):                0.00000%
Mean Decay Time (counted):            --------
Mean Decay Time (all):                --------
Mean Flight Time (counted):           0.111838 (0.00230264)
Mean Flight Time (all)                0.103948 (0.00161121)
Mean Detect Time:                     0.00000 (   0.0)
Mean Flight Trajectory length (counted):  19.8442 (0.400232)
Mean Flight Trajectory length (all):  18.0853 (0.280411)
Mean Surfaces (counted):              7.32008 (0.108633)
Mean Surfaces (all)                   5.90019 (0.0840245)
Random number seed:                   1226
Photon generation in material: 1
X:  0.003 to 0.003
Y:      0 to      0
Z: 0.9942 to 0.9942
------------------------------
```

Comp #, sum of detected photons

1	0
2	0
3	0
4	0
5	1
6	1
7	0
8	0
9	0
10	0
11	1
12	0
13	0
14	0
15	0
16	0

Centroid of position sensitive surface 1: X: -1.26113 Y: 1.96352 Z: -3.65954

APPENDIX G

G.1 Energy Resolution:

Energy Resolution can be quantified as the full width at half maximum (FWHM) of the photopeak. This is measured by first determining the number of counts at the top of the photopeak and then locating the points on either side of the peak where the counts are half of the peak counts.

The width of the photopeak in pulse height units is obtained by subtracting the lower pulse height from the upper. Finally, this width is divided by the pulse height (energy) at the apex of the photopeak and multiplied by 100 to produce an energy resolution measurement in percent. The smaller the number, the better the energy resolution [131].

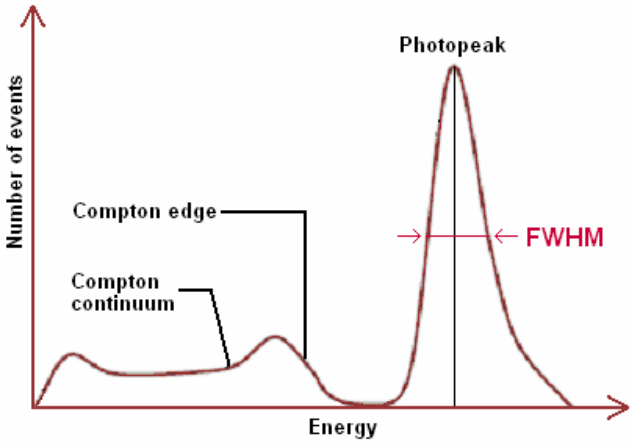

Figure G.1: The components of a typical optical pulse-height spectrum (OPHS) for monoenergetic incident gamma rays.

The names of components of this graphic are shown in Figure G.1.

Benefiting from this type of graphic, FWHM can be calculated with the Equation g.1

% Energy Resolution = (Full width at half maximum / Photopeak center) x 100 (g.1)

G.2 Spatial Resolution:

Spatial resolution can be defined in terms of the amount by which a system smears out the image of a very small point source or a very thin line source of radioactivity. A profile of the counts along a line through the point source image (which is called as the point spread function) or through the line source image (perpendicular to the line, line spread function) can be produced.

Resolution can be quantified as the FWHM of the point or line spread function and generally expressed in millimetres. This measurement of spatial resolution is directly analogous to the measurement of energy resolution as the FWHM of the photopeak of a pulse height spectrum as seen in the Figure G.1.

The purpose of the measurement of the spatial resolution is to characterize the width of the point spread function (PSF) in the reconstructed image of compact radioactive sources. The width of the PSF is reported as the full with at half maximum (FWHM) and full width at tenth maximum (FWTM). (Figure G.2)

The spatial resolution is measured in the transverse slice in two directions radially and tangentially and in the axial direction. (Figure G.3) [168,169].

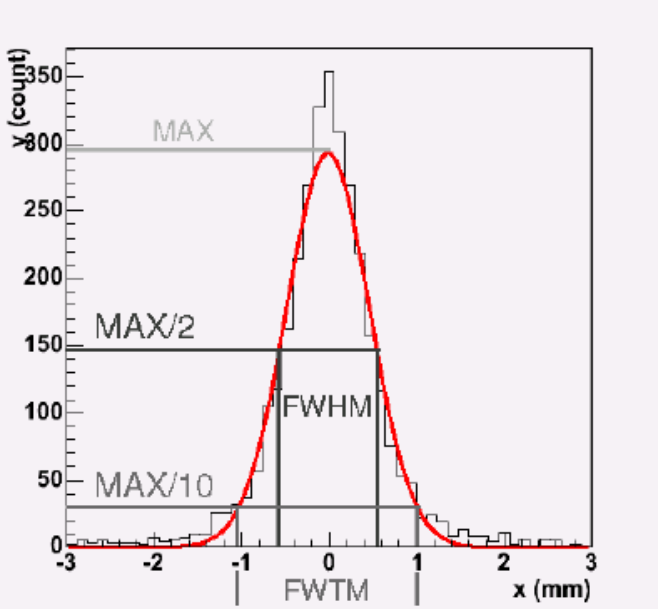

Figure G.2: The schematic representation of FWHM and FWTM [170,171].

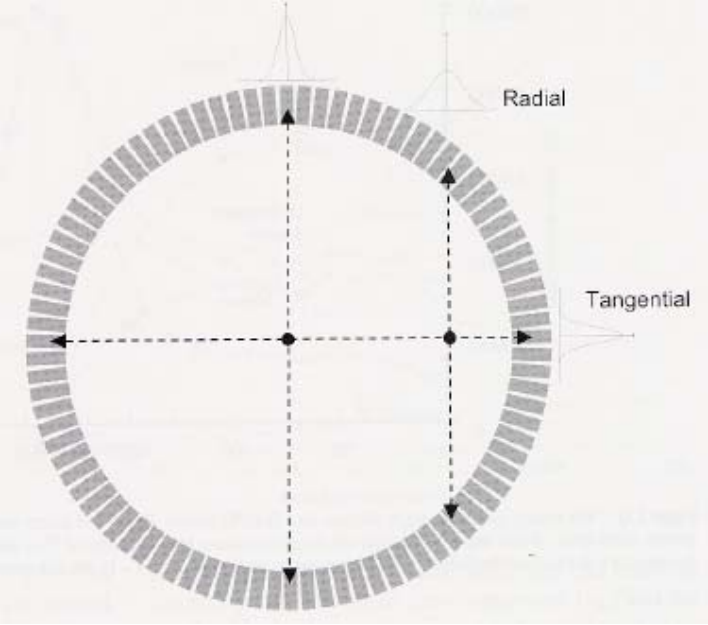

Figure G.3: Transaxial resolution separated into tangential and radial components. As moving the source of radioactivity of off-axis, the energy absorbed in the scintillator will be broadening over a number of detector elements. Spatial resolution in this direction decreases under this uncertainty in localizing the photon interaction to one discrete detector [169].

G.3 Image Compression:

The main reasons of the pincushion effect in PET detectors are;

1. Geometric configuration: It has a significant influence on the spatial resolution. The more distant is the interaction point (source positions) from the PS-PMT's photocathodes centers, the smaller is the solid angle subtended by the PS-PMT. This implies fewer amounts of photoelectrons produced and causes image compression.

2. Multiple reflections and refractions related with the crystal thickness: Multiple reflections and refractions which is related with the crystal thickness distort the light distribution in the crystal and lead to losses of scintillation photons in continuous scintillation crystal. As a result, it causes image compression. Also, as the crystal gets thicker, there are more Compton scatter in the crystal and a larger fraction of the crystal being influenced by the edge effects.

3. The used detection algorithm: Spatial or positional resolution can even more degrade due to the limitations of a detection algorithm to provide sufficiently precise estimation of distant events. Therefore, it also causes image compression. As the result, the spatial resolution in regions close to the detector edges significantly degrades [119,120,121,122,123].

4. Surface treatment of the crystal sides,

5. Structure of the sensor,

6. Positron range.

APPENDIX H

H.1 Post Processing Module: Quantum Efficiency by Using Perl Scripting

```
#!/usr/bin/perl
use Math::Round;
$length=@ARGV;
if ($length!=2) {
        die ("Invalid number of arguments. You should give 2 argument only\n");
}
else {
#       print "Now the file will be parsed for prosessing :\n";
#       print "@ARGV[0] is the filename :\n";
#       print "@ARGV[1] is the quantum efficiency :\n";
        open (FILE,@ARGV[0]);
        while ($line=<FILE>) {
                chomp($line);
                if($line=~/DETECT/) {
                        $line=~s/$/,PS/;
                        print "$line\n";
                }
                elsif($line=~/^RUN/) {
                        $qe=@ARGV[1];
                        $line=~s/^RUN(\d*)/RUN_XXXX_$1_XXXX_/;
                        @vals=split("_XXXX_",$line);
                        $new_val=$qe*$vals[1];
                        $last_val=round($new_val);
                        $line=~s/^RUN_XXXX_\d*_XXXX_/RUN$last_val/;
                        print "$line\n";
                }
                else {
                        print "$line\n";
                }
        }
}
```

REFERENCES

1. Ternar, O., *Camera Techniques for Radionuclide Scanning.* PhD thesis, the Medical Division of the Oak Ridge Institute of Nuclear Studies, Washington 25, D.C., U.S.A, 1963.
2. Greenleaf, A. R., *Photographic Optics*, New York: the Macmillan Company, 1950.
3. Southall, J. P. C., *Mirrors, Prisms and Lenses*, New York: the Macmillan Company, 3rd ed., 1933.
4. Woodburn, J. H., "Chronology of Steps Leading to Our Present Knowledge about Nuclear Science, Nuclear Science Teaching Aids and Activities," Washington, U.S. Government Printing Office, pp. 63–72, 1959.
5. Anger, H. O., "Scintillation and Positron Cameras," USAEC Report UCRL-8640, August 1959.
6. Becquerel, H., "Sur les radiations émises par phosphorescence," *Académie des Sciences (Paris) Comptes Rendus des Séances*, Vol. 122, pp. 420–42l, 1896.
7. Curie, P., and S. Curie, "Sur une substance nouvelle radioactive contenue dans la pechblende," *Académie des Sciences*, Vol. 122, pp. 175–178, 1898.
8. Curie, P., M. Curie, and G. Bemont, "Sur une nouvelle substance fortement radioactive, contenue dans la pechblende," *Académie des Sciences*, Vol. 127, pp. 1215–1217, 1898.
9. Blahd, W. H., F. K. Bauer, and B. Cassen, "The Practice of Nuclear Medicine," Springfield, Illinois, U.S.A., 1958.
10. Brucer, M., "The Development of Radioisotope Scanning. Applications of radioisotopes and radiation in the life sciences," Washington, United States Government Printing Office, pp. 402-426, 1961.
11. Beaudoin and Ceytre, "La Radiumthérapie," *Rev. Scientifique*, Ser. 5, Vol. 9, pp. 111–114, 1908.
12. Dessauer, F., "X-rays similar to radium gamma rays," *Physik,*. Z. 15, pp. 739–791, 1914.
13. Halliday, D., *Introductory Nuclear Physics*, New York: John Wiley and Sons, Inc., 1955.
14. Birks, J. B., *Scintillation Counters*, New York: McGraw-Hill Book Co., Inc., 1953.
15. Mayneard, W. V., and E. H. Belcher, "Scintillation Counting and its Medical Applications," *Brit. J. Radiol.*, Suppl. 2, pp. 259–290, 1950.
16. Blau, M. and B. Dreyfus, "The Multiplier Photo-tube in Radioactive Measurements," *Rev. Sci. Inst.* 16, pp. 245–248, 1945.
17. Bleuler, E. and G. J. Goldsmith, *Experimental Nucleonics*, New York, Bolt, Rinehart and Winston, 1952.

18. Kallmann, H., "Quantitative Measurements with Scintillation Counters," *Phys. Rev.,* Vol. 75, pp. 623–626, 1949.
19. Deutsch, M., "Scintillation Counters with Naphthalene," Laboratory for Nuclear Science and Engineering, Massachusetts Institute of Technology, Technical Report U-1385, No. 3, 1947.
20. Jordan, W. H., and P. R. Bell, "Scintillation Counters," *Nucleonics*, Vol. 5, No. 5, pp. 30–4l, Oct 1949.
21. Hofstadter, R., "Alkali Halide Scintillation Counters," *Phys. Rev.*, Vol. 74, pp. 100–101, 1948.
22. Copeland, D. E. and E. W. Benjamin, "Pinhole Camera for Gamma-ray Sources," *Nucleonics*, Vol. 5, No. 2, pp. 44–49, Aug 1949.
23. Reynolds, G. T., "Liquid Scintillation Counters," *Nucleonics*, Vol. 6, no. 5, pp. 68–69, May 1950.
24. Johannson, S. A. E. A., "Scintillation Spectrometer for High-Energy Gamma Rays," *Nature,* Vol. 166, pp. 794–795, 1950.
25. Harris, C. C., *Collimators for Radioisotope*, Scanning ORINS Scanning Symposium, Oct 1962.
26. Kakehi, H., Problems of Collimation. Medical Radioisotope Scanning. Proceedings of a seminar jointly organized by the International Atomic Energy Agency and the World Health Organization. Vienna, 25-27 February 1959. Vienna, International Atomic Energy Agency, pp. 13–29, 1959.
27. Cassen, B., L. Curtis, C. Reed, and R. Libby, "Instrumentation for I^{131} Use in Medical Studies," *Nucleonics*, Vol. 9, No. 2, pp. 46–50, Aug 1951.
28. Kaufmann, G. and H. Ernst, "Fotoscanning eine trägheitslose Registrierung von Modulationsgamma –grammen," *Strahlentherapie,* Vol. 107, pp. 493–496, 1958.
29. Reid, W. B., and H. E. Johns, "An Automatic Brain Scanner," *Inter. J. of Applied Radi. and Isotopes*, Vol. 3, pp. 1–7, 1958.
30. Kuhl, D. E., "Rotational Scanning of the Liver," *Radiology*, Vol. 71, pp. 875–876, 1958.
31. Brucer, M., "An Introduction to the Use of the Area Scan in Medical Diagnosis," in *Radioisotope Scanning*, USAEC Report, ORINS-20, Jan 1958.
32. Reid, W. B., and H. E. Johns, "An Automatic Brain Scanner," *Inter. J. of Applied Radi. and Isotopes*, Vol. 3, pp. 1–7, 1958.
33. Kramer, S., L. K. Burton, and N. G. Trott, "Radioactive Isotopes in the Localization of Brain Tumors," *Acta Radiologica*, Vol. 46, pp. 415–424, 1956.
34. Brownell, G. L., *Problems in Radioisotope Visualization*, ORINS Scanning Symposium, Oct 1962.

35. Corbett, B. D., R. M. Cunningham, K. E. Halnan, and E. E. Pochin, “A profile counter and its calibration,” *Physics in Med. and Bio.*, Vol. 1, pp. 37–56, 1956.
36. Pochin, E. B., “Profile Counting,” in Medical Radioisotope Scanning, Vienna, International Atomic Energy Agency, pp. 143–162, 1959.
37. Concannon, J. P., and F. Bolhuis, “Studies with a modified collimator for use with scintillation counter for total body scanning,” *Am. J.Roentgenol*. Vol. 78, pp. 855–863, 1957.
38. Anger, H. O., “A multiple Scintillation Counter In Vivo Scanner,” *Am. Jour. of Roentgenol.*, Vol. 70, pp. 605–612, 1953.
39. Cassen, B., “External Counting and Localization. Radioisotopes in Medicine,” USAEC Report, ORO-125, pp. 189–197, 1955.
40. Brownell, G. L., and W. H. Sweet, “Scanning of positron-emitting isotopes in diagnosis of intracranial and other lesions,” *Acta Radiol.*, Vol. 246, pp. 425–434, 1956.
41. Wrenn, F. H. Jr., M. L. Good, and P. Handler, “The use of positron-emitting radioisotopes for the localization of brain tumors,” *Science*, Vol. 113, pp. 525–527, 1951.
42. Sweet, W. H., “The Uses of Nuclear Disintegration in the Diagnosis and Treatment of Brain Tumor,” N. *Engl. J. Med.* 245, pp. 875–878, 1951.
43. Brownell, G. L., and W. H. Sweet, “Localization of Brain Tumors with Positron Emitters,” *Nucleonics*, Vol. 11, No. 11, pp. 40–45, Nov 1953.
44. Aronow, S. and G. L. Brownell, “An Apparatus for Brain Tumor Localization Using Positron Emitting Radioactive Isotopes,” *IEEE*, IRE National Convention, pp. 8–16, 1956.
45. Brownell, G. L., S. Aronow, and W. V. McDermott, “External localization in organs other than the brain by means of positron emitting isotopes,” USAEC Report, NYO-9309, 1959.
46. Rankowitz, S., J. S. Robertson,, W. A. Higinbotham, and M. J. Rosenblum, “Positron Scanner for Locating Brain Tumors,” *IRE (Inst. Radio Engrs.)* Intern. Con. Record; Vol. 9, BNL - 6041, June 18, 1962.
47. Anger, H. O., “Use of a Gamma-Hay Pinhole for In Vivo Studies,” *Nature*, Vol. 170, pp. 200–201, 1952.
48. Kellershohn, C., and P. Pellerin, “Scintillator Grid Localizes Gamma Emitters Photographically,” *Nucleonics*, Vol. 13, No. 12, pp. 34–37, Dec 1955.
49. Kellershohn, C., and P. A. Pellerin, “Photographic Method for Determining the Localization and Distribution of a Radioactive Substance in the System,” New York, United Nations, Vol. 10, pp. 387–391, 1956.
50. Kellershohn, C., and P. Pellerin, “Sur la possibilité d’utiliser tube amplificateur d’image pour mettre en évidence la localisation et la distribution d’un corps radioactive,” *Société de Bologie et de ses filiales Comptes Rendus de Séances*, Vol. 149, pp. 533–536, 1955.
51. Anger, H. O., “Scintillation Camera,” *Rev. Sci. Instr.*, Vol. 29, pp. 27–33, 1958.

52. Bender, M. A., and M. Blau, Autofluoroscopy: the Use of a Non-scanning Device for Tumor Localization with Radioisotopes [Abstract] *J.Nucl. Med.*, Vol. 1, p. 105, 1960.

53. Rich, D. A., "A Brief History of Positron Emission Tomography," *J.Nucl. Med.,* Vol.25, pp. 4–11, 1997.

54. Anderson, C. D., "Energies of cosmic-ray particles," *Phys. Rev.* Vol. 40, pp. 405–421, 1932.

55. Burnham, C. A., S. Aronow, G. L. Brownell, "A hybrid positron scanner," *Phys. Med.Biol.*, Vol. 15, pp. 517–528, 1970.

56. Ter–Pogassian, M. M., J. O. Eichling, D. O. Davis and M. J. Welch, "The measure in vivo of regional cerebral oxygen utilization by means of oxyhemoglobin labeled with radioactive oxygen," *J. Clin. Invest.*, Vol. 49, pp. 381–391, 1970.

57. Tsang, G., "A Simulation for the Design of Position Encoding Detectors for Positron Emission Tomography", Master's thesis, University of British Columbia, Physics Department, Vancouver, Canada, April 1995.

58. Jan S., G. Santin, D. Strul, S. Staelens, K. Assié, D. Autret, S. Avner, R. Barbier, M.Bardiès, P. M. Bloomfield, D. Brasse, V. Breton, P. Bruyndonckx, I. Buvat, A. F. Chatziioannou, Y. Choi, Y. H. Chung, C. Comtat, D. Donnarieix, L. Ferrer, S. J. Glick, C. J. Groiselle, D. Guez, P-F Honore, S. Kerhoas-Cavata, A. S. Kirov, V. Kohli, M. Koole, M. Krieguer, D. J. van der Laan, F. Lamare, G. Largeron, C. Lartizien, D. Lazaro, M. C. Maas, L Maigne, F. Mayet, F. Melot, C. Merheb, E. Pennacchio, J. Perez, U. Pietrzyk, F. R. Rannou, M. Rey, D. R. Schaart, C. R. Schmidtlein, L. Simon, T. Y. Song, J-M. Vieira, D. Visvikis, R. Van de Walle, E.Wieërs and C. Morel, "GATE: a simulation toolkit for PET and SPECT," *Phys. Med.Biol.* Vol. 49, pp. 4543 – 4561, 2004.

59. Assié K., V. Breton, I. Buvat, C. Comtat, S. Jan , M. Krieguer , D. Lazaro, C. Morel , M.Rey, G. Santin, L. Simon, S. Staelens, D. Strul, J.M. Vieira and R. Van de Walle, "Monte Carlo simulation in PET and SPECT instrumentation using GATE," *Nucl. Instr. Meth.* A527, pp. 180–189, 2004.

60. Staelens S., D. Strul, G. Santin, S. Vandenberghe , M. D. Koole, Y. Asseler , I. Lemahieu and R. Van de Walle "Monte Carlo simulations of a scintillation camera using GATE: validation and application modelling," *Phys Med Biol.*, Vol. 48(18), pp. 3021–42, 2003.

61. Walker, C., L. Ronald, G. Purnell, B. J.-J. Laurie, L. T. Kathy , A. J. Brito and F. J. Ernest, "Introduction to Pet Imaging with Emphasis on Biomedical Research," *NeuroToxicology,* Vol. 25, pp. 533–542, 2004.

62. Nuclear Fields Collimators: http://www.nuclearfields.com/indexproduct.htm.

63. Humm, J. L., Anatoly Rosenfeld and Alberto Del Guerra, "From PET detectors to PET Scanners," *European Journal of Nuclear Medicine and Molecular Imaging,* Vol.30, no. 11, Nov. 2003.

64. Institute for Nuclear Research of RAS: http://arxiv.org/ftp/physics/papers/0601/0601159.pdf.
65. Hamamatsu: http://jp.hamamatsu.com/en/hamamatsu/history/1978-1985.html.
66. Knoll, G. F., *Radiation Detection and Measurement*, New York/Chichester/Weinheim Brisbane/Toronto/Singapore: John Wiley & Sons, Inc, 3rd ed., 2000.
67. Detection Technology: http://www.deetee.com/history.htm.
68. Wikipedia Geiger-Müller Counter: http://en.wikipedia.org/wiki/Image:Geiger.PNG.
69. Nobel Prizes in Physics: http://nobelprize.org/nobel_prizes/physics/laureates/1992/press.html.
70. Schäfers, K. P., A. J. Reader, M. Kriens, C. Knoess, O. Schober, and M. Schäfers, "Performance Evaluation of the 32-Module quadHIDAC Small-Animal PET Scanner," *the Journal of Nuclear Medicine,* Vol. 46, no.6, pp. 996–1004, Jun. 2005.
71. Presentation of Valeri Saveliev, University of Obninsk, Russia: http://www-flc.desy.de/store/hcal/other/040322-VS_MRS-SiPM.pdf.
72. Golovin, V., and V. Saveliev, "Novel type of avalanche photodetector with Geiger mode operation," *Nuclear Instruments and Methods in Physics Research*, A 518 pp. 560–564, 2004.
73. Helbert, D., J. V. Saveliev, N. Belcari, N. D'Ascenzo, A. Del Guerra and A. Golovin, "First Results of Scintillator Readout with Silicon Photomultiplier," *IEEE, Trans. Nucl. Sci*., Vol. 53, no.1, pp. 389–394, Feb. 2006.
74. Saveliev, V., and V. Golovin, "Silicon avalanche photodiodes on the base of metal-resistor semiconductor (MRS) structures," *Nuclear Instruments and Methods in Physics Research*A 442, pp. 223–229, 2000.
75. V. Saveliev, Obninsk State University of Nuclear Engineering, Obninsk, Russia, (Personnel correspondence), 2 August, 2006.
76. Report of Christopher J. Thompson, Montreal Neurological Institute, McGill University, Canada: www.aapm.org/meetings/02AM/pdf/8465-78776.pdf.
77. Chatziioannou, A. F., "Pet Scanners Dedicated to Molecular Imaging of Small Animal Models," *Molecular Imaging and Biology*, Vol. 4, no. 1, pp: 47–63, 2002.
78. Del Guerra, A., and N. Belcari, "Advances in animal PET scanners," *the Q. J. Nucl Med*, Vol. 46, no.1, pp. 35–47, 2002.
79. Larobina, M., A. Brunetti and M. Salvatore, "Small Animal PET: A Review of Commercially Available Imaging Systems," *Current Medical Imaging Reviews*, Vol. 2, pp. 187–192, 2006.
80. Schäfers, K.P. "Imaging small animals with positron emission tomography," *Nuklearmedizin*, Vol. 42, pp. 86–89, 2003.
81. University at Buffalo, Micropet: http://www.research.buffalo.edu/forms/iacuc/MicroPET.doc.
82. Technische Universitaet München, MADPET: http://www.lrr.in.tum.de/~stamatak/publications/madpet_informatik.pdf.

83. Welt der Physik: http://www.weltderphysik.de/de/1552.php.
84. Electronic Design of a Fast Shaping Amplifier, Universitè de Sherbrook, Canada: http://keeper.cmc.ca/news/awards/documents/pratte_sherbrooke.pdf.
85. Ingegneria dei Sistemi Elettronici: http://www.ise-srl.com/.Accessed December 10, 2004.
86. Del Guerra, A., C. Daminani, G. Di Domenico, A. Motta, M. Giganti, R. Marchesini, "An integrated PET-SPECT small animal imager: preliminary results," *IEEE Trans. Nucl. Sci.*, Vol. 47, pp. 1537–1540, Aug.2000.
87. Ricoh Company: http://www.ricoh.co.jp/netmessena/ACADEMIA/JAMIT/MITVM/PET/ TANAKA04/ etext8.html.
88. ANIPET, Christopher J. Thompson, Montreal Neurological Institute, McGill University, Canada: www.bic.mni.mcgill.ca/users/chris/ANIPET_2000.PDF.
89. The ClearPET Small Animal PET System: http://www.raytestitalia.it/CLEARPET.pdf.
90. IEEE Nuclear Science Symposium & Medical Imaging Conference 2004: http://ess.web.cern.ch/ESS/IEEE2004/IndustrialProgramme/SeminarPresentations/CERN-Raytest.pps.
91. Surti, S., J. S. Karp, R. Freifelder, A. E. Perkins and G. Muehllehner, "Design evaluation of A-PET: a high sensitivity animal PET camera," *IEEE Trans. Nucl. Sci,.,*Vol. 50, pp. 1357–1363, Oct. 2003.
92. Seidel, J., J. J. Vaquero and M. V. Green, "Resolution uniformity and sensitivity of the NIH small animal PET scanner: comparison to simulated LSO scanners without depth-of-interaction capability*," IEEE Trans.Nucl. Sci*., Vol. 50, pp. 1347–1350, Oct. 2003.
93. http://www.gehealthcare.com/usen/fun_img/pcimaging/images/explore_vista_170.jpg
94. Woodya, C., A. Kriplan, P. O'Connor, J.-F. Pratte, V. Radeka, S. Rescia, D. Schlyer, S. Shokouh, S. Stoll, P. Vaska, A. Villaneuva, N. Volkow and B. Yu, "RatCAP: a small, head-mounted PET tomograph for imaging the brain of an awake RAT," *Nuclear Instruments and Methods in Physics Research,* Vol. A527, pp. 166–170, July 2004.
95. https://www.phenix.bnl.gov/phenix/WWW/publish/woody/PET/RatCAP/PID27730-v11.pdf.
96. Rouze, N. C., W. Winkle, and G. D. Hutchins, "IndyPET – A High-Resolution, high sensitivity dedicated research scanner," M10-36, *Proc. of the IEEE Nucl. Sci. Symp. and Med. Img. Conf.,* Seattle, WA 1999.
97. Rouze, N. C., K. M. Stanz, and G. D. Hutchins, "Design of IndyPET–II, a High-Resolution, high-sensitivity dedicated research scanner ", *Proc. of the IEEE Nucl. Sci. Symp. Med. Img Conf., San Diego,* CA, Vol. 3, pp. 1545-1549, 4-10 Nov. 2001.
98. Lewis, J.S., S. Achilefu, J. R. Garbow, R. Laforest and M. J. Welch, "Small animal imaging: current technology and perspectives for oncological imaging," *European Journal of Cancer*, Vol. 38, pp. 2173–2188, Nov.2002.

99. Oxford Positron Systems Ltd: http://www.oxpos.co.uk/.Accessed December 28, 2004.

100. Missimer, J., Z. M. Madi, M. Honer, C. Keller, A. Schubiger and S. M. Ametamey, "Performance Evaluation of the 16-module quad-HIDAC small animal PET camera," *Phys.Med. Biol.*, Vol. 49, pp. 2069–2081, May. 2004.

101. Photomultiplier tubes Basics and Applications, second edition, Hamamatsu Photonics K.K., 1999.

102. The Spectroscopy Net: http://www.thespectroscopynet.com/Educational/Detectors.htm.

103. Hamamatsu Photonics K.K., "Flat-panel type multi-anode photomultiplier tube assembly H8711-03," http://www.hamam"Testing Scintillation Transport Models with Photoelectron Yields Measured under Different Surface Finishes atsu.com, data sheet.

104. Gimenez, E.N., J. M. Benlloch, M. Giménez, C. W. Lerche, N. Pavón and M. Rafecas, "Detector Optimization of a Small Animal PET Camera Based on Continuous LSO Crystals and Flat Panel PS-PMTs," *Proc. of the IEEE Nuclear Science Symposium Conference Record,* Vol. 6, pp. 3885–3889, 16-22 Oct. 2004.

105. Facouette, F., "Performance Improvement of a Dual-Layered Pixellated Scintillation Block Using DETECT2000 Monte Carlo Simulations," Master's thesis, McGill University, Montreal, Canada, 2002.

106. Moisan, C, and G. McDonald, BUILDER A High Level Language Interface to DETECT for the Design of Scintillation Detectors User's Manual, Version 6.0, Department of Electrical and Computer Engineering Laval University Quebec City, Quebec, Canada, September 2000.

107. Moisan, C., E. Hoskinson, M. Levin, A. Vozza, D., "Public domain platform to model scintillation counters for gamma-ray imaging applications," Proc. SPIE Vol. 3115, pp. 21–29, Hard X-Ray and Gamma-Ray Detector Physics, Optics, and Applications, Richard B. Hoover; F. Patrick Doty; Eds., 1997.

108. Hoskinson, E., and C. Moisan, The GRIT Essentials, TRIUMF 4004, Version 3.0, May 1995.

109. Moisan, C., F. Cayouet and G. McDonald, DETECT2000, The Object Oriented C++ Language Version of DETECT A Program for Modelling Optical Properties of Scintillators Department of Electrical and Computer Engineering Laval University Quebec City, Quebec, Canada Version 5.0 September 1, 2000.

110. Pedrotti, F. L., and L. S. Pedrotti *Introduction to Optics,* Englewood Cliffs, NJ: Prentice Hall ,2nd edition, 1993.

111. Levin, A. and C. Moisan, "A more physical approach to model the surface treatment of scintillation counters and its implementation into DETECT," *Proc. of the IEEE Nuclear Science Symp. Conf.* Rec., Vol. 2, pp. 702–706, 2-9 Nov. 1996.

112. Thalat, T. M., "Modelling Scintillator-Photodiodes as Detectors for Megavolt Computed Tomography," Master's thesis, University of Alberta, Edmonton,Canada, 2004.

113. Saint-Gobain Company Prelude420 Crystal Datasheet: http://www.detectors.saint-gobain.com/media/documents/S000000000000001004/SGC_PreLude_420_Data_Sheet_1006.pdf

114. Charles L., S. F. Melcher, P. Stephen, M. Cramer, A. Spurrier, P. Szupryczynski and R. Nutt, "Cerium Oxidation State in LSO:Ce Scintillators," *IEEE Transactions on Nuclear Science*, Vol. 52, pp. 1809–1812, Oct. 2005.

115. Knoll, G.F., T.F. Knoll and T.M. Henderson "Light collection in scintillation detector composites for neutron detection," *IEEE Trans. Nucl. Sci.*, Vol. 35, pp. 872–875, Feb.1988.

116. Moisan C., A. Levin, and H. Laman, "Testing scintillation transport models with photoelectron yields measured under different surface finishes," *Proc. of the IEEE Nuclear Science Symposium Conference Record,* Vol. 1, pp. 824–828, 16-22, 9-15 Nov. 1997.

117. Bronstein A., M. Bronstein, M. Zibulevsky and Y. Y. Zeevi "High-Energy Photon Detection in Positron Emission Tomography Using Adaptive Non-Linear Parametric Estimation Algorithms," TECHNION – Israel Institute of Technology Department of Electrical Engineering, the Vision Research and Image Science Laboratory, 2002.

118. Cinti M. N., R. Scafè, R. Pellegrini, C. Trotta, P. Bennati, S. Ridolfi, L. Montani, F. Cusanno, F. Garibaldi, J. Telfer and R. Pani "CsI (Tl) Micro-pixel Scintillation Array for Ultra-high Resolution Gamma-ray Imaging," *Proc. of the IEEE Nuclear Science Symposium Conference Record,* Vol. 4, pp. 2371–2375,19-25 Oct. 2003.

119. Dokhale P.A, R. W. Silverman, K. S. Shah, R. Grazioso, R. Farrell, J. Glodo, M. A. McClish, G. Entine, V.-H. Tran and S. R. Cherry1," Performance measurements of a depth-encoding PET detector module based on position-sensitive avalanche photodiode read-out," *Phys. Med. Biol*. Vol. 49, pp. 4293–4304, Sept.2004.

120. Rogers, J. G.,"Testing 144- and 256-crystal BGO Block Detectors," *Proc. of the IEEE Nuclear Science Symposium Conference Record,* Vol. 3, pp. 1837–1841, 31Oct.-6Nov.1993.

121. Melles Griot Photonics Products: http://www.mellesgriot.com/products/optics/images/fig1_20.gif.

122. Rogers, J. G., C. Moisan, E. M. Hoskinson, M. S. Andreaco, C. W. Williams and R. Nutt "A Practical Block Detector for a Depth Encoding PET Camera," *IEEE Trans.Nucl.Sci*. Vol. 43, pp. 95–82, Dec. 1996.

123. Ling, T., K. Lee and R. S. Miyaoka, "Performance Characteristics of Continuous Miniature Crystal Element (cMICE) Detectors, *Proc. of the IEEE Nucl. Sci. Symp.Con. Record*, Vol.3, pp. 1586–1589, 23-29 Oct. 2005.

124. Miyaoka, R. S., and T. K. Lewellen, "Sub-millimetre Intrinsic Spatial Resolution PET Detector Designs Using Geiger-mode Avalanche Photodetectors" *Proc. of the IEEE, Nucl.Sci.Symp. Conf. Record,* pp. 2903–2907, 2005.

125. Wimvar A**.**, N. Schramm, H. Vosberg and H.-W. Muller-Gartner," Influence of crystal geometry and wall reflectivity on scintillation photon yield and energy resolution," *IEEE* , pp. 1443–1445, 2000.

126. Joung J., R.S. Miyaoka, S.G. Kohlmyer and T.K. Lewellen, "Investigation of Bias-Free Positioning Estimators for the Scintillation Cameras," *IEEE, Trans.Nucl.Sci.* Vol.48, No: 3, pp. 715–719, 2001.

127. Joung, J., R. S. Miyaoka and T. K. Lewellen "cMİCE: a high resolution animal PET using continuous LSO with a statistics based positioning scheme," *Nucl.Ins.and Meth. in Physics Research*, Vol. A 489, pp. 584–598, Aug.2002.

128. Ljungberg, M., S.E Strand and M.A. King, *Monte Carlo Calculations in Nuclear Medicine, Applications in Diagnostic Imaging*, "UK, Bristol : J.W Arrowsmith Ltd, 1998.

129. Cherry, S.R., J. A. Sorenson and M.E. Phelps, *Physics in Nuclear Medicine*, Saunders, Philadelphia, Pennsylvania, 3rd ed., 2003.

130. Tsang, G., "A simulation for the design of position encoding detectors for positron emission tomography," Master's thesis, The University of British Columbia, Vancouver, Canada, 1995.

131. Christian, P. E., D. Bernier, and J. K. Langan, *Nuclear Medicine and PET Technology and Techniques*, St. Louis, Missouri : Mosby Inc., 5th ed., 2004.

132. Wikipedia Compton Scattering: http://en.wikipedia.org/wiki/Compton_scattering.

133. Ter-Pogossian, M., D. Ficke , M. Yamamoto and J. T. Hood "Super PETT I: a positron emission tomograph utilizing photon time-of-flight information," *IEEE Trans. Nucl. Sci.*, Vol. 1, pp. 179, 1982.

134. Weber S, A. Bauer, H. Herzog, et al. "Recent results of the TierPET scanner," *Proc. of the IEEE Nucl. Sci. Symp.Con. Record*, Vol.3, pp. 1603–1607, 1999.

135. Karp J, L.E. Adam, R. Freifelder, G. Muehllehner, F. Liu and S. Surti "High resolution GSO-based brain PET camera," *Proc. of the IEEE Nucl. Sci. Symp.Con. Record*, Vol.2, pp. 1077–1081, 1999.

136. Melcher, C. L., "Scintillation Crystals for PET," *J.Nucl.Med.,* Vol. 41, pp. 1051–1055, Jun. 2000.

137. Weber M. J., and R. R. Monchamp, "Luminescence of $Bi_4Ge_3O_{12}$: spectral and decay properties," *J Appl. Phys.,*Vol. 44, pp. 5495–5499, 1973.

138. Yamamoto, M, D. C. Ficke, and M.M. Ter-Pogossian, "Experimental assessment of the gain achieved by the utilization of time-of-flight information in a positron emission tomograph (super PETT I*)*," *IEEE Trans Med Imaging*, Vol. 1, pp. 187–192, 1982.

139. Eriksson L, C. Bohm, M. Kesselberg, J.-E. Litton, M. Bergstrom and G. A. Blomquist, *A high resolution positron camera*, In: Greitz T, Ingvar DH, Widen L, eds., The Metabolism of

the Human Brain Studied with Positron Emission Tomography, New York, NY: Raven Press; pp.33–46, 1985.

140. Holte S, H. Ostertag and M. Kesselberg , "A preliminary evaluation of a dual crystal positron camera," *J. Comput Assist. Tomogr.*, Vol. 11, pp. 691–697, March 1987.
141. Melcher C. L. and J. S. Schweitzer, "Cerium-doped lutetium oxyorthosilicate: a fast, efficient new scintillator," *IEEE Trans. Nucl. Sci.*, Vol. 39, pp. 502–505, 1992.
142. Schmand M., L. Eriksson and M.E. Casey, et al., Performance results of a new DOI detector block for a high resolution PET-LSO research tomograph HRRT. *IEEE Trans. Nucl Sci.*, Vol. 45, pp. 3000–3006, Dec. 1998.
143. Chatziioannou, A.F., S. R. Cherry and Y. Shao, et al., "Performance evaluation of microPET: A high resolution LSO PET scanner for animal imaging,"*J. Nucl. Med.* Vol. 40, pp. 1164–1175, 1999.
144. Shao, Y, S. R. Cherry and K. Farahani, et al., "Development of a PET detector system compatible with MRI/NMR systems," *IEEE Trans Nucl Sci.*,Vol. 44,1167–1171, Jun.1997.
145. Schmand M, M. Dahlbom and L. Eriksson L et al., "Performance of a LSO/NaI(Tl) phoswich detector for a combined PET/SPECT imaging system," J Nucl Med., Vol. 39, p. 9,1998.
146. Habte F., P. D. Olcott , A. M. K. Foudray, C. S. Levin, J. Zhang and G. Chim , "Simulation and Measurement of Gamma Ray and Annihilation Photon Imaging Detectors," *Proc. of the IEEE Nucl. Sci. Symp.Con. Record*, Vol.6, pp. 4019–4022, 16-22 Oct. 2004.
147. Brun, R., F. Bruyant, M. Maire, A.C. Mc. Pherson, and P. Zanarini, "GEANT3," CERN Data Handling Division, DD/FE/84-1, September, 1987.
148. Leo, W. R., *Techniques for Nuclear and Particle Physics Experiments*, Springer-Verlag, Berlin, Germany, (34, 50–54,149, 157–158), 1987.
149. Small Animal PET and Monte Carlo Simulation, Munich Center of Molecular Lifesciences: http://www.org.chemie.tu-muenchen.de/people/fhagn/JASS2006/files/JASS2006-Torres-Espallardo.pdf.
150. Electron Gamma Shower (EGS) Monte Carlo Radiation Transport Code: http://pager.lbl.gov/egs/egs.html.
151. MNCP directory: http://www-xdiv.lanl.gov/XCI/PROJECTS/MCNP/.
152. Halbleib J. A., R. P. Kensek, T. A. Mehlhorn, G. D. Valdez, S. M. Seltzer, and M. J. Berger, "ITS Version 3.0: the integrated TIGER series of coupled electron/photon Monte Carlo transport codes," Sandia National Laboratories, Technical Report SAND91-1634, 1992.
153. GEANT 3 home page: http://wwwasd.web.cern.ch/wwwasd/geant/.
154. GEANT 4 home page: http://geant4.web.cern.ch/geant4/.
155. Ljungberg, M. and S. E. Strand," A Monte Carlo program for the simulation of scintillation camera characteristics," *Comput. Methods Prog. Biomed.* Vol. 29, pp. 257–72, 1989.

156. Yanch J.C., A. B. Dobrzeniecki, C. Ramanathan, and R. Behrman, "Physically realistic Monte Carlo simulation of source, collimator and tomographic data acquisition," *Phys. Med. Biol.,* Vol. 37, pp. 853–70, 1992.

157. Yanch, J.C., and A. B. Dobrzeniecki, "Monte Carlo simulation in SPECT: complete 3D modelling of source, collimator and tomographic data acquisition, *IEEE Trans. Nucl. Sci.,* Vol. 40, pp. 198–203, 1993.

158. Smith, M. F., "Modelling photon transport in non-uniform media for SPECT with a vectorized Monte Carlo code," *Phys. Med. Biol.*, Vol. 38, pp. 1459–74, 1993.

159. Smith, M. F., C. D. Floyd, and R.J. Jaszczak,, "A vectorized Monte Carlo code for modelling photon transport in SPECT," *Med. Phys.* Vol. 20, pp. 1121–1127, 1993.

160. Thompson C.J., J.M.Cantu and Y. Picard, "PETSIM: Monte Carlo program simulation of all sensitivity and resolution parameters of cylindrical positron imaging systems," *Phys. Med. Bio.,* Vol. 37, pp. 731–49, 1992.

161. Thompson, C.J., and Y. Picard*, PETSIM: Monte Carlo simulation of positron imaging systems,* In: Ljungberg M, Strand SE, King M, editors, *Monte Carlo calculations in nuclear medicine,* Bristol and Philadelphia: IOP Publishing, pp. 233–48, 1998.

162. Zaidi, H., C. Labbe, C. Morel, "EIDOLON: Implementation of an environment for Monte Carlo simulation of fully 3D positron tomography on a high performance parallel platform," *Parallel Comput.,* Vol. 24, pp. 523–36, 1998.

163. Reilhac A., M. C. Gregoire, N. Costes, F. Lavenne, C. Pierre and A. Diou, et al. Seattle, "A PET Monte Carlo simulator from numerical phantoms: validation against the EXACT ECAT HR+ scanner," *Proceedings of the IEEE Nuclear Science Symposium and Medical Imaging Conference,* Vol. 3, pp. 1527–1536, 24-30 Nov.1999.

164. Castiglioni, I., O. Cremonesi, M. C. Gilardi, V. Bettinardi, G. Rizzo and A. Savi, et al., "Scatter correction techniques in 3D PET: a Monte Carlo evaluation," *IEEE, Trans. Nucl. Sci,.*Vol. 46, pp. 2053–2058, 1999.

165. Harrison, R.L., S. D. Vannoy, D.R. Haynor, S.B. Gillipsie, M.S. Kaplan, T.K. Lewellen, San Francisco, "Preliminary experience with the photon history generator module of a public domain simulation system for emission tomography," *Proceedings of the IEEE, Nuclear Science Symposium and Medical Imaging Conference,* pp. 1154–1158, 31Oct.-6Nov.1993.

166. SIMSET. SIMSET overview. http://depts.washington.edu/ simset/html/simset_home.html.

167. GATE home page: http://www-lphe.epfl.ch/~PET/research/gate/.

168. Daube-Witherspoon M. E., J. S. Karp, M. E. Casey, F. P. DiFilippo, H. Hines, G. Muehllehner, V. Simcic, C. W. Stearns, L.-E. Adam, S. Kohlmayer, and V. Sossi, "PET Performance Measurements Using the NEMA NU 2-2001 Standard," *The Journal of Nuclear Medicine*,Vol. 43 No. 10, pp. 1398–1409, October, 2002.

169. Spatial Resolution of the MicroPET for Small Animal, University of Texas: http://ric.uthscsa.edu/personalpages/lancaste/DI2_Projects_2004/KL_Project.pdf.

170. Moehrs S., N. Belcari, A. Del Guerra, D. Herbert, M. Mandelkern, A. Motta and V. Saveliev, "Small Animal PET Design Using SiPMs and Anger Logic with Intrinsic DOI ", *Proceedings of the IEEE, Nuclear Science Symposium and Medical Imaging Conference,* Vol. 6, pp. 3475–3479, 16-22 Oct.2004.

171. NEMA NU 2-2001 - Performance Measurements of Positron Emission Tomographs.